THE UNIVERSITY OF CHICAGO

INTERPLAY OF STRUCTURE, MECHANICS, AND DYNAMICS IN RECONSTITUTED ACTIN

A DISSERTATION SUBMITTED TO

THE FACULTY OF THE DIVISION OF THE PHYSICAL SCIENCES

IN CANDIDACY FOR THE DEGREE OF

DOCTOR OF PHILOSOPHY

DEPARTMENT OF PHYSICS

BY

DANIELLE ROBIN SCHEFF

CHICAGO, ILLINOIS

AUGUST 2021

This work is dedicated to the memory of Faye Scheff. I could not have made it this far without her. She still inspires me daily to be the best possible version of myself.

I must therefore not be discouraged by the difficulty of interpreting life by the ordinary laws of physics. For that is just what is to be expected from the knowledge I have gained of the structure of living matter. I must be prepared to find a new type of physical law prevailing in it.

Erwin Schrödinger, *What is Life?*

TABLE OF CONTENTS

LIST OF FIGURES

LIST OF TABLES

ACKNOWLEDGEMENTS

This work would not have been possible without the assistance of countless others who helped me grow on both a scientific and personal basis over the past six years. I entered graduate school with no background in biology, and could not have learned and developed into a biophysicist without the support of the entire Gardel Lab. They were always willing to teach and never made me feel stupid for asking basic questions. Sayantan Majumdar taught me everything I know about rheology, as well as how to form reconstituted networks. Kimberly Weirich provided invaluable insight and inspired a love of tactoids. It is impossible to fully list everything that I have learned from her. Jonathon Winkelman showed me how to purify proteins and was always available to answer questions about almost any actin protein. Samantha Stam taught me about actomyosin networks and spent too much time helping me troubleshoot and fix my own idiotic mistakes. Patrick McCall taught me about biochemistry and specifically turnover. I used to joke that to get any question answered in lab, you just needed to say it out loud and Patrick would jump in with his insight. Yvonne Beckham kept lab running through normal and pandemic times and was always around to answer any question from “how does cloning work?” to “where do we keep spare paper towels?” Steven Redford provided beautiful simulations and was invaluable for bouncing ideas around and providing feedback. Erik Schumann answered all my basic chemistry questions and was willing to give his advice even after graduating. I was told at one point that when choosing a lab to work in, to look at the advanced graduate students because they demonstrate the scientist you will become working in that group. If I have developed into half the scientist as any of them, I would consider that a huge success.

Of course, I could not have achieved any of this without Margaret Gardel herself. I have grown greatly as a scientist under her guidance. Her feedback was invaluable. Every presentation and paper I showed her become significantly improved by her insight, and as a result I have become a better presenter and writer. I am forever impressed by her capability to advice on a wide range of research areas stretching between biology and physics. The consistent quality of students graduating from her lab is a real testament to her ability as a mentor. Equally important, Margaret did not only care about my research performance, but she also cared about my mental and emotional wellbeing. I remember her telling me that she believes all students should see therapists and that it is okay to be distracted by outside events.

I have also had the fortune to work with great collaborators. Every conversation with Kinjal Dasbiswas was informative, and he always willing to redescribe the tactoid model until I fully understood. The entire Kovar lab, but especially Cristian Suarez, were always willing to help purify proteins and were extremely patient with my never ending questions about actin binding proteins. Finally, Nicole James provide invaluable assistance with rheology.

Outside of research, many people provided support as well. My dad, Andrew Scheff, and brother, Benjamin Scheff, provided indescribable support without which I could have never made it to graduate school, let alone finish a PhD. Additionally, I was fortunate to grow up close to much of my extended family and have had the opportunity to reconnect with more while living in Chicago. My grandmother, Betty-Jane Scheff, continues to inspire me, and I have had the help of too many aunts, uncles, and cousins to name. I have also had the support of many friends both inside and outside of academia. Adam Wang, Lesya Horyn, and Lipi Gupta provide critical support on both an academic and personal basis, especially during our first year. Nidhi

Pashine and Jamie Murphy have been excellent and supportive roommates. Abigail Spanier has always been there when I needed help or comfort. Margaret Overholt has been willing to drop everything to provide needed help. All of these people have been essential, either directly or indirectly, to achieving this work.

ABSTRACT

Cells dynamically control their material properties through remodeling of the actin cytoskeleton, an assembly of cross-linked networks and bundles formed from the biopolymer actin. Actin thus serves as an ideal model system to study mechanical adaptation of the cytoskeleton towards understanding both the functioning of cells and inform the creation of novel materials. In this work, I reconstitute networks *in vitro* to investigate the interplay of three aspects of actin: structure, mechanical properties, and dynamics.

First, I investigate the influence of filament dopants on the internal structure and material properties of protein liquids. I find that the short, biopolymer filaments of actin spontaneously partition into phase separated FUS to form composite liquid droplets. As the concentration of actin increases, the coalescence time decreases, indicating that the dopants control viscosity relative to surface tension. The droplet shape is tunable and ranges from spherical to tactoid as the filament length or concentration is increased. I find that the tactoids are well described by a model of a quasi bipolar liquid crystal droplet, where nematic order from the anisotropic actin filaments competes with isotropic interfacial energy from the FUS, controlling droplet shape in a size-dependent manner. These results demonstrate a versatile approach to construct tunable, anisotropic macromolecular liquids.

Next, I explore how actin networks adapt to external stimuli through structural changes. It was recently found that cross-linked networks of actin filaments can exhibit adaptive behavior. In these networks, training, in the form of applied shear stress, can induce asymmetry in the nonlinear elasticity. Here, I explore control over this response, called mechanical hysteresis, by tuning the concentration and mechanical properties of cross-linking proteins in both

experimental and simulated networks. I find that this effect depends on two conditions: the initial network must exhibit nonlinear strain stiffening, and filaments in the network must be able to reorient during training. Hysteresis depends strongly and non-monotonically on cross-linker concentration, with a peak at moderate concentrations. In contrast, at low concentrations, where the network does not strain stiffen, or at high concentrations, where filaments are less able to rearrange, there is little response to training. Additionally, I investigate the effect of changing cross-linker properties and find that longer or more flexible cross-linkers enhance hysteresis. Remarkably plotting hysteresis against alignment after training yields a single curve regardless of the physical properties or concentration of the cross-linkers.

Finally, I investigate the ability of cross-linkers and myosin activity to control turnover, a dynamic process in which actin continuously polymerizes on one end while depolymerizing on the other. Using fluorescence recovery after photobleaching, I measure actin severing and turnover in these networks. I find that when actin is bundled by the cross-linker α-actinin, cofilin mediated severing and turnover vanishes. Additionally, I find that myosin mediated severing is sufficient to increase the rate of actin turnover, even in systems without cofilin. This increase depends on actin buckling and severing. When buckling is reduced by decreasing filament length, turnover is similarly reduced. Remarkably, α-actinin does not impact myosin mediated severing, and myosin is able to increase turnover even in bundled networks. These results not only suggest that myosin can regulate turnover of actin filaments, but also that different methods of disassembly might be needed to remodel actin depending on its local structure.

CHAPTER 1

INTRODUCTION

1.1 Cells as Materials

1.1.1 Cells are Complex Materials

Early in graduate school, I was asked “are cells liquids or solids?” The answer is both: they are viscoelastic with properties of both viscous and elastic materials. They can simultaneously flow like a liquid yet retain their overall shape like a solid. Cells are not unique in this regard as viscoelasticity is found in many substances, and concepts learned from studying other viscoelastic materials can inform on cellular mechanics [1–5]. Studying the material properties of cells has therefore proven useful in understanding their overall function. However, cells are vastly more complicated than any current artificial material. They are composed of thousands of distinct proteins, along with other macromolecules such as lipids and nucleic acids, which interact in intricate systems. As a result, the material properties of cells are not fully understood, and many of these properties cannot currently be duplicated in artificial materials.

One such example is cells’ ability to adapt to external forces without jeopardizing long term maintenance of shape. To function, cells must be able to maintain a constant shape. At the same time, many processes require cells to undergo rapid structural changes. Much of this adaptation is accomplished through the cytoskeleton, a collection of proteins responsible for both giving cells shape and creating movement. For example, drastic cell deformation driven by the cytoskeleton is required for morphogenesis [5–7] and wound healing [8–10]. While there are

other important components such as microtubules and intermediate filaments, in this work I focus on one essential cytoskeletal protein—actin.

1.1.2 The Actin Cytoskeleton

Actin is an ancient and highly conserved protein that is found in all branches of life [11]. It is one of the most abundant proteins in eukaryotic cells and a primary component of the cytoskeleton [12]. It helps provide structure, so studying actin mechanics often directly translates towards better understanding the physical aspects of cells [13–17]**.** Actin has many roles, which it accomplishes through the use of myriad binding proteins. Cross-linkers and nucleators form actin into parallel bundles in filopodia, antiparallel bundles in stress fibers, cross-linked networks in the cortex, or branched networks in lamellipodia [18], along with countless other structures. Through actin, myosin exerts contractile forces [15] and transports various cellular components [19]. Actin also helps drive cell motility [5,20,21]**.** As such, actin provides an ideal model system for studying the mechanics of cells. These studies lead both to better understanding of cells and inform the creation of novel, biological inspired materials.

As a biopolymer, actin is composed of protein monomers that polymerize to form long filaments. As is convention, this work will refer to unbound monomers as G-actin, standing for globular actin, while calling monomers in filaments F-actin for filamentous actin. Actin monomers are 42 kDa proteins which bind either ATP, ADP with a phosphate (ADP-Pi), or ADP alone [12]. I will use ATP- or ADP-actin to denote monomers bound to the appropriate form of adenine. While monomers themselves have a width of only 5.5 nm [22], thousands of monomers form filaments with lengths of several microns. Such filaments have a natural helicity and form a right-handed, two-start helix that repeats every ~72 nm [22,23]. This twist can be altered, however, through the binding of proteins such as cofilin [24,25] or the application of mechanical

force [23]. I further discuss the dynamics of individual filaments in Section 1.3, while Section 1.4 focuses on larger actin networks.

1.2 Reconstituted Actin Networks

1.2.1 Forming Networks *In Vitro*

The large number of actin binding proteins and simultaneously occurring cellular processes complicate the study of actin in cells. Instead, reconstituted networks can be formed *in vitro*, meaning outside of cells, to study simplify systems and isolate individual effects (Figure 1.1). Actin monomers, along with other actin binding proteins, can be purified from either animal tissue or genetically modified cells. For example, in this work actin is purified from powdered rabbit muscle, while several actin binding proteins were expressed in and purified from E. coli. Additionally, these proteins can be labeled with fluorescent dye to allow microscopic imaging. For information on how proteins are purified and labeled for this work, see Appendix A.2.

At sufficiently high salt concentrations, G-actin will polymerize into filaments. Networks can thus be formed by combining purified actin with other desired components in high salt buffers. Depending on the experiment, G-actin is either added directly to the chamber where it then polymerizes, or pre-polymerized in aliquots with the resulting F-actin being added later. In addition to actin, various actin binding proteins, which are further discussed in Sections 1.3 and 1.4, macromolecular crowding agents, and drugs can be added to samples to create experimental systems with desired properties and test the effects of various manipulations. Crowding agents, in this work the globular protein methylcellulose, deposit actin to the bottom of an imaging chamber due to depletion effects and create a quasi-two dimensional layer [26]. Drugs include latrunculin, which prevents G-actin from polymerizing into filaments [27], and phalloidin, which

strongly binds actin filaments and prevents depolymerization [28]. In this work, such networks are prepared for use in either imaging chambers for microscopy or on a rheometer. Microscopy is discussed in the following section, while rheology is discussed in Section 1.4.2.

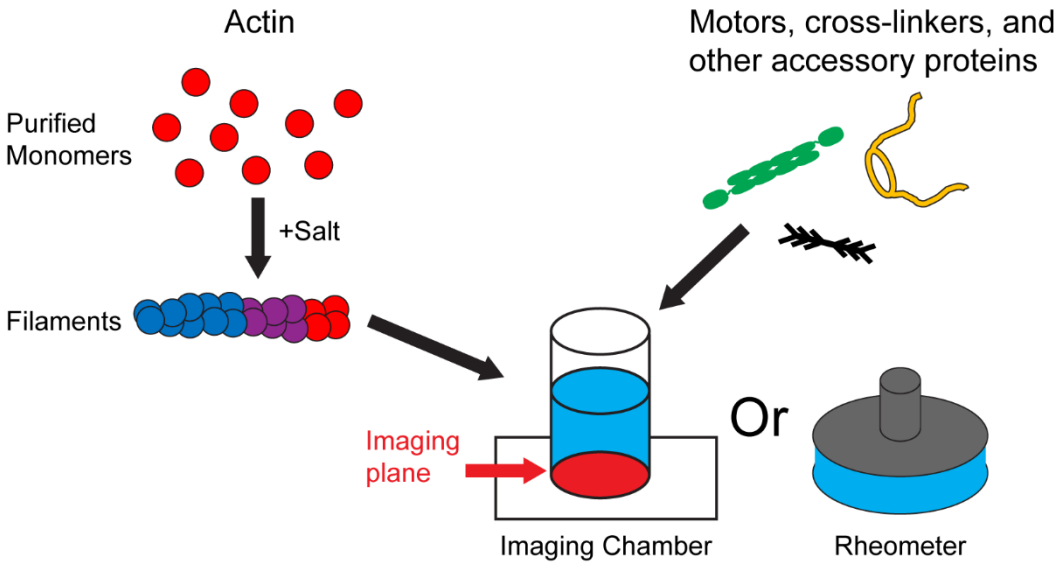

Figure 1.1: Cartoon of *in vitro* assay. This work uses *in vitro* assays composed of purified actin monomers, which polymerize into filaments at sufficiently high salt concentrations, along with other accessory proteins such as cross-linkers and molecular motors. Components are added either to a rheometer or to a cylindrical imaging chamber, the bottom of which is illuminated by a laser.

1.2.2 Microscopy

For imaging, proteins are labelled with fluorescent dyes that emits light when excited by a particular wavelength photon. Such labeling allows imaging of macromolecules smaller than the wavelength used, and proteins can be imaged using visible light. When excited by a laser, the dyes emit longer wavelength light. Since the emission spectrum of each dye is known, other wavelengths can be filtered out so only one component is visualized at a time. Using different dyes for different proteins therefore allows simultaneous imaging of several proteins by sequentially illuminating the sample with multiple lasers. Such a process produces images for each protein, which can later be combined. However, illumination with sufficiently high

intensity light, or over long time periods, will irreversibly damage the dye. This damage, called photobleaching, reduces the duration for which a sample can be imaged and is thus often avoided. For this work, I reduce photobleaching through the addition of an oxygen scavenger systems composed of glucose oxidase and catalase which reduces oxidation, one cause of bleaching [29,30]**.** However, photobleaching can also be used constructively, such as in fluorescence recovery after photobleaching (FRAP) assays where intensity recovery of a photobleached region informs on protein dynamics. FRAP is discussed further in Chapter 4.

For this work, networks are imaged in a chamber composed of a glass cylinder epoxied to a silane-treated coverslip. Since these chambers are open at the top, they easily permit the later addition of proteins or other reagents. Silane treating the coverslips allows the use of an oil-surfactant layer, which prevents the adhesion of proteins to the glass. Submitting the coverslip to UV/ozone will remove exposed silane, causing the oil-surfactant to only stick to part of the coverslip. Placing a Teflon mask at the coverslip center then subjecting to UV/ozone removes silane from the chamber edges. This process creates a boundary of stuck, stationary actin at the border between silane and untreated glass, which reduces bulk flows in space spanning networks. More details on the preparation of the oil-surfactant and imaging chambers are given in Appendix A.3.

This work utilizes two methodologies for microscopy. In confocal microscopy, light passes through the same pinhole twice, before and after illuminating the sample. This process focuses light to a thin vertical plane anywhere in the sample then excludes out of focus light from reaching the camera, allowing imaging of a single vertical slice. The other technique, total internal reflection fluorescence (TIRF) microscopy, takes advantage of induced evanescent waves to image a narrow region at the bottom of a sample with minimal background. In TIRF

microscopy, a laser is directed towards the coverslip at above the critical angle for total internal reflection, causing the laser to completely reflect at the interface between the coverslip and the sample. The specimen is illuminated by the resulting evanescent wave, which only reaches a narrow region adjacent to the coverslip. Both of these methods enable imaging of a thin vertical slice. However, the thickness of the oil-surfactant layer excludes the use of TIRF as the evanescent wave no longer reaches the sample. Confocal microscopy is thus used for the majority of this work, except for in Section 4.4.1 when higher resolution is needed.

1.3 Dynamics of Individual Actin Filaments

1.3.1 Filament Nucleation, Growth, and Depolymerization

Even without other regulatory proteins, individual actin filaments undergo complex nucleation and polymerization dynamics. To form filaments, monomers first nucleate into dimers and trimers, a slow process that limits the rate of polymer development [12]. Proteins such as formins, profilin, and arp2/3 regulate this nucleation rate. Formins, for example, enhance actin nucleation [31,32]. In contrast, profilin greatly reduces the spontaneous nucleation of actin monomers into oligomers [33]. After nucleating, the addition of a fourth monomer stabilizes filaments, which then grow as new monomers bind to their ends [12]. Growth rate depends on the concentration of G-actin and is further regulated through actin binding proteins. For instance formin, in conjunction with profilin, increases the polymerization rate of actin [34].

Once formed, actin filaments are polar on both a molecular level and due to ATP activity. First, the monomers themselves are polar, resulting “barbed” and “pointed” ends of a filament [22] which have different rates of polymerization and depolymerization (Table 1.1) [12]. The binding rate is equal to $k_{on} * [G - actin]$, where brackets denote concentration, while the

unbinding rate is k_{off}. Note that while unbinding rate is intrinsic to actin and concentration independent, binding rate depends on the concentration of G-actin since it is diffusion limited [12]. As a result, at a critical concentration of G-actin equal to k_{on}/k_{off}, polymerization and depolymerization occur at the same rate. Above this critical concentration, filaments grow, while they shrink at lower concentrations. Since the critical concentration is higher at the pointed than the barbed end, as G-actin is depleted during filament growth its concentration reaches a point where polymerization is occurring at the barbed end, while pointed ends depolymerize. Steady state thus occurs when

$$k_{on}^{b} * [G] - k_{off}^{b} + k_{on}^{p} * [G] - k_{off}^{p} = 0 \quad 1.1$$

where k^b and k^p are the rates at the barbed and pointed end, respectively, and $[G]$ is the concentration of G-actin. At this concentration, polymerization at the barbed end balances depolymerization at the pointed end (Figure 1.2A) [35]. This process is called treadmilling and is a subset of turnover, which includes any process where the constituent monomers in a filament are constantly being replaced. Turnover is discussed further in the next section.

ATP activity further enforces this polarity. Before polymerizing into filaments, G-actin binds ATP. In fact, ADP bound to G-actin is replaced with ATP over the course of ~60 s, a process accelerated by profilin [12]. Once polymerization occurs confirmational changes causes the ATP to hydrolyze on the order of ~3 s [36] and release the phosphate on time scales of minutes [37]. F-actin thus ages as ATP hydrolyzes to ADP-Pi then ADP. Due to treadmilling, barbed ends contain newer monomers compared to pointed ones. As a result, filaments eventually develop a cap where they have ATP and ADP-Pi bound at the barbed end and ADP at the pointed one [38]. This cap amplifies the difference in binding and unbinding rates between the two ends (Table

1.1) [12], accelerating treadmilling. Since ATP and ADP-Pi have similar polymerization and depolymerization rates [12], for simplicity I will henceforth use ATP to encompass both states when discussing actin dynamics.

	k_{on} (μM^{-1} s^{-1})	k_{off} (s^{-1})	Critical Concentration (μM)
Pointed End			
ATP	1.3	0.8	0.6
ADP	0.16	0.3	2.0
Barbed End			
ATP	12	1.4	0.12
ADP	4	8	2.0

Table 1.1: Binding rates, unbinding rates, and critical concentrations for both ends of actin filaments depending on whether ATP or ADP is bound. ADP-Pi-actin has comparable rates to ATP-actin. The binding rate is given by $k_{on} * [G - actin]$, while the unbinding rate is k_{off}. Critical concentration is equal to k_{on}/k_{off}. Data is taken from [12].

1.3.2 Turnover and Cofilin

As discussed in Section 1.1, the cytoskeleton must rapidly adjust to external stimuli. To this end, actin is constantly being restructured**.** Actin in cells undergoes a dynamic process called turnover, where filaments continuously polymerize on their barbed ends while depolymerizing on their pointed ends [21]. This process is essential in cells and when it is prevented, for example with the addition of the drug phalloidin, they die [28]. Cells therefore must be able to regulate the rate of actin turnover, and they possess many methods towards this purpose. While treadmilling is one such method, it is slow. Using the rates in Table 1.1 and assuming an ATP-bound barbed end and ADP-bound pointed end, Equation 1.1 can be used to estimate the steady state treadmilling rate. By this calculation, steady state occurs at $[G] = 0.13$ μM with a turnover rate given by $k_{on}^{b} * [G] - k_{off}^{b} = 0.21$ monomers/s, comparable to the experimentally measured

values [39–41]. Converting to length using ~1 monomer per 2.7 nm in a filament [42] yields a rate of 2 μm/hr. It thus takes hours for a several micron long filament to completely turnover via treadmilling, negligibly slow compared to cellular processes that can occur on timescales of seconds to minutes. Instead of relying on treadmilling, cells possess a myriad of proteins to regulate turnover by controlling the rate of polymerization, severing, and depolymerization of actin filaments [12,18].

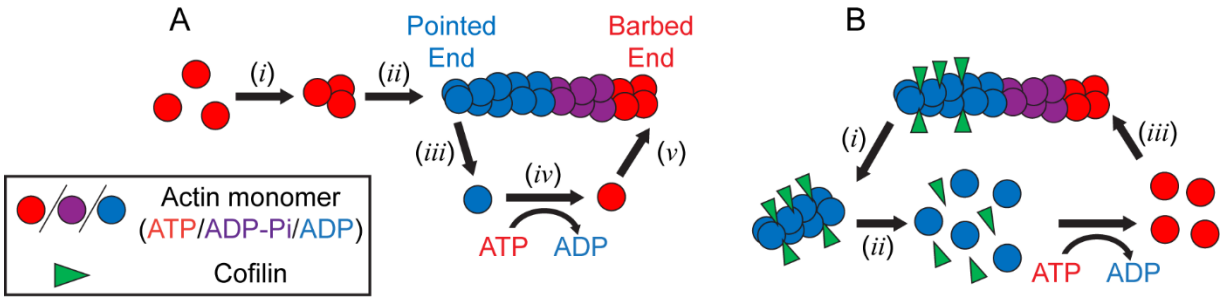

Figure 1.2: Actin nucleation and turnover. (A) Cartoon depicting nucleation and treadmilling of actin filaments. (*i*) G-actin nucleates into trimers that then (*ii*) grow into full filaments. (*iii*) Filaments continuously depolymerize at the pointed end while (*v*) growing at the barbed end through the binding of ATP-actin monomers. (*iv*) ADP bound to G-actin is replaced with ATP. (B) Cartoon depiction of cofilin mediated turnover. (*i*) Cofilin binds to the pointed end of actin, where it enhances severing at the boundary between coated and naked filaments. (*ii*) The cofilin-coated daughter filament then depolymerizes, adding monomers to solution that can (*iii*) repolymerize on the barbed end.

One important protein behind the regulation of turnover is cofilin, which enhances the severing rate of actin. This severing has been found to be necessary for turnover in cells [43,44]. Cofilin has also been found to accelerate turnover *in vitro* to 15 times the rate of treadmilling alone [41]. To sever actin, cofilin binds preferentially to ADP-actin at the pointed end (Figure 1.2B) [45]. This binding is cooperative, and new cofilin is more likely to bind adjacent to bound cofilin [46]**.** Cofilin-coated actin is more flexible than uncoated actin [47], creating a mechanically weak point at the boundary between coated and naked filament [48]. The filament then severs at this point due to thermal fluctuations [48,49]. Since cofilin mediated severing

occurs at boundaries, it depends non-monotonically on concentration and is maximized when cofilin concentration is half that of actin [49]. Cofilin binding also increases the helicity of actin filaments, which can induce torsional stress capable of severing filaments [24,25]. After severing, one of the daughter filaments—the segment that was previously the pointed end—contains "older" monomers that are likely ADP-bound. This filament now has ADP-actin at both the barbed and pointed ends, so the critical concentration at both ends is 2 μM (Table 1.1) [12], which is higher than the previously calculated steady state concentration of 0.13 μM. One of the daughter filaments is thus unstable and depolymerizes; cofilin accelerates this process [50].

1.3.3 Filament Mechanics

Physically, these filaments act as semi-flexible rods. Their width, at ~8 nm, is about a thousand times smaller than their length, which varies in cells but reaches lengths of microns [18]. Furthermore, at physiological temperatures, actin has similar contour and persistence lengths. Persistence length measures the length scale at which thermal and buckling energy are equivalent and is defined as $l_p = EI/k_bT$, where E is the Young modulus, I is the geometric moment, k_b is Boltzmann's constant, and T is the temperature [51]. Filaments much shorter than their persistence length act as rigid rods, while longer filaments are compacted by thermal forces [18]. For actin at physiological temperatures, $l_p \sim 10$ μm [23]. Since actin's contour length is comparable to l_p, absent other forces thermal energy will buckle but not completely contract filaments. As a result of this buckling, actin acts as an entropic spring. Stretching filaments reduces entropy, as there are fewer bending configurations that connect the two ends, and thus costs free energy. Additionally, the required force is nonlinear and rapidly increases as actin is stretched [23]. This nonlinearity is called strain stiffening.

1.4 Structure and Mechanics of Actin Networks

1.4.1 Actin Binding Proteins Tune Network Architecture

Cells utilize many regulatory proteins to control the local architecture of actin based on the necessary function. Depending on the presence and concentration of actin binding proteins, as well as the polymerization conditions, actin *in vitro* forms various structures (Figure 1.1) [18,52–54]. At sufficiently high concentrations, actin forms entangled networks which are kinetically arrested and stuck away from their equilibrium state [55,56]. Their structure thus depends on initial conditions and is affected by proteins that impact nucleation or growth rate of actin [56–58]. The nucleator arp2/3 also more directly tunes structure by forming branched networks [59]. In addition to modifying nucleation and growth rate, proteins can regulate actin architecture by functioning as cross-linkers. These proteins vary from short and rigid cross-linkers, such as fascin, to long and flexible ones, such as filamin [60,61]. The physical properties and concentration of these proteins define actin architecture. For instance, varying cross-linker conditions forms structures such as space-spanning networks of individual filaments, cross-linked networks of bundles, and individual bundles [52–54]. Three different cross-linkers are used in this work: α-actinin, and two homologs of filamin. α-actinin is a rigid, ∼35 nm long protein [62]. At 40 nm, dictyostelium discoideum filamin (ddFLN) is about the same length as α-actinin, but it is much more flexible [60,63]. Human filamin (FLN) is similarly flexible, but with a contour length of approximately 160 nm [64]. FLN and α-actinin can form either cross-linked networks at lower concentrations or bundles at sufficiently high concentration [52,53]. These cross-linkers thus control the structure of actin networks. Next, I will talk about how through these changes to structure, cross-linkers influence the mechanics of actin.

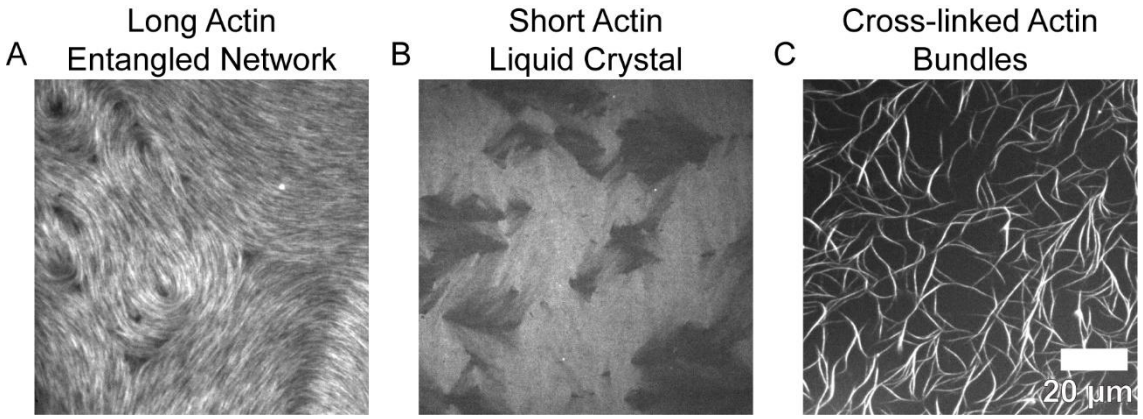

Figure 1.3: Actin binding proteins regulate actin network architecture. (A) Without other regulatory proteins, long actin forms entangled networks. (B) When length is shortened using 20 nM of capping protein, actin instead forms liquid crystals. Intensity corresponds to local filament orientation. (C) The cross-linker α-actinin bundles actin at high concentrations (here 1 μM). All images from networks with 2 μM actin.

1.4.2 Viscoelasticity and Rheology Depend on Structure

The mechanical properties of actin networks are intrinsically linked to their structure. As such changes to architecture similarly affect material aspects. To observe its effect, a rheometer can be used to direct measure the material properties of actin networks (Figure 1.4). A rheometer is a device that studies properties of fluid or viscoelastic materials by measuring relationship between strain and stress. It can take on different geometries, but for this work I exclusively use parallel plates where two plates rotate relative to each other, shearing a material placed in between. The rheometer then measures the relationship between strain, γ, and stress, σ, which are defined as

$$\gamma = \frac{\Delta x}{h} \tag{1.2}$$

$$\sigma = \frac{F}{A} \tag{1.3}$$

where Δx is horizontal displacement, h is the height in between the two plates, F is the force exerted by the plates, and A is plate area (Figure 1.4A). Strain is non-dimensional displacement, whereas stress is the pressure exerted by the plate.

Actin networks form a viscoelastic material, meaning they have properties of both fluids and solids [58,65]. When shearing an idealized elastic solid, stress depends only on strain as $\sigma = G * \gamma$, where G is the shear modulus of the material. For fluids, stress depends instead on the strain rate, $\sigma = \eta * d\gamma/dt$, where η is viscosity and t is time. [66]. For complex materials, G and η need not be constant in nonlinear materials but instead could depend on other variables such as γ or $d\gamma/dt$. In viscoelastic materials, stress depends on both the strain and strain rate. While many models describe these materials, a useful one represents the sample as the sum of a viscous and elastic material, with

$$\sigma = G'\gamma + G"d\gamma/dt \tag{1.4}$$

where G' and $G"$ are the elastic and viscous moduli, respectively. G' represents the storages of elastic energy in the material, while $G^{"}$ measures dissipation of energy due to viscous forces. Experimentally, these moduli can be measured by exerting a cyclical strain $\gamma = \gamma_0 \sin(\omega t)$. Plugging this strain into Equation 1.4 gives a corresponding stress of

$$\sigma = \gamma_0[G^{'} \sin(\omega t) + \omega G" cos(\omega t)] \tag{1.5}$$

Note that the part of the response due to elasticity is in phases with the applied strain, while the viscous response is out of phase. G' and $G"$, which often depend on frequency, are calculated by fitting the measured stress to Equation 1.5 [66]. The relative viscosity to elasticity is measured through the phase angle $\phi = arctan[G"/G']$, where $\phi = 0$ for purely elastic materials and $\phi = \pi/2$ for purely viscous fluids. ϕ is also frequency dependent, and at a characteristic timescale the

material transitions from being predominantly viscous to predominantly elastic. For uncross-linked actin networks, this transition occurs at ~0.01-0.1 s depending on concentration [65]. Phase angle, along with viscous and elastic moduli, also depends on network architecture and can be changed through the addition of cross-linkers [53,67–70] or by altering the concentration [65] or length of actin [71].

Many materials are nonlinear with G' dependent on strain. In such cases, the differential modulus $K = d\sigma/d\gamma$ better represents material properties. K can be thought of as a local elastic constant, representing the local limit of the linear elasticity $G' = \sigma/\gamma$. One relevant example of nonlinear materials is strain stiffening, where K increases with strain. The opposite response, where K decreases with strain, is called strain softening. Depending on the concentration and type of cross-linkers present, actin can have a linear, strain softening, or strain stiffening response to shear [15,23,54,72]. In networks that are either uncross-linked or have low cross-linker concentration, strain is distributed heterogeneously, and filaments deform primarily through bending, leading to a linear or strain softening shear response. In contrast, sufficient cross-linker concentration leads to affine deformations where all filaments are stretched equally. In this regime the network strain stiffens due to the nonlinearity of individual filaments [23,72]. However, increased cross-linker concentration does not always lead to affine deformations. For example, networks containing the short, rigid cross-linker fascin can strain stiffen as previously described. However, fascin bundles actin at high concentrations, resulting in less-well connected networks that soften under shear [54]. Rheology at high strains thus depends not only on cross-linker concentration, but also on the physical properties of the cross-linker and the structures that they produce.

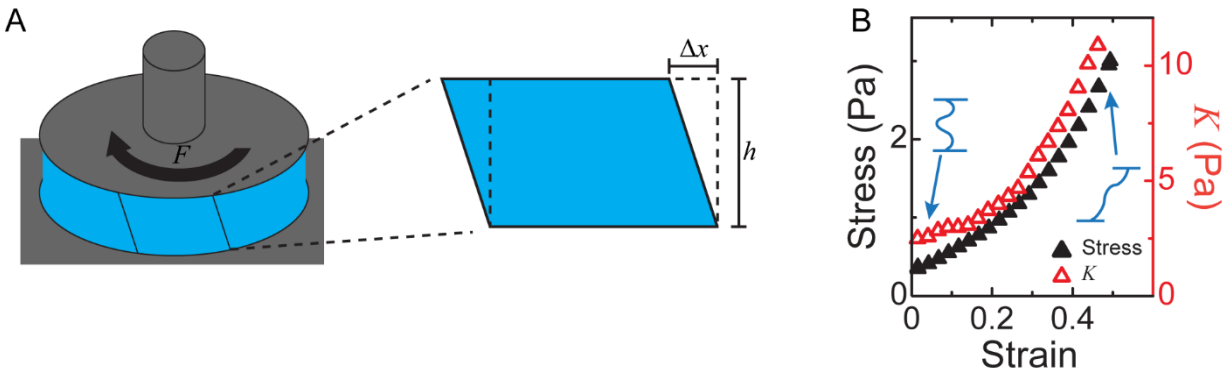

Figure 1.4: Rheology and strain stiffening. (A) A parallel plate rheometer is composed of two plates separated by distance h. The top plate of area A rotates, exerting force F and shearing a fluid to displacement Δx from its original position depicted by the dotted rectangle. The rheometer measures stress and strain, as defined in Equations 1.2 and 1.3 (B) Stress (closed black triangles) and differential modulus $K = d\sigma/d\gamma$ (open red triangles) as a function of strain in a cross-linked actin network. This network is sufficiently cross-linked to shear stiffen, demonstrated by the increase in both variables with strain, due to affine stretching of nonlinear filaments.

Mechanical forces can also change the structure and rheological properties of actin networks, leading to materials that adapt to external stress. Schmoller *et al*. found that at low cross-linker concentrations, actin networks irreversible weaken when cyclically sheared to high strains, similar to the classic Mullins effect. On the other hand, at high cross-linker concentrations, the networks instead irreversibly harden under cyclic shear. By combining rheology with confocal microscopy, they found structural changes that occurred during repeated shear, leading to the observed hardening [73]. Actin networks have also been recently found to reversibly adapt their structure to external stress. Majumdar *et al*. observed that after the application of a large stress, networks had an asymmetric strain response where more force was required to shear in the direction of the previously applied stress than in the opposite direction [74]. Simulations found that filament alignment can lead to such asymmetry, suggesting it originates from actin aligning under applied stress [74,75]. This response is called mechanical hysteresis and is discussed further, including original research into its origin, in Chapter 3.

1.4.3 Liquid Crystal Structure and Properties

In addition to forming cross-linked networks, actin binding proteins can regulate structure by shortening filaments and inducing a liquid crystalline state (Figure 1.3B). Many proteins regulate filament length. Capping protein for instance decreases average length by binding to the barbed end of growing filaments and preventing the addition of new monomers [76]. Proteins that increase the nucleation rate of actin also lead to more, but shorter, filaments. A higher formin concentration, for example, increases the number of actin filaments and thus decreases their length as the same number of monomers are spread between more filaments [41]. Shortening actin in this regard drastically alters its structure. When actin becomes sufficiently short compared to its persistence length, it acts as a rigid rod and forms a state called a liquid crystal (Figure 1.3B) [42,77,78]. Such a state occurs when rod-like particles entropically align at high concentrations but remain positionally disordered [79]. This alignment is called nematic ordering and is described by the nematic vector field $\hat{n}$ that traces local alignment. Distorting $\hat{n}$ costs energy, so nematic ordering imparts elasticity to the fluid. In Frank-Oseen elastic theory, elastic energy density of a liquid crystal is given by

$$f = \frac{1}{2}K_{11}(\nabla \cdot \hat{n})^2 + \frac{1}{2}K_{22}(\hat{n} \cdot \nabla \times \hat{n})^2 + \frac{1}{2}K_{33}\left(\hat{n} \times (\nabla \times \hat{n})\right)^2 - \frac{1}{2}K_{24}\nabla \cdot [\hat{n}(\nabla \cdot \hat{n}) + \hat{n} \times (\nabla \times \hat{n})] \quad 1.6$$

where the four Ks are material properties representing the energy penalty for splay (K_{11}), twist (K_{22}), bend (K_{33}), and saddle-splay (K_{24}) deformations. A common simplification assumes $K_{11} = K_{22} = K_{33} = K_{24} \equiv K$, where K is the Frank elastic constant. This elasticity depends on the aspect ratio of the rods [77,80,81], and in actin liquid crystals the ratio of bend to splay modulus has been found to increase with filament length [77]. While orientational order imparts

an elasticity, positional disorder allows fluid-like flows [80,81]. In addition to actin, nematic order has been observed in other biological materials including microtubules [82], amyloid fibrils [83], collagen [84,85], and fd virus [86].

Due to competition between elasticity and surface tension, liquid crystal droplets can take on an elongated, spindle shape called a tactoid [42,83,87–91]. Proteins that shorten filaments can thus control shape and elasticity of actin by inducing a liquid crystalline state. Liquid crystals and tactoids are discussed further in Chapter 2.

1.4.4 Actomyosin Networks

Another protein important for deforming and restructuring actin is myosin, a family of molecular motors with active head regions. Myosin heads bind to actin then undergo a powerstroke motion, after which they unbind and repeat the cycle. This cycle hydrolyzes ATP and myosin uses the resulting energy to exert a force that can propel either itself or the actin [92–94]. Importantly, such force is directional. With the exception of myosin VI, all myosins move towards the pointed end of actin [92]. This work focuses on myosin II, which has the unique feature where hundreds of individual myosin monomers polymerize into filaments [93]. Due to its plethora of heads, myosin II exerts large forces and can induce flows in actin networks.

Myosin II can induce contractile or extensile forces and flows depending on the architecture of actin networks. One of myosin's roles in cells is to exert contractile forces. In some cases, such as in muscle cells, contraction occurs due to ordered structures of antiparallel actin [94,95]**.** However, cells contain disordered networks that also contract, and myosin similarly generates contractile flows in isotropic reconstituted networks, condensing actin into asters [96,97]. In this case, contraction occurs due to buckling, which breaks the symmetry between contractile and extensile forces. Myosin is able to contract actin, but extensile forces buckle filaments and are

thus unable to produce flows [96]. As a result, myosin forces are sensitive to changes in actin structure that impact buckling. When buckling is prevented by either cross-linking actin into rigid bundles or shortening filaments well below their persistence length, myosin instead produces extensile forces [78,97]. Increasing cross-linking between bundles, however, restores contractions due to arrested sliding [97]. Reymann *et al*. also found that myosin induced deformations depend on network architecture, with parallel filaments aligning and extending, while antiparallel filaments contract [98]. Overall, the forces and flows generated by myosin depends on the structure of the affected network.

1.4.5 Reciprocity of Turnover with Structure and Mechanics

Finally, turnover dynamics both affect and are affected by network structure and mechanical properties, although these effects are poorly understood. While cross-linkers greatly impact network structure and mechanics, their effect on turnover is less well studied. Cross-linkers have been found to dampen thermal fluctuations [99]. Since cofilin-mediated severing depends on these fluctuations, changes in actin architecture that affect them could have a similar impact on cofilin activity. Indeed, structure has been found to influence cofilin severing, with faster disassembly in branched versus bundled actin [100]. Previous research has also investigated the role of cross-linkers on disassembly, finding that cofilin severing is enhanced by bundling with either fascin [101] or biotin and neutravidin [25], a method of permanent cross-linking which also creates short, rigid bonds. Wioland *et al.* attributed this increase in severing to the introduction of twist constraint, which increased the torsional stress generated by cofilin binding [25]. However, it is unclear whether a similar effect would occur in actin cross-linked by longer or less rigid cross-linkers which might provide less restraint than their shorter counterparts.

Myosin has also been linked to actin depolymerization and turnover. It has been found to be able to disassemble actin in cells [35] and to be essential for turnover in cytokinesis [102,103] and neuronal growth cones [104]. This role in turnover is supported by reconstituted networks where myosin has similarly been shown to be able to disassemble actin [98,105] and, through buckling, to sever filaments [96,106]. Recently, myosin disassembly of branched, membrane-bound actin *in vitro* was found to be able to facilitate the assembly of new filaments [107]. The underlying mechanics behind this process, however, are poorly understood and it is unclear whether it will persist in different actin architectures.

While simulations show turnover can affect myosin induced flows, such effect has not been studied experimentally. Turnover has been found to increase the phase angle ϕ in actin networks, making them behave more like viscous fluids [41]. McCall *et al*. found that above frequencies of ~0.1 Hz, increased turnover rate decreased G', with minimal effect on $G"$. Such fluidization was attributed to increased relaxation of stress. Disassembly of stretched actin dissipates stress, while actin repolymerizes in a relaxed state [41,108]. Turnover therefore might dissipate myosin generated stress, influencing flows and forces in actomyosin networks. Indeed, simulations have found that turnover regulates myosin activity by tuning its ability to both sustain stress over time and contract actin into asters [109–111]. Tubule growth rate was similarly observed to control flows in networks of microtubules and molecular motors. Fast growth rates led to extensile flows and nematically aligned microtubules, while slower rates led to contractile flows and polar asters [112]. However, the effects of turnover on actomyosin stresses and flows have not been experimentally studied. As discussed in Section 1.3.2, turnover is negligibly slow *in vitro* without other regulatory proteins, especially compared to myosin induced contractions which occur on the order of minutes. Turnover is thus minimal in previous reconstituted actomyosin

networks. Understanding how turnover impacts these flows is essential towards applying knowledge about myosin activity from *in vitro* assays to cells, where turnover occurs at a much faster rate.

1.5 This Work

This work investigates the connection between three aspects of actin networks: structure, mechanics, and dynamics. I first examine both how different structures affect the material properties of a network, and how mechanical response modifies structure. As discussed in Section 1.4, structure and mechanics are intrinsically linked, and I further investigate their connection. In Chapter 2, I describe how actin can change internal structure by adding nematic order to otherwise anisotropic droplets. Here, I form composite, demixed droplets composed of short actin and FUS, a protein previously found to phase separate *in vitro* [113]. Changing actin concentration and length tunes both the shape and the physical properties, such as viscosity and elasticity, of these droplets. Using a bipolar tactoid model, I show how changing actin length influences the material properties and leads to droplet shape. While these droplets show how to create droplets with tunable shape and mechanics, I next investigate how changes to structure in existing networks. In Chapter 3, I discuss how actin networks can adapt to external stimuli by varying their rheological properties through structural changes. I investigate cross-linked networks of long actin that develop long-lasting but reversable changes to rheological properties after the application of stress. By changing the concentration and properties of the cross-linkers in both experimental and simulated networks, I find that this response, called mechanical hysteresis, stems from structural changes where initially disordered filaments align under stress. I further find that hysteresis depends on strain stiffening in the initial network. In these droplets

and networks, alignment of actin, whether formed initially or in response to mechanical stimuli, defines the material properties.

Finally, in Chapter 4 I investigate how actin architecture and myosin generated stress can regulate the dynamics of actin turnover. As previously observed, cofilin increases the turnover rate of actin *in vitro* [41]. In contrast, I find that bundling actin through the addition of α-actinin prevents cofilin mediated severing of actin and thus arrests turnover. I further find that myosin buckling and severing of actin enhances turnover. Remarkably, myosin enhances severing even in bundled networks, suggesting that different methods of severing actin might not only be possible in cells, but might also be necessary depending on local architecture. Additionally, I investigate the effect of actin dynamics on myosin generated stresses, and find that increasing turnover leads to faster, but less contractile, flows.

CHAPTER 2

TUNING SHAPE AND INTERNAL STRUCTURE OF PROTEIN DROPLETS VIA ACTIN FILAMENTS

2.1 Preface

This chapter is adapted from Scheff *et al.* 2020 [114]. All experiments were conducted and analyzed by the author, except for the polscope imaging which was conducted by Kimberly Weirich and Avinash Patel. Kimberly and Avinash also initially observed composite FUS-actin droplets, and Kimberly provided experimental guidance. Kinjal Dasbiswas developed the quasi bipolar model with input from Suriyanarayanan Vaikuntanathan. Margaret Gardel provided guidance at every step.

2.2 Introduction

Liquid condensates, dense macromolecular droplets that phase separate out of a dilute suspension, are widespread in soft and biological materials ranging from coacervates [115] to membraneless organelles [116]. The formation and material properties of condensates can be tuned through modifying macromolecular composition [117–119] or environmental conditions [120–122]. Intriguingly, the fluid condensates typically adopt a characteristic spherical shape and coalescence over time, indicative of droplets composed of an isotropic liquid with a dominant interfacial tension. However, macromolecules are inherently structured, often with significant rigidities and size, which may impart anisotropy to these liquids.

It is well appreciated that highly anisotropic rod-like objects can form structured liquid phases [79,123], which changes the shape of droplets. Liquid crystal droplets are observed to nucleate out of a dense isotropic suspension at the isotropic-nematic phase transition [83,90,91] or out of dilute suspensions through the addition of depletants or cross-links [42,88,89]. The competing effects of elasticity and surface tension in the droplets results in an elongated, spindle shape called a tactoid [87]. Due to different scaling of bulk and interfacial properties, the droplet shape is size-dependent [90,91] and is predicted to transition from spherical to tactoid [87,124]. Tactoids have been observed to form from a range of anisotropic components, including fd virus, biopolymer filaments, carbon nanotubes, and inorganic oxides [42,90,91,125–128]. Recently, nematic droplets with tunable shape were achieved by inducing attraction of biopolymer filaments of actin with transient cross-links [42]. The extent to which rod-like components influence anisotropic properties of condensates such as protein-based droplets remains to be explored.

Here I create composite liquid droplets composed of FUS, a protein that forms condensates [113], doped with filaments the biopolymer actin to investigate the impact of anisotropic dopants on droplet shape and properties. I find that actin incorporates throughout FUS droplets, leading to a composite liquid phase. By varying actin filament concentration and length, the degree of the anisotropic effects on the liquid vary and result in tunable droplet shape. I find that the droplet shape is well described by a continuum model of a nematic droplet, where the nematic elastic energy arises from the actin filaments. These results indicate that rigid dopants can impart liquid crystallinity to otherwise isotropic droplets. Such composite droplets provide a new means to control material properties and shape of liquid condensates, with implications for designing both biological assemblies and soft materials.

2.3 Materials and Methods

2.3.1 Protein Purification

Monomeric actin (G-actin) is purified as described in Appendix A.2. HisTag mouse capping protein is provided by Kimberly Weirich and is purified from bacteria using a procedure adapted from [129] and stored in a buffer composed of 10 mM Tris, 40 mM KCl, 0.5 mM DTT, 0.01 wt% NaN_3, 50 vol% glycerol, pH 7.5. FUS-GFP is expressed in and purified from insect cells as described in [113] by Avinash Patel and stored in a buffer composed of 2 mM Tris, 500 mM KCl, 1 mM DTT, pH 7.4. All proteins are flash frozen in liquid nitrogen and stored at -80°C. Actin and capping protein are used within three days of thawing, while FUS is used within 4 hours. After thawing, proteins are stored at 0-4°C until use.

2.3.2 Experimental Assay

The experimental chamber is composed of a glass cylinder (3166-10; Corning Life Sciences) epoxied to a glass coverslip (Fisherbrand, #1.5). The coverslip surface was passivated against protein adhesion through an oil-surfactant layer as described in Appendix A.3.

To polymerize actin filaments, 5 μM actin monomer (0.5 μM labelled with TMR) is added to a buffer composed of 2 mM Tris, 2 mM $MgCl_2$, 25 mM KCl, 0.5 mM ATP, 0.3 wt% methylcellulose, pH 7.4. To regulate actin filament length, capping protein is added to the final concentration of 50-150 nM. The actin is incubated for at least 30 min, while it polymerizes into filaments for at least 30 min, before 0.25 μM phalloidin is added to prevent dilution-induced depolymerization. Actin filaments are then mixed with 4.4 μM FUS resulting in a final mixture composed of 2 mM Tris, 2 mM $MgCl_2$, 45 mM KCl, 0.5 mM ATP, 0.04 mM DTT, 0.3 wt%

methylcellulose, 0.1 μM phalloidin. This mixture is immediately added to the sample chamber. Samples are incubated for 60 min before images are collected for droplet shape analysis.

2.3.3 Filament Length

I modulate the length of actin filaments through capping protein, which binds to growing filaments and prevents further polymerization, leading to an exponential distribution of filament lengths [76]. In the limit of strong binding, I approximate the average number of monomers in a filament from the ratio of actin monomers to capping protein, [Actin]/[Capping Protein]. I convert monomers to length using the known value of ~1 monomer per 2.7 nm in a filament, leading to average filament length of 2.7 nm*[Actin]/[Capping Protein] [42]. Pre-polymerizing the actin and stabilizing with phalloidin before mixing with FUS minimizes the influence of interactions between FUS and actin on actin filament polymerization and filament length. To further reduce artifacts associated with filament length, samples are compared only with other samples prepared on the same day when measuring the effect of actin and capping protein concentration. For measurements taken at different actin concentrations, the actin filaments in each sample are sourced from the same pre-polymerized stock. For different capping protein concentrations, all samples use capping protein sourced from the same aliquot.

2.3.4 Microscopy

Samples are imaged using a spinning disk confocal microscope (Nikon, Yokogawa) equipped with a CMOS camera (Andor) and 60x 1.2NA objective (Nikon). Samples are illuminated using a 491 or 561 nm laser (Cobolt). The polarization images were acquired on a home built LC-Polscope microscope constructed by Rudolph Oldenbourg at Marine Biological Laboratory in Woods Hole, MA [130]

2.3.5 Image Analysis

Droplet aspect ratio is calculated from droplet shape parameters extracted through ImageJ's built-in Analyze Particles function [131,132]. Images are thresholded and droplets in contact with another droplet or in the process of coalescing are excluded through visual inspection. Due to uneven illumination, droplets near the image edge may appear misshapen after thresholding; these droplets are similarly excluded. To extract the major and minor axes lengths, droplet shape is approximated as an ellipsoid. Droplet shape classification as tactoids or ellipsoids is determined through visual inspection of all droplets in a given field of view, excluding only those whose shape could not be confidently classified.

To estimate the amount of actin that partitions into droplets, the relative intensities inside to outside the droplet is calculated from images which have been background corrected by subtracting a dark image. Dark is defined as the average intensity without illumination, representing the camera dark levels. The average intensity inside of droplets is compared to the intensity within a ring between 1.4 and 3.2 μm from the droplet border, excluding anywhere within 1.4 μm of another droplet. The ratio between these values is calculated separately for each droplet to account for difference in illumination across the field of view. This ratio is then averaged across all measured droplets.

2.3.6 Quasi Bipolar Tactoid Model

The spindle shape of the tactoid is described naturally by a bipolar geometry obtained as surface of revolution of a circular arc about its chord, which corresponds to the major axis of the tactoid [87,133]. The size and shape of the tactoid is then completely prescribed by the length of its semi-major axis, R, and semi-minor axis, r, which together define the aspect ratio, R/r (Figure 2.5A). This parameter can vary from $R/r = 1$ for a spherical droplet to larger values for

more elongated droplets. Since I observe relatively spheroidal droplets ($R/r < 2.5$), I choose to work within the quasi bipolar tactoid model introduced in Ref. [134], where the nematic director lines, which follow the local average orientation of the comprising rods, meet "virtually" at points outside the droplet at a distance $2\tilde{R}$ apart (Figure 2.5A). When, $R = \tilde{R}$, I have the idealized bipolar tactoid configuration which arises only in the limit of very strong surface anchoring of the director to the tactoid surface. For the rest of this discussion, I define the parameters, $x \equiv R/r$ as the aspect ratio, and $y \equiv \tilde{R}/R$, the extent of the bipolarity of the director field. The optimal shape and director configuration of the droplet is then decided by a minimization of its total free energy with respect to these parameters.

If a nematic droplet is large relative to the scale of the comprising rods (here short, actin filaments), its free energy can be written as a sum of an elastic and a surface energy. This latter contains contributions from both the isotropic surface tension of the nematic fluid as well as the anisotropic surface tension or surface anchoring of the director to the droplet surface, γ_A. For the quasi bipolar tactoid model, I can scale out the size scale of the droplet (given by its semimajor axis, R) and write the total free energy in terms of the aspect ratio, x, and bipolarity parameter, *y*, as,

$$F(R;\, x, y) = KRf_{el}(x, y) + \gamma R^2(f_s(x) + \, \omega f_{an}(x, y))\,, \qquad 2.1$$

where K is the nematic elastic constant, γ is the surface tension associated with the droplet interface and ω is a dimensionless anchoring strength. The surface anchoring energy is defined as the energy cost of misalignment of the director, $\hat{n}$, with the surface described by its normal, $\widehat{N}$, such that the total anchoring free energy over the whole surface, S is, $\gamma_A \int_s ds \left(\hat{n} \cdot \widehat{N}\right)^2$, with $\omega = \gamma_A/\gamma$. Further, I use the equal Frank elastic constant approximation for bend and splay and

the saddle-splay term allowed for a finite surface is ignored since this just renormalizes the usual splay constant [134]. Although the bend and splay constants are in principle different [87], the equal constant approximation reduces the number of free fitting parameters in the model and captures the trends in droplet shape versus size. The volume of the tactoid similarly scales as $R^3 v(x)$.

These nondimensional shape factors, corresponding to surface tension, nematic elastic, and surface anchoring energy as well as the volume are calculated for the quasi bipolar geometry. This is done in the bispherical coordinate system (detailed in Refs. [134] and [135]) with coordinates $0 < \phi < 2\pi, 0 < \xi < \pi, 0 < \eta < \eta_0$, where $\eta_0 = 2tan^{-1}(1/x)$ is related to the aspect ratio of the tactoid. The corresponding scale factors in the bispherical coordinate system are defined as: $h_\phi = Z^{-1} sin\,\xi sin\,\eta$, $h_\xi = Z^{-1}$, $h_\eta = Z^{-1} sin\,\xi$ with $Z \equiv sin\,\xi sin\,\eta$. The shape factors defined in Equation 2.1 can be calculated in this coordinate system by performing the following integrals. Here I give the results directly based on the derivation given in Ref. [134].

$$f_s(x,y) = \int_0^{2\pi} d\phi \int_0^{\pi} d\xi \left(h_\phi h_\xi\right)|_{\eta=\eta_0} = 2\pi/x^2 \cdot (x + x^3 - (x^4 - 1)\tan^{-1}x^{-1}), \quad 2.2$$

$$f_{el}(x,y) = \int_0^{2\pi} d\phi \int_0^{\pi} d\xi \int_0^{\eta_0} d\eta \; h_\phi h_\xi h_\eta \, N^{-1} \cdot (4\cos^2\xi + \sin^2\xi\cos^2\eta), \quad 2.3$$

$$f_{an}(x,y) = \int_0^{2\pi} d\phi \int_0^{\pi} d\xi \left(h_\phi h_\xi\right)|_{\eta=\eta_0} (4N)^{-1} \cdot (y^2 - 1)^2 \cos^2\xi \sin^2\eta_0, \quad 2.4$$

$$v(x) = \int_0^{2\pi} d\phi \int_0^{\pi} d\xi \int_0^{\eta_0} d\eta \, h_\phi h_\xi h_\eta = \pi/(2x^3) \cdot (x + 2/3x^3 + x^5 - (x^2 - 1)(x^2 + 1)^2 tan^{-1} x^{-1}), \quad 2.5$$

with the factor N defined as,

$$N \equiv (\sin\xi\cos\eta + (1 + \sin\xi\cos\eta) \cdot y^2/2 - (1 + \sin\xi\cos\eta)^{-1})^2 + y^2 \sin^2\xi \sin^2\eta,$$

where the factors corresponding to surface area and volume can be calculated analytically in closed form, while those related to the nematic elastic energy and the anchoring energy are calculated by numerically integrating the expressions in Equations 2.3 and 2.4. It is readily checked that in the spherical limit, $x \to 1$, I recover the expected surface area and volume factors, and that in the elongated or high aspect ratio limit, $x \to \infty$, the surface area and volume scale as $R^2/x \sim R \cdot r$ and $R^3/x^2 \sim R \cdot r^2$ as expected for a cylindrical limit.

I now consider a tactoid of given volume, V, and find the shape parameters, x and y that minimize the total free energy. The free energy in Equation 2.1 can be re-expressed in terms of the tactoid volume and aspect ratio, by using $R = \left(V/v(x)\right)^{\frac{1}{3}}$, and expressed as a nondimensional free energy, $F(x, y, R)/\left(\gamma V^{\frac{2}{3}}\right)$, which depends on the tactoid aspect ratio and two nondimensional parameters: $K/\left(\gamma V^{1/3}\right)$, expressing the relative importance of the bulk nematic and surface tension energies, and ω. The equilibrium shape, and therefore the aspect ratio, of a tactoid of a given volume, V, and given material properties, K, γ, ω is found by numerically minimizing the nondimensional free energy with respect to the shape parameters, x and y. I employ standard numerical minimization techniques from the Mathematica FindMinimum function.

I then compare the equilibrium aspect ratio vs. tactoid size (in terms of the cross-sectional area which scales as $V^{2/3}$) for different values of the length scale, K/γ, to the corresponding experimentally measured values. By inspection, I choose three different curves for three different K/γ values that best describe and bound the data set obtained from averaging over the aspect ratio and area measurements of populations of tactoids. These fitting curves along with the experimental data are shown in Figure 2.5C and Figure 2.6. I note that not all tactoids in the

same experiment have the same material properties. I thus obtain a range of K/γ values for each experiment at a different capping protein concentration.

2.4 Results and Discussion

2.4.1 FUS and Actin Form Composite, Liquid Droplets

To investigate the impact of anisotropic components such as biopolymer filaments on protein droplets, I sought to form composite droplets out of FUS and actin filaments. The RNA-binding protein, FUS, is known to liquid-liquid phase separate into a protein-rich condensed phase upon a reduction in monovalent ion concentration [113]. Here, I form composite FUS-actin droplets by adding 4.4 μM FUS-GFP (FUS) to a solution containing pre-polymerized, fluorescent actin filaments (1 μM monomeric actin labeled with TMR, 1 mol% capping protein), which reduces the ambient monovalent salt concentration by an order of magnitude upon mixing, from 500 mM to 45 mM KCl (Figure 2.1A). Using fluorescence microscopy, I observe micrometer-sized condensates enriched with FUS, consistent with previous reports of FUS droplets [113]. Additionally, I find these droplets are also enriched with actin (Figure 2.1B). I find that the actin fluorescence uniformly colocalizes with the FUS fluorescence, indicating that these two proteins form composite droplets with apparent homogeneous distribution of both actin and FUS (Figure 2.1C). When I first observe FUS droplets (~10 min after mixing), they already contain concentrated actin, demonstrating that actin partitions into droplets relatively rapidly.

To quantify the partitioning of actin into the droplets, I compare the average actin intensity in the droplet interior, I_{inside}, to exterior, I_{outside}. Since fluorescence intensity is proportional to protein concentration, the intensity ratio, $I_{\text{inside}} / I_{\text{outside}}$, provides an estimate of the actin concentration inside the droplets relative to in the bulk solution [118,136]. At low actin

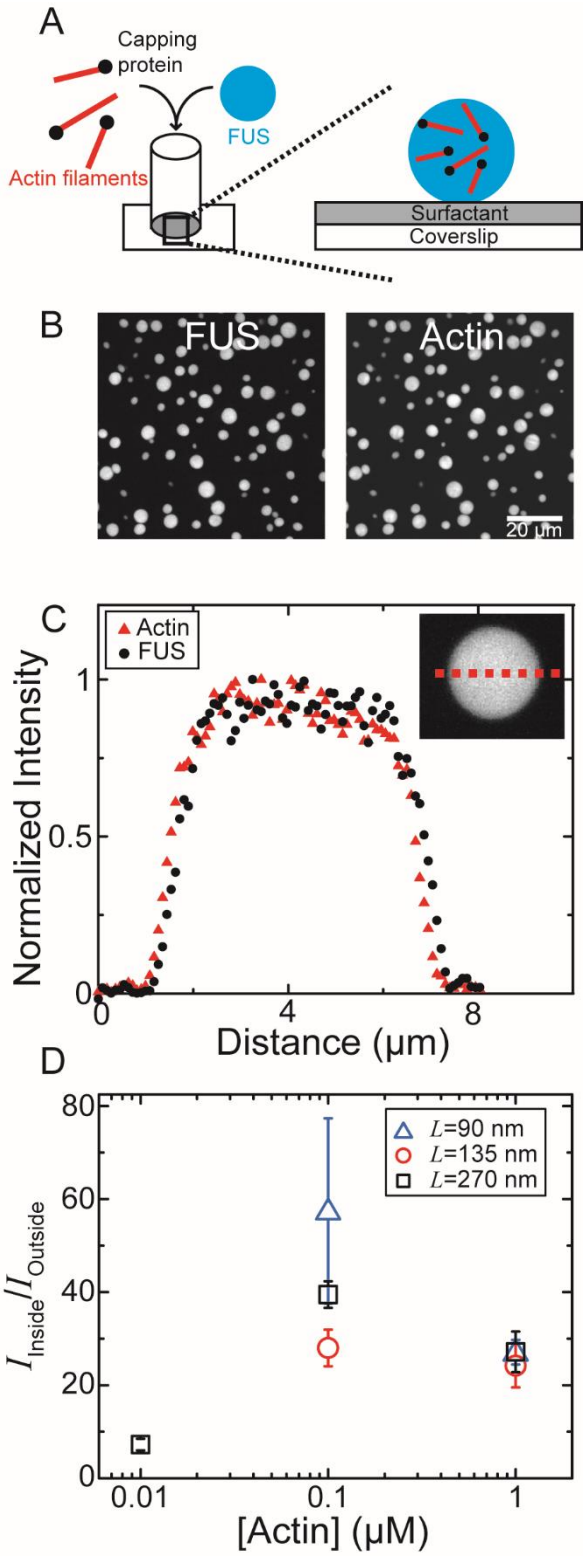

Figure 2.1: Actin and FUS form composite droplets. (A) Schematic of experimental setup. The protein FUS mixes with short, pre-polymerized actin filaments to form composite droplets which

Figure 2.1 continued: sediment to a surfactant passivated layer at the bottom of the sample chamber. (B) Images of composite droplets through fluorescence microscopy of FUS (left) and actin (right). Scale bar is 20 μm. (C) Intensity across the midplane of a droplet (*inset*, red dashed line) for FUS (black circles) and actin (red triangles). Intensities are normalized by their maximum values. Data shown in (B) and (C) for samples containing 1 μM actin with length $L \sim$ 90 nm. (D) Intensity of actin in droplets relative to in the solution as a function of actin concentration for samples with actin of length $L \sim$ 90 nm (blue triangles), $L \sim$ 135 nm (red circles), and $L \sim$ 270 nm (black squares). Error bars are standard deviation between droplets. In all panels, the data shown are droplet samples composed of 4.4 μM FUS.

concentrations (0.01 μM), the intensity of actin inside is about 7 times greater than in the bulk, indicating that the actin filaments preferentially accumulate into FUS droplets. At higher actin concentrations (0.1 μM -1 μM), the intensity is ~ 25-40 times greater in the droplets than the bulk solution (Figure 2.1D). These observations are consistent with previous measurements of actin partitioning into coacervates, where the intensity ratio was found to increase with increasing actin at low concentrations before plateauing at higher concentrations [136]. I note that without knowing the explicit relationship between intensity and concentration, the ratio $I_{\text{inside}} / I_{\text{outside}}$ does not provide an exact measure of a partition coefficient. However, the large value measured is indicative of large accumulation of actin within the droplets. Thus, actin filaments preferentially incorporate into the FUS droplets across a range of actin concentrations.

Similar to previous reports of FUS droplets [113], one growth mechanism of composite actin-FUS droplets is coalescence, where two initially separate droplets merge and relax into a new droplet (Figure 2.2A) Analyzing the dynamics of coalescence provides an estimate of the relative contributions of two droplet material properties: interfacial tension and viscosity. I measure the droplet cross-sectional area, A, as a function of time, t, during individual coalescence events (Figure 2.2B, *inset*). Two droplets with a total initial cross-sectional area at time of first contact, A_i, coalesce into a new droplet which relaxes to a final shape with cross-

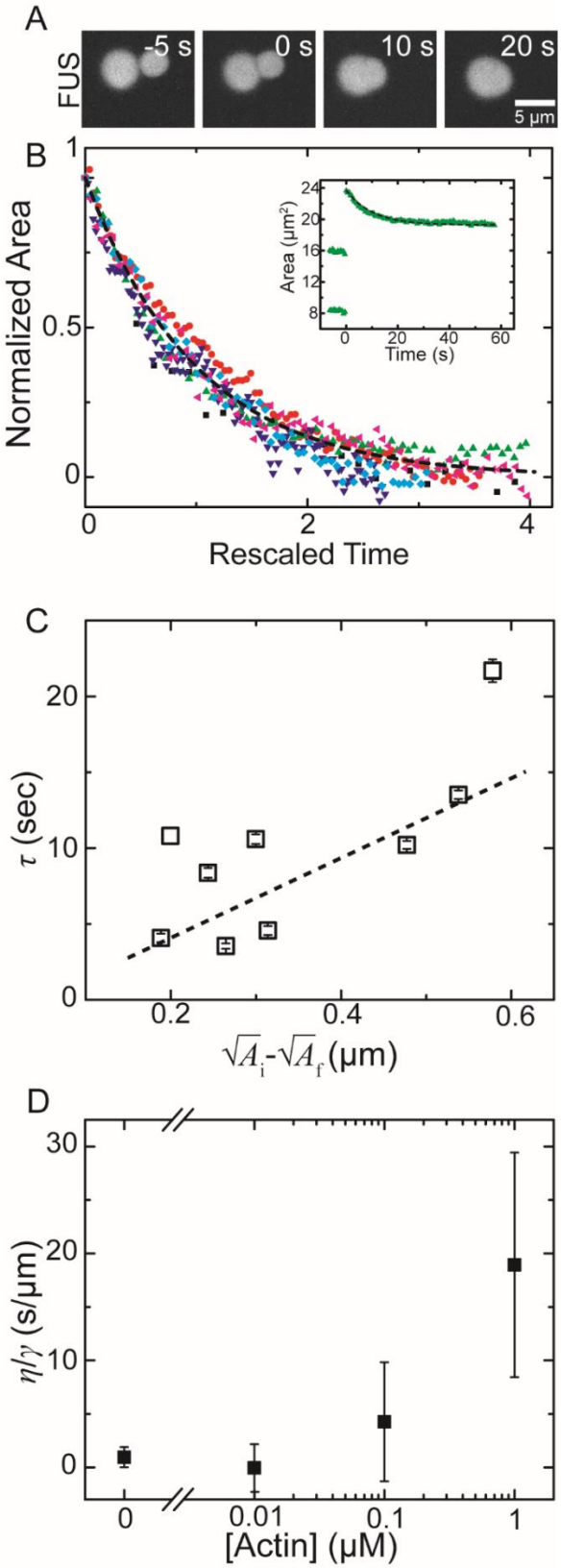

Figure 2.2: Droplets are liquid with actin dependent properties.

Figure 2.2 continued: Droplets are liquid with actin dependent properties. (A) Fluorescence microscopy images of (FUS-labeled) droplets coalescing over time. Scale bar is 5 μm. (B) *Inset:* Area over time for a single coalescence event (green triangles) is fit by a single exponential (black dashed line). Normalized area for 6 different droplet coalescence events with time rescaled by the timescale τ. Black dashed line indicates a single exponential, e^{-t}. Data shown is for droplets composed of 4.4 μM FUS and 1 μM actin with $L \sim 90$ nm. (C) Dependence of the characteristic coalescence time, τ, on the coalescence length scale, defined as the difference of the square roots of the final and initial areas. Dashed line indicates a linear fit to the data. Data shown are droplet samples composed of 4.4 μM FUS and 1 μM actin. (D) The ratio of the viscosity to surface tension as a function of actin concentration. Error bars are the standard error from the linear fit.

sectional area, A_f. The area decrease is consistent with an exponential decay, which I can extract a characteristic relaxation time, τ, from the fit $A(t) = A_f + (A_i - A_f)e^{-t/\tau}$. Plotting the normalized area, $(A - A_f)/(A_i - A_f)$, against rescaled time, t/τ, reveals that coalescence events from various droplet sizes collapse into a single curve that is consistent with an exponential decay (Figure 2.2B), indicative of coalescence associated with isotropic fluids [42].

For isotropic fluids, I expect the characteristic relaxation time, τ, to scale linearly with the coalescence relaxation length, the difference between the initial and final length, Δl, of the droplet. Here, to account for droplets with shapes that deviate from spherical, I define the relaxation length from the square root of the droplet cross-sectional area such that $\Delta l = \sqrt{A_i} - \sqrt{A_f}$. I find that τ increases with the difference between the coalescence relaxation length (Figure 2.2C). By balancing viscously dissipated mechanical energy against change in the interfacial energy of the coalesced droplet as it relaxes, I see that τ depends on the viscosity, η, and interfacial tension, γ, of the liquid as $\tau \sim \eta/\gamma \cdot \Delta l$ [42]. Thus, the slope of the linear fit in Figure 2.2C gives the ratio η/γ. In Figure 2.2D, I find η/γ increases with actin concentration, suggesting that actin filament density impacts composite droplet viscosity more than it affects surface tension.

2.4.2 F-Actin Elongates Droplets

In contrast to FUS droplets which are always spherical [113], composite droplets also adopt a variety of elongated shapes (Figure 2.3A). The shape of these droplets is dependent both on the droplet size and actin concentration (Figure 2.3B). While average droplet size increases with time as droplets coalesce, I note that the droplet shape at a given size is independent of the time after formation, suggesting rapid actin accumulation in the droplets. Despite this observation, to reduce measurement uncertainty, I investigate the dependence of droplet shape in a population of droplets at a given time after formation. For low actin concentrations (<0.1 μM), droplets of all assayed cross-sectional areas (between 1 μm^2 and 32 μm^2) are spherical. However, for actin concentrations greater than 0.1 μM, I observe non-spherical droplets, particularly in smaller (below ~15 μm^2) droplets. For 1 μM actin, elongated shapes are observed for droplet sizes smaller than ~20 μm^2; as the droplet size increases, the average aspect ratio approaches 1 (Figure 2.3C). To quantitatively compare the size and actin concentration dependence of droplet shape, I plot average aspect ratio for small (4-6 μm^2), medium (14-16 μm^2) and large (>20 μm^2) droplets. I find the average aspect ratio decreases as droplet size increases, with the trend most pronounced at the highest actin concentration (1 μM). Furthermore, the average aspect ratio increases with actin concentration (Figure 2.3D). In contrast to the elongated droplets observed at higher concentrations, for the lowest actin concentration (0.01 μM), droplets of all sizes have an aspect ratio ~1. This strongly suggests that the high density of filaments within the droplets underlie the observed differences in aspect ratio.

I therefore hypothesize that the actin filaments elongate droplet shape through nematic ordering. The resulting nematic elasticity of aligned filaments competes with the droplet

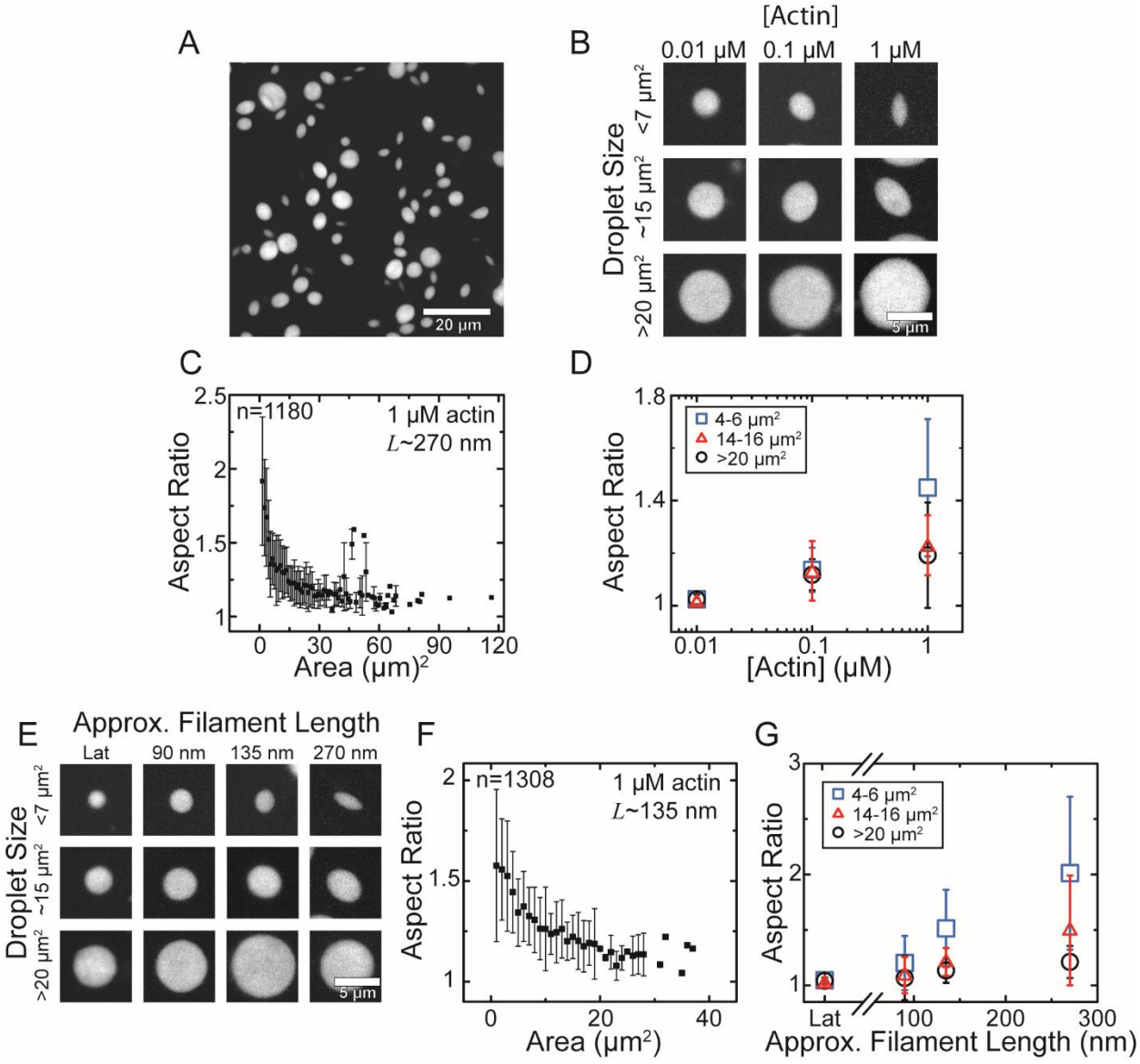

Figure 2.3: Actin filaments elongate droplets. (A) Fluorescence microscopy image of FUS-labeled droplet samples containing 1 μM actin with L ~ 270 nm. Scale bar is 20 μm. (B-D) Higher actin concentration elongates droplets. All data shown for droplets containing filaments with L ~ 270 nm. (B) Fluorescence images of composite droplets as a function of droplet size and actin concentration. Scale bar is 5 μm. (C) The average aspect ratio of the droplets as a function of cross-sectional area. (D) Actin concentration dependence of average aspect ratio for droplets with areas of 4–6 μm^2 (blue squares), 14–16 μm^2 (red triangles), and > 20 μm^2 (black circles). (E-G) Longer actin filaments elongate droplets. All data shown for droplets with 1 μM actin. (E) Fluorescence microscope images of FUS-labeled droplets as a function of droplet size and actin filament length. In the presence of latrunculin (Lat) which prevents actin polymerization, droplets are spherical regardless of size. Scale bar is 5 μm. (F) Aspect ratio as a function of cross-sectional area for droplets containing actin with L ~ 135 nm. (G) Average

Figure 2.3 continued: aspect ratio as a function of actin filament length. Symbols are the same as in part (D). Error bars represent ± 1 standard deviation between droplets.

interfacial tension, which constrains pure FUS droplets to be spherical. To test whether the filamentous form of actin, rather than the mere actin monomer incorporation, is causing the droplet elongation, I form composite droplets in the presence of the drug latrunculin (Lat) which prevents actin polymerization into filaments. In this case, all droplets are spherical (Figure 2.3E). Additionally, previous work has shown that nematic elastic energy scales with the aspect ratio of the rod-like constituents [77,81]. I thus hypothesize that filament length impacts droplet shape. To systematically study the impact of filament length on droplet shape, I modify the actin filament length through the amount of capping protein [137]. As the concentration of capping protein is increased from 1 mol% to 3 mol%, the average length of the actin filaments is expected to decrease from ~270 nm to ~90 nm. I find that, at 1 μM actin, droplet shape varies with average actin filament length, L, with longer filaments leading to more elongated droplets (Figure 2.3E). For L ~ 135 nm, smaller (<20 μm^2) droplets are elongated, with the average aspect ratio decreasing with cross-sectional area (Figure 2.3F). In contrast, for the shortest actin filaments tested, L ~ 90 nm, droplets of all sizes have aspect ratios ~1 (Figure 2.3E,G). Notably, for the smallest droplet sizes (4-6 μm^2), the average aspect ratio increases as the filament length increases.

2.4.3 Droplets are Tactoids, Ellipsoids, or Spheres

For a given droplet size and composition, there is a distribution of three characteristic shapes: elongated tactoids with pointed ends, ellipsoids, and spheres. The two elongated shapes, tactoids and ellipsoids, are distinguished by the local shape at the tips of the long axis, where tactoids tips are sharp cusps while ellipsoids tips are smooth (Figure 2.4A). To quantify the prevalence of

these shapes, I measure the fraction of droplets that are tactoids as a function of cross-sectional area. I visually distinguish between tactoids and ellipsoids or spheres based on the droplet tips, noting that even droplets with ellipsoid shape are technically tactoids if they are nematic liquid crystal droplets. With 1 μM actin, L ~ 270 nm, droplets with cross-sectional areas less than 8

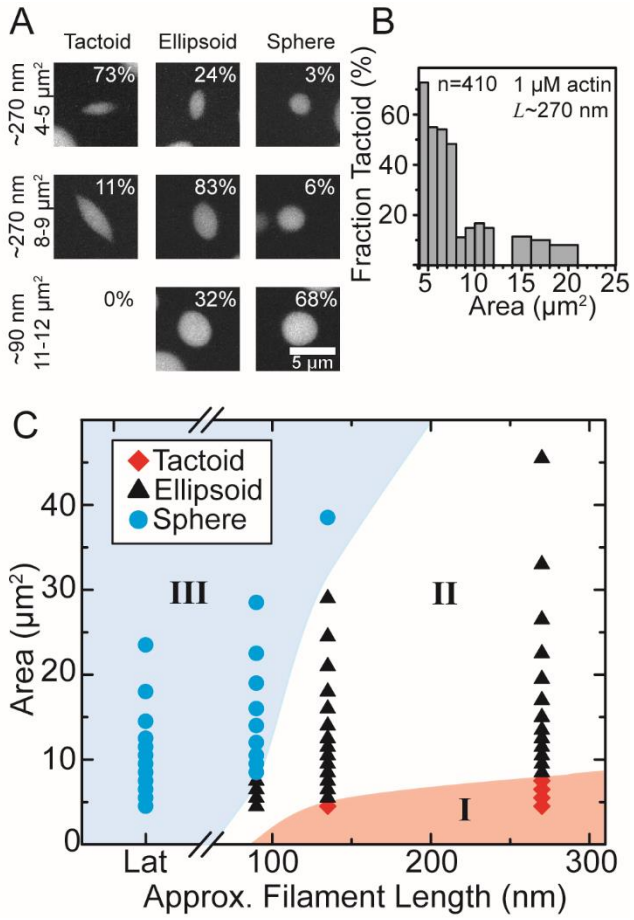

Figure 2.4: Droplet size and actin length tune the shape of the droplets. (A) Occurrence of droplet shape for three different droplet lengths and cross-sectional areas. Droplets primarily take on one of three shapes: tactoids with pointed tips (left column), ellipsoids that are elongated but have round tips (center), or spheres (right). (B) Fraction of the droplets that are tactoids as a function of cross-sectional area for droplets containing actin with L ~ 270 nm. Above 25 μm^2, none of the observed droplets are tactoids. The shape of droplets under 4 μm^2 could not be accurately determined. Bar width corresponds to the range of areas included and varies such that each bar represents at least 10 droplets. (C) Phase space of droplet shape as a function of size and filament length, where latrunculin (Lat) indicates unpolymerized actin. I define three regions based on whether droplets are majority (>50%) tactoids (I, red diamonds), ellipsoids (II, black triangles), or spheres (III, blue circles). All samples contain 1 μM actin and 4.4 μM FUS.

μm^2 are primarily (>50%) tactoids (Figure 2.4B). On the other hand, for larger (>8 μm^2) droplets, the fraction that are tactoids sharply decreases to less than 20%. While the transition from tactoid to ellipsoid and sphere with increasing droplet size has been theoretically predicted [87,124], to my knowledge it has not been previously experimentally observed. Based on this observation I classify droplets by the shape which is most frequently adopted for each size and filament length. I define any droplet with aspect ratio <1.1 to be a sphere. While in principle this definition is not mutually exclusive with being a tactoid, I do not observe tactoids with aspect ratios this small. Plotting as a function of filament length and droplet size, I find three regions of phase space (Figure 2.4C) based on whether the droplets are primarily (>50%) tactoids (I), ellipsoids (II), or spheres (III). The smallest droplets with longest actin filaments primarily form tactoids (Figure 2.4C, *Region* I). Larger droplets are primarily elliptical, while the largest are spheres (Figure 2.4C, *Regions* II & III). The critical size at which droplet shape transitions to ellipsoids or spheres increases with longer filaments: for $L \sim 90$ nm, all but the smallest (>8 μm^2) sizes are primarily spheres and no droplets are majority tactoids, even at the smallest droplets measured (4 μm^2), while for $L \sim 270$ nm, droplets are primarily ellipsoidal from 8 μm^2 up to the largest size observed (~45 μm^2). Droplets containing purely monomeric actin are spherical at all sizes (Figure 2.4C, *Region* III, *Lat*). Thus, the shape of composite droplets can be tuned either by changing the concentration or length of actin filaments.

2.4.4 Quasi Bipolar Tactoid Model Describes the Droplets

At high densities (1 μM) of actin, elongated spindle shaped droplets are seen to nucleate and become more spheroidal as they grow (Figure 2.3A). This decrease in aspect ratio with increasing droplet size is consistent with the bipolar model of tactoids where the comprising

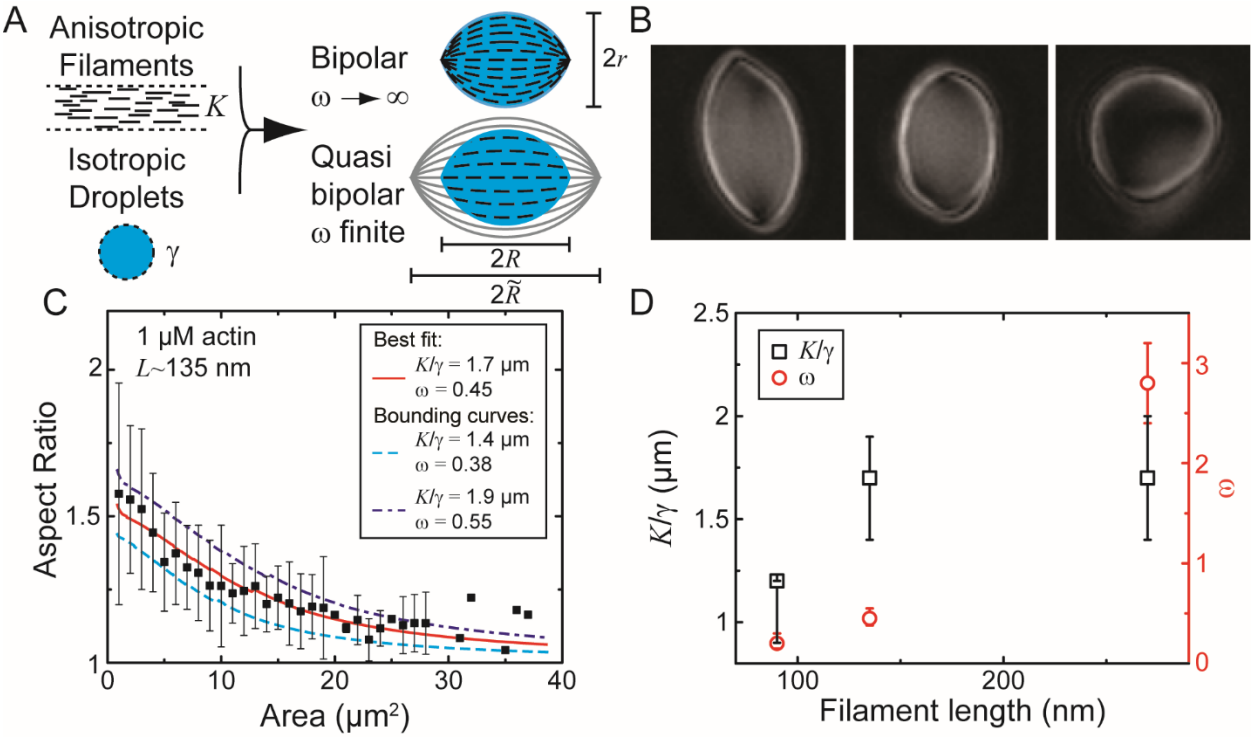

Figure 2.5: Bipolar model description of droplet shape. (A) Cartoon schematic of droplet shape determinants. Actin filaments contribute a nematic elastic energy, while FUS droplets predominately contribute an isotropic interfacial energy. Bipolar tactoids have defects at the poles, whereas in quasi bipolar tactoids, virtual defects exist outside the droplet. (B) LC polscope birefringence images of composite droplets. The dark areas at the poles indicate defects lacking local nematic ordering. (C) Theoretical fit (lines) to experimental data (black squares). K/γ and ω are extracted from the best fit (red solid line), while the fits that bound the experimental data give the minimum (light blue dashed line) and maximum (dark blue dashed line) values. Data are from samples containing actin with $L \sim 135$ nm. (D) K/γ (black squared) and ω (red circles) as a function of actin filament length. Error bars are from the maximum and minimum theoretical fits as shown in part (C). All data are from samples containing 1 μM actin.

rods (here, actin filaments) align parallel to the droplet interface giving rise to curved director lines that meet at point defects known as "boojums" [87]. While these defects are located right at the droplet poles in the ideal bipolar configuration, they can be located off the droplet surface in the more realistic quasi bipolar configuration (Figure 2.5A) [134,135]. This latter model also successfully describes the continuous transformation of the director geometry from homogeneous, with uniform director lines, to bipolar with increasing droplet size previously

observed [83,90]. The internal nematic order and its bipolar director orientation for 1 μM actin-FUS droplets is confirmed by observing the droplets under crossed polarizers where intensity corresponds to local nematic order (Figure 2.5B). In particular, the reduced intensity seen at the droplet poles suggest the presence of defects in the nematic order that are characteristic of bipolar tactoids [90]. However, the resolution of these polarization images is not sufficient to distinguish between a quasi bipolar and a perfectly bipolar director structure.

The shape and director structure of a nematic tactoid is determined by a balance of its interfacial energy and its bulk nematic elastic energy that depends on the Frank elastic constant, K [90]. The interfacial energy comprises the surface tension, γ, of the droplet, as well as the surface anchoring energy cost of the deviation of the director from parallel alignment with the droplet interface (Figure 2.5A). This is expressed by a dimensionless parameter, $\omega = \gamma_A/\gamma$, which is the strength of the surface anchoring energy arising from nematic alignment, γ_A, relative to the fluid surface tension. For a tactoid of characteristic length R, the interfacial energy grows as R^2 with droplet size, whereas the bulk nematic elastic energy scales as R (elastic energy scales as droplet volume times the square of the curvature of the director lines, $R^3 \cdot R^{-2} \sim R$). For bipolar droplets of increasing size, the interfacial energy grows larger relative to the bulk elastic energy, resulting in lower aspect ratios that become nearly spherical when the droplet size is large compared to a characteristic nematic distortion length scale, $R \gg K/\gamma$. This behavior is seen for 1 μM actin-FUS tactoids (Figure 2.4C). For smaller droplets with $R \ll K/\gamma$, the nematic elastic energy cost of distorting the directors into the bipolar configuration becomes prohibitively expensive resulting in a nearly uniform director structure throughout the droplet. In this homogeneous limit, the aspect ratio of the droplet is determined by the anchoring strength, ω

[87]. While continuous transformation of the director structure from homogeneous to bipolar with increasing droplet size was previously reported [83,90], this transition may occur at droplet sizes below experimental resolution. The quasi bipolar model captures the droplet shape trends realistically in both these limiting cases and unlike the pure bipolar geometry, it captures the low aspect ratio shapes at small droplet sizes seen in these composite droplets.

Using the quasi bipolar geometry, I numerically minimize the scaled form of the free energy expression to yield expected aspect ratios for a given droplet size, measured as average cross-sectional area in the experiment. In this quasi bipolar model, I expect that the aspect ratio for a given droplet size depends only on two unknown constants: the distortion length scale, K/γ, and the anchoring strength, ω. Comparing the experimental data to the model then let me estimate average values for both these material properties for the FUS-actin droplets (Figure 2.5c, Figure 2.6). I expect both K/γ and ω to increase with actin concentration as well as average actin filament length, since these parameters drive greater entropic alignment of the actin. This is consistent with previous experiments in actin nematics that show K scaling with filament length [77,81]. Such trends may also occur in FUS-actin droplets, but it is not clear given the resolution of my measurements of K/γ (Figure 2.5D). The uncertainty in measuring K/γ results from the large dispersion in the observed droplet aspect ratios. Additionally, I estimate the length scale, K/γ, of FUS-actin droplets to be a few microns, similar to estimates from pure actin tactoids [42], whereas $\omega = \gamma_A/\gamma$ for FUS-actin composite droplets is significantly lower than for pure actin tactoids. This decrease is consistent with the expectation that the presence of FUS increases the interfacial tension but not surface anchoring.

For low densities (0.01 μM) of actin, the resulting droplets are spherical for all sizes, as is expected of pure FUS droplets. This points to the absence of a nematic phase at such low actin

concentration. The Onsager theory does in fact predict a critical density of rods above which they align purely on entropic grounds [79,123]. The critical volume fraction at which nematic order occurs scales inversely as the aspect ratio of the filaments, L/D, where $D \sim 8$ nm is the diameter of the constituent actin filaments. This qualitatively explains the observed tendency to form elongated droplets at higher actin concentration as well as at longer average actin filament length. At intermediate densities (0.1 μM), the droplets are slightly elongated and appear ellipsoidal, but their aspect ratio does not depend appreciably on droplet size. They also lack the characteristic pointed ends of a bipolar tactoid. I speculate that this concentration of actin induces some nematic order resulting in a slight anisotropy of the physical properties of the droplet. This results in an ellipsoidal instead of a spherical droplet, while not contributing sufficient nematic order required for the characteristic tactoid shape.

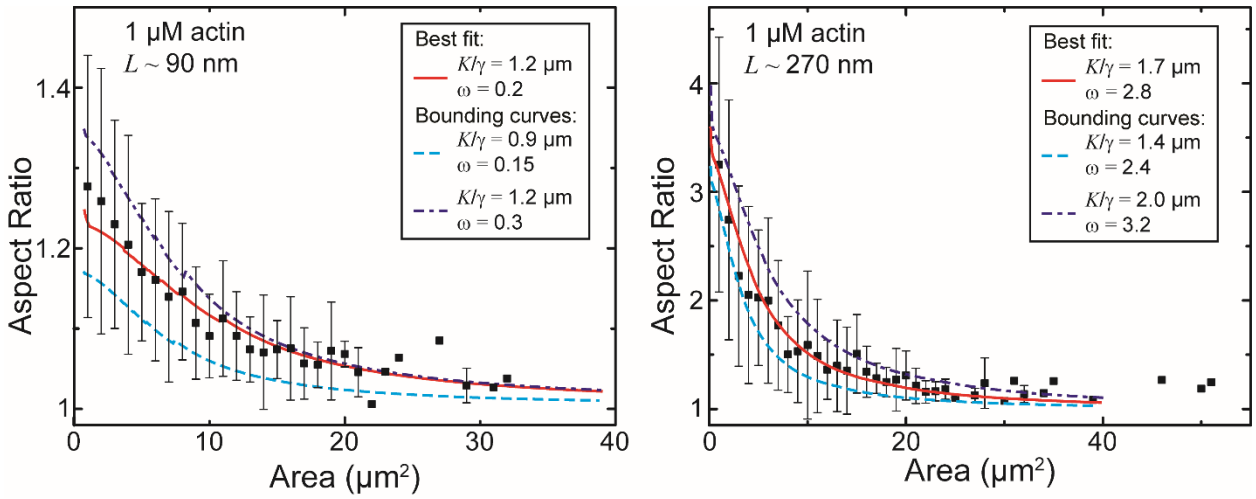

Figure 2.6: Quasi bipolar model fits. Theoretical fit (lines) to experimental data (black squares). K/γ and ω are extracted from the best fit (red solid line), while the fits that bound the experimental data give the minimum (light blue dashed line) and maximum (dark blue dashed line) values. Data are from samples containing actin with $L \sim 90$ nm (*left*) and $L \sim 270$ nm (*right*).

2.5 Conclusions

Here I find that actin filaments spontaneously partition into FUS droplets. Since FUS and actin have no known specific biochemical interaction, this suggests the complexation is driven by non-specific protein-protein interactions such as charge or hydrophobicity. Partitioning of filaments induces anisotropy in otherwise isotropic condensates. While it is well appreciated that modifying macromolecular components and their interactions can influence mechanical properties from solid-like to liquid-like in droplets [121], here I tune the droplet anisotropy while maintaining a liquid phase. Moreover, the partitioning of actin filaments into a significantly reduced volume provides a new route for forming liquid crystal droplets. This complements a growing range of methods to form composite macromolecular droplets, such as previous reported protein partitioning into coacervates due to specific binding interactions [118] or charge interactions [138–140]. Exciting areas of future inquiry may seek to elucidate how the macromolecular component interactions control miscibility and spatial organization of components and mechanics of composite liquid droplets.

One consequence of the droplet's liquid crystallinity is that competing effects of elasticity with interfacial tension give rise to diverse droplet shapes and internal structure. For example, I have shown experimentally the transition between spherical and tactoid-shaped droplets which has been previously theoretically predicted [87]. This shape change inherently causes changes in the surface area to volume ratio, which could be harnessed as a mechanism to dynamically tune partitioning or other interface-mediated activity. Furthermore, these shapes reflect changes in the spatial organization of the filaments across the droplet [124]. This internal structure could be used as a template for droplet-scale spatial structure [141–144]. Thus, composite condensates

offer a promising means to understand and design reconfigurable materials where the interfacial and elastic phases can be orthogonally tuned.

Additionally, phase separation is well appreciated as a mechanism of intracellular organization [145]. I speculate that the myriad of biopolymers found within the cytoplasm may spontaneously partition into cytoplasmic condensates to form similar composite droplets in vivo. One outstanding example speculated to form a liquid crystalline phase is that of the mitotic spindle [127]. Recently, evidence for a "spindle matrix" comprised of protein-rich condensate around microtubule filaments [146] suggests an analog of the composite I observe. Finally, the extent to which this may influence intermediate filament and actin filament organization is unknown, but has potential implications for neurodegenerative diseases [147] and control of cytoskeletal signaling [148].

CHAPTER 3

ACTIN FILAMENT ALIGNMENT CAUSES MECHANICAL HYSTERESIS

3.1 Preface

This chapter is adapted from Scheff *et al.* 2021 [149]. All experiments were performed by the author. All simulations were performed by Steven Redford, while Chatipat Lorpaiboon assisted in the development of the methods required to simulate constant stress training. Sayantan Majumdar provided guidance conducting experiments and analyzing the resulting data. Margaret Gardel and Aaron Dinner provided invaluable input throughout.

3.2 Introduction

The mechanical properties of eukaryotic cells are, to a large degree, determined by the actin cytoskeleton [1]. To allow for cell shape change and cytoskeletal remodeling, actin networks in vivo rapidly adjust their structure and mechanics. Stress-mediated adaptation can arise from mechanotransduction pathways that dynamically regulate actin cytoskeletal composition [150]. Alternatively, the dynamic nature of cross-linking proteins can also result in adaptation in passive networks [73,74,151].

The structure and rheological properties of actin networks are controlled by varying the concentration and type of protein cross-linkers [52,152,153]. At a sufficiently high cross-link density, the network's elastic modulus increases nonlinearly at large strains, a phenomenon known as strain stiffening. Strain stiffening is a reversible phenomenon, arising from the nonlinear increase in the spring constant of individual semi-flexible polymers as they are

stretched [72]. While filament stretching dominates the mechanics of strain stiffening, filaments can also buckle under shear, creating a locally weakened region [75,154]. Changes in cross-linker concentration or filament orientation can influence the relative likelihood of shear-induced bending and stretching, impacting the mechanical response [53,67,75,155]. The physical properties of cross-linkers, such as their length and flexibility, also influences network structure and mechanics [156].

Majumdar *et al*. recently showed that actin networks cross-linked with the protein filamin exhibit mechanical hysteresis [74]. In contrast to strain stiffening, mechanical hysteresis is a stress-induced and direction-dependent modification to elastic properties that is maintained long after the applied stress is removed but can then be modified by subsequent stress applications. These networks have an asymmetric response to strain, where higher stress is required to shear the network in the direction of the previously applied stress than in the reverse direction. Simulations suggest the asymmetric response results from shear induced filament alignment [73,74]. These simulations, however, did not investigate how filaments realign under stress or how the nature of the cross-linking protein might affect this reorganization. While the mechanics and affinity of the cross-linking proteins are known to play an important role in rheology, their effect on mechanical hysteresis and the adaptive properties of actin networks is unknown**.**

Here, I explore how cross-linker properties and concentration can be used to modify the extent of mechanical hysteresis. Furthermore, simulations allow me to directly probe the internal structure of networks and how changes correlate with hysteresis. I find that hysteresis requires networks to have a nonlinear response to strain and correlates strongly with the ability of filaments to align under stress.

3.3 Materials and Methods

3.3.1 Protein Purification

Proteins are purified as described in Appendix A.2.

3.3.2 Network Preparation

To prepare *in vitro* networks, 23.8 μM of G-actin and a varied concentration of cross-linker are added to CaBG (Appendix A.1.). Polymerization is initiated by adding 1/10 the final volume of 10x KMEI and mixing immediately before placement on the rheometer sample chamber. After loading the sample, the value of G' and $G"$ with time is measured at a frequency of 0.5 Hz and a strain of 0.05 to track network polymerization, characterized by an increase in both moduli. Each network is polymerized for 1.5 hrs, at which point both G' and $G"$ are constant with time. Cross-linker concentration is reported as a ratio $R_{Cross-linker} = [cross-linker]/[actin]$.

3.3.3 Bulk Rheology

All rheological measurements are performed on an Anton-Paar MCR301 rheometer at 22° C using a 25 or 50 mm diameter plate and a 160 mm gap. A humidity chamber is used to prevent solvent evaporation. Each readout is performed 3 consecutive times. For analysis, the second time is used to avoid the impact of the initial acceleration. To find γ_{max}, I perform the readout process to incrementally increasing γ on an untrained network. γ_{max} is then the highest value of γ for which the network does not irreversibly weaken during repeated readout cycles. This process is repeated at different cross-linker concentrations and the lowest value is used. γ_{Max} is measured separately for each cross-linker. During training, the networks undergo plastic deformation and no longer relax back to $\gamma = 0$ under zero stress, but instead maintain a residual strain γ_R. For subsequent readouts, I redefine zero strain such that $\gamma_R = 0$.

3.3.4 Simulations

Networks were simulated using the package AFINES, which has been previously described in [157] and is summarized here. AFINES takes advantage of a coarse-grained description of cytoskeletal components in two dimensions to efficiently simulate their networks. Specifically, actin filaments are parametrized as N+1 beads connected by N springs of length 1 μm; an additional N–1 springs are applied to the angles at the joints to limit bending and afford simulated filaments a persistence length similar to that measured experimentally. Cross-linkers are similarly modeled as springs of length l and stiffness f with beads on either end that can bind and unbind from filaments via a kinetic Monte Carlo scheme that preserves detailed balance. The motion of filaments and cross-linkers evolves according to an overdamped Langevin dynamics in two dimensions with a timestep Δt of 10^{-6} s and Lees-Edwards boundary conditions [158].

To assess the rheological properties of simulated networks training and readout shears are performed analogously to the experiment. For what follows, I define $\gamma = \Delta X/Y$ as the unitless engineering strain, where Y is the box height and ΔX is the maximum horizontal displacement since the initiation of shear. Every $\Delta t_s = 10^{-5}$ s, a shear strain is applied to bead i using

$$\Delta x_i(t) = \frac{d\gamma(t)}{dt} y_i(t) \Delta t_s \tag{3.1}$$

where x_i and y_i are the coordinates of bead i. Shear strain is measured as $(1/A)\ dU/d\gamma$ where A is the area of the simulation box and U is the total potential energy.

To initialize the simulations, the position of the first bead of each filament or crosslinker is drawn with uniform probability within the box and introduce the remaining beads in a manner consistent with the Boltzmann distribution such as to randomly orient the crosslinker or filament.

For the training, the network is equilibrated for 5 s and then compute γ/dt at every tenth step (i.e., $\Delta t_s = 10^{-5}$ s) such as to achieve a constant shear stress σ using the Berendsen barostat [159]:

$$\frac{d\gamma(t)}{dt} = k_\sigma \left(\sigma - \frac{1}{A}\frac{dU}{d\gamma}\right), \tag{3.2}$$

where k_σ is the strength of the coupling; I substitute the resulting $d\gamma/dt$ into Equation 3.1, which is executed prior to the Langevin integration. As in the experiment, networks are trained to the stress that an untrained network achieves at $\gamma = 0.5$. Simulations are trained by applying the stress σ with $k_\sigma = 0.2$μm/(pN s) for 10 s before allowing them to relax by approaching $\sigma = 0$ with $k_\sigma = 0.01$ μm/(pN s) for an additional 10 s before readout is performed.

For readout simulations, the system is equilibrated for 5 s before applying a triangle wave of the form

$$\gamma(t) = 4\gamma_{max} v \left(t - \frac{1}{2v}\left\lfloor 2vt + \frac{1}{2}\right\rfloor\right)(-1)^{\left\lfloor 2vt + \frac{1}{2}\right\rfloor} \tag{3.3}$$

where γ_{max} is the amplitude of the wave and v is the frequency of the oscillation. For all of the simulations considered herein $\gamma_{max} = 1$ and $v = 0.5$ s^{-1}. Stress is measured over a number of shear cycles to ensure that the simulation is stable over time. Specifically, readout shear is applied for 11 seconds such that untrained simulations have a final time, t_{final}, of 16 s.

3.4 Results and Discussion

3.4.1 Networks' Response to Training Stress

To investigate its origin and controlling factors, I probe mechanical hysteresis in actin networks formed with cross-linkers with various physical properties and concentrations. As such, I require a standardized method of imparting and measuring hysteresis that can be applied uniformly to all cross-linker conditions. I adapt the process developed by Majumdar *et al.*, in

which the network's directional response to shear is measured before and after a training stress [74]. Specifically, I train the networks by subjecting them to a constant stress, σ, for 300 s, before allowing them to relax at $\sigma = 0$ for an additional 100 s (Figure 3.1A). Here, training always occurs in the same direction, corresponding to clockwise rotational shear and defined as positive strain, whereas counterclockwise rotation is defined as negative strain. I measure the effect of training using a readout process, in which the network is cyclically sheared with an amplitude of γ_{max} (Figure 3.1B). Comparing readout curves taken before and after training allows me to ascertain the effect that training has on the rheological properties of cross-linked networks and reveals any asymmetric responses arising from the direction of the training stress. Since networks irreversibly break at sufficiently large strains, I set γ_{max} to be the maximum strain at which the network can be repeatably sheared with no observed changes in its stress response, as described in methods. γ_{max} was determined separately for each cross-linker used. The training stress for each network is individually determined as the stress required to shear the untrained network to $\gamma = \gamma_{max}/2$. I note that Majumdar *et al*. found that training for longer times or under higher stress had an increased impact on the network [74]. However, I found that training for longer times of 500 s did not further increase the network's response to training, while higher training stress irreversibly broke the network.

First, I measure the effect of training on networks cross-linked with α-actinin, a rigid protein able to form transient bonds between filaments, and whose rheological properties are well studied [160]. I characterize the readout response through both the stress and the differential modulus $K = d\sigma/d\gamma$ as a function of the strain, γ. K can be understood as a strain-dependent elastic modulus, and any increase reflects a nonlinear, strain stiffening response. Initially, both σ

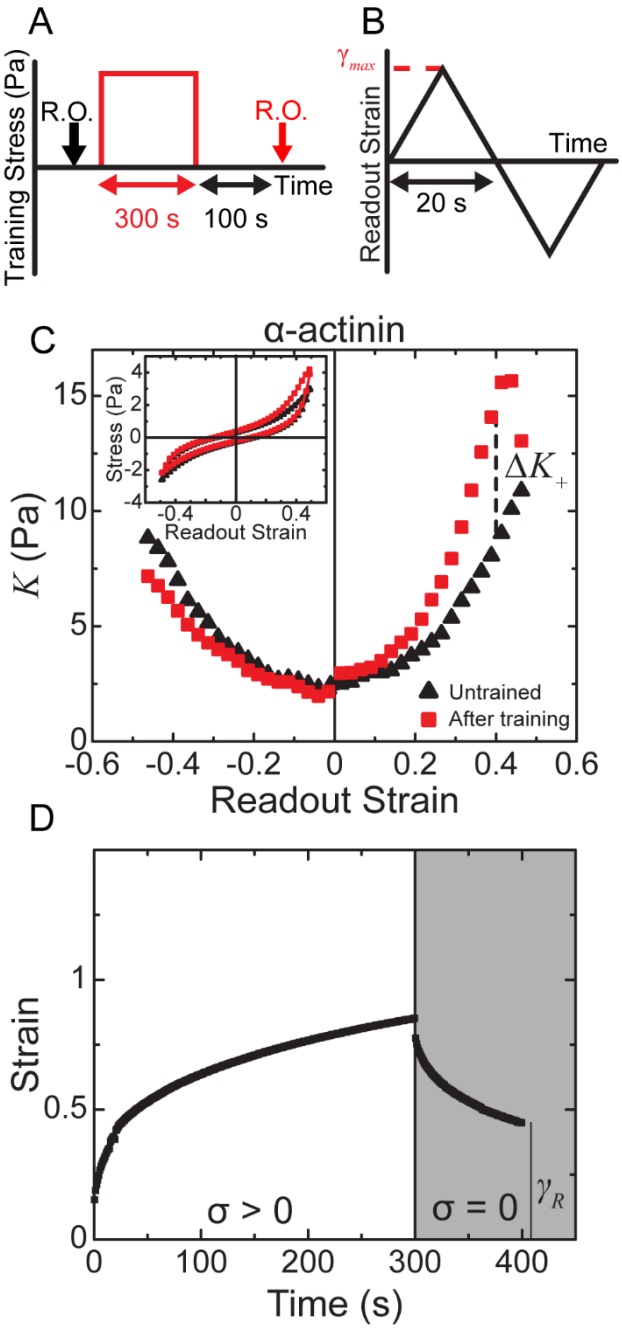

Figure 3.1: Cross-linked actin networks have asymmetric response to strain after a training stress. (A) Cross-linked actin networks are trained by applying a constant stress for 300 s before being allowed to relax at zero stress for an additional 100 s. Before and after training, the nonlinear response to strain is measured using a readout process (B), in which the network is sheared in both the direction of training and the opposite direction. (C) The differential modulus K, measured at different strains during readout, before (black triangles) and after (red squares) training. ΔK_+ measures the rescaled difference in the trained versus untrained value of K. Inset: The corresponding stress from which K was measured. Data shown for a network with $R_\alpha = 1\%$

Figure 3.1 continued: (D) Example creep response of the strain to a training stress (white region). After training (gray region), the network does not relax to its original position, leaving a residual strain γ_R.

and K are symmetric across $\gamma = 0$, as expected for an isotropic material (Figure 3.1C, black triangles) [74]. I call this initial case the "untrained" network. In contrast, the networks develop an asymmetric response to shear direction after training. After training, K increases for $\gamma > 0$ and decreases for $\gamma < 0$ relative to the untrained case (Figure 3.1C, red squares). Training thus induces a direction dependent mechanical response. I refer to this phenomenon as mechanical hysteresis and quantify it by the parameter

$$\Delta K_+ = \frac{K_{Trained} - K_{Untrained}}{K_{Untrained}} \tag{3.4}$$

where $K_{Untrained}$ and $K_{Trained}$ are the differential moduli measured at $\gamma = 0.8 * \gamma_{max}$ before and after training, respectively. ΔK_+ corresponds to the fractional increase in differential modulus for $\gamma > 0$. I measure ΔK_+ at $0.8 * \gamma_{max}$ since this strain is close to γ_{max} and well within the regime of nonlinear shear response while avoiding artifacts near γ_{max} due to inertial effects as the plate reverses direction. Furthermore, the network does not relax back to its original state after training. Instead, it undergoes a plastic deformation and maintains a residual strain, γ_R (Figure 3.1D). In previous work, I found that increased γ_R corresponds to larger amounts of hysteresis [74]. This correlation hints at underlying changes in the network during training that could explain the observed phenomenon. Additionally, both here and in previous work, hysteresis is reversable with subsequent training in the negative direction producing an opposite hysteretic response [74]. I therefore conclude that the causes behind hysteresis must be similarly reversible. However, while these observations describe the bulk phenomena of mechanical hysteresis, they do not provide any microscopic origin.

To grasp the microscopic effect that training has on cross-linked networks I turn to coarse-grained simulations using the simulation package AFINES [157]. Past modeling efforts initialized simulations in putative post-training geometries to evaluate plausible mechanisms of mechanical hysteresis, namely that the effect can be explained by post-training nematic alignment of filaments [74]. However, here I endeavor to explicitly simulate the training process to gain a more complete understanding of shear-induced rearrangements. The model and simulations are described in Methods. In brief, I represent networks in two dimensions by bead-spring filaments that are connected by cross-linkers with length l and stiffness f that can bind and unbind filaments with rates k_{on} and k_{off} (Figure 3.2A). These simulations specifically contain 500 7-μm filaments initialized randomly in a 20 x 20 μm box with periodic boundary conditions. Training and readout follow protocols analogous to the experiments as described in Methods.

I observe a mechanical hysteresis response similar to that seen in experiment with a cross-linker density of 9 μm^{-2}, $l = 0.15$ μm, $f = 100$ pN/μm, $k_{off} = 0.5$ s^{-1}, and a $k_{on}/k_{off} = 10$ (Figure 3.2B). Specifically, the trained networks in simulation stiffen in the direction of training and soften in the opposite direction. Having successfully recapitulated mechanical hysteresis with a heretofore uninvestigated cross-linker and a simulation that explicitly models training I now turn to investigate the origins of the phenomenon.

3.4.2 Measuring Filament Alignment

Majumdar and colleagues' past investigation of mechanical hysteresis in similar networks suggested that the ability of the network to rearrange in response to training is the origin of the mechanical hysteresis response. To investigate whether such rearrangements occur in these simulations, I measure the nematic order parameter

$$S = 2\left(\langle cos(\theta_{ij})\rangle - \frac{1}{2}\right)$$

where θ_{ij} is the angle between two filament sections. For the simulated network in Figure 3.2B, after equilibration but before the onset of training, the network is largely isotropic with S =0.004 (Figure 3.2C). In contrast, the filaments in the trained network before readout are aligned with S =0.09, over an order of magnitude increase. These results indicate that networks do indeed rearrange in response to the training stress.

I test the importance of these network structural changes in developing hysteresis by altering the unbinding rate of cross-linkers in simulations. If alignment of filaments is indeed how mechanical hysteresis develops, then cross-linkers with lower unbinding rates will lead to less structural rearrangement and lower values of ΔK_+. To test this hypothesis, I first simulate a network with a crosslinker density, R_{Sim}, of 9 μm^{-2} and an extremely slow off rate of $k_{off} = 0.05\ s^{-1}$ and $k_{on}\ /k_{off} = 100$ (Figure 3.2D). In this low rearrangement regime, I find that the network does not exhibit the mechanical hysteresis response following training. Furthermore, when I allow k_{off} to vary from 0.05 s^{-1} to 3 s^{-1} while keeping the ratio of $k_{on}\ /k_{off} = 10$, I find that decreasing off rate leads to reduced ΔK_+ (Figure 3.2D). As k_{off} drops below 0.25 s^{-1} the network does not respond to training at all. Furthermore, these changes in ΔK_+ correspond to changes in alignment, which similarly increases with k_{off}, confirming that the transient nature of cross-linkers is essential for filament rearrangements. Changes in network structure during training are thus vital for mechanical hysteresis, and sufficiently reducing these rearrangements eliminates hysteresis.

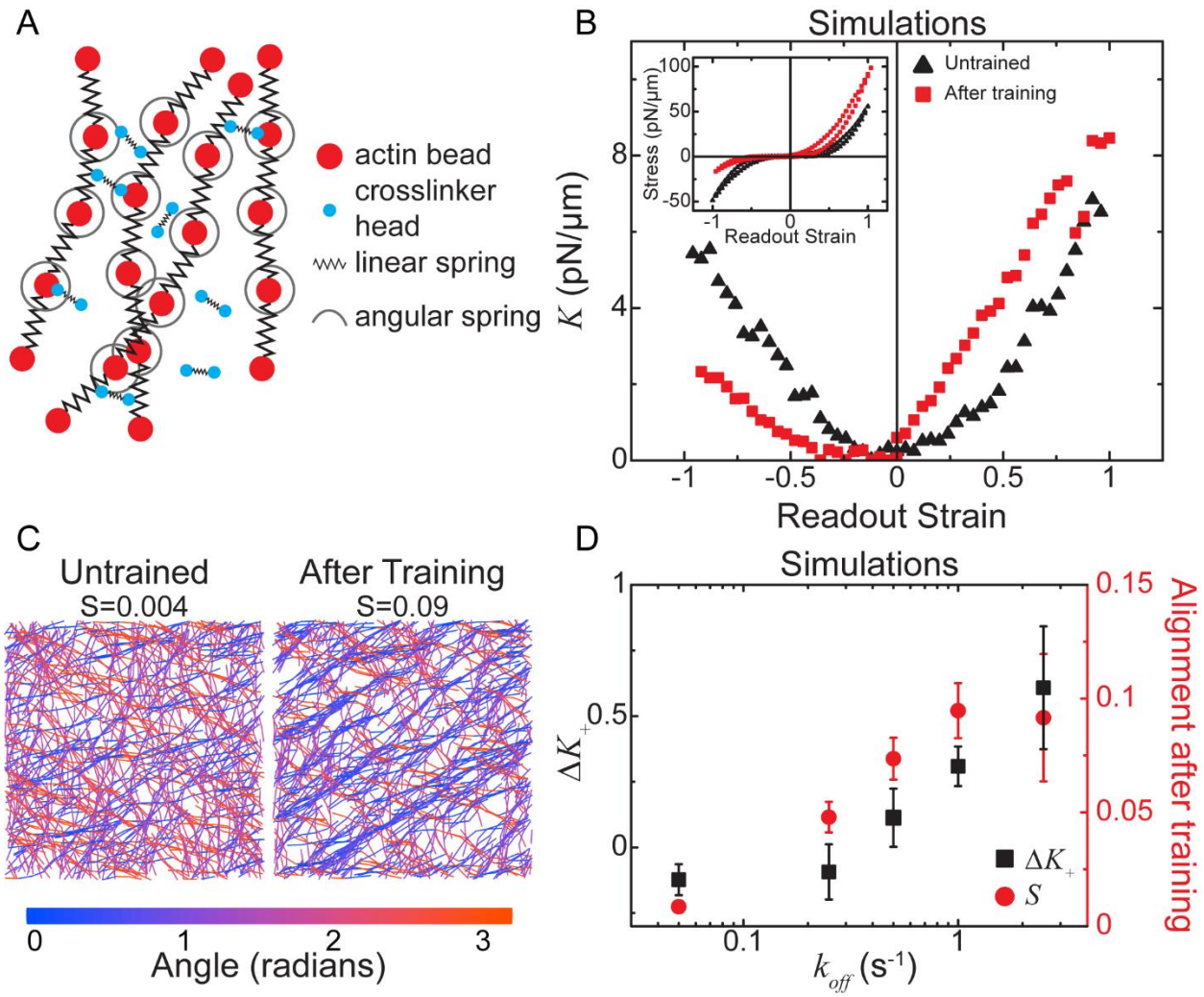

Figure 3.2: Simulated networks develop mechanical hysteresis due to alignment of filaments during training. (A) Schematic of the AFINES model. Filaments and cross-linkers are parametrized as beads connected by springs with cross-linkers able to bind and unbind according to a kinetic Monte Carlo scheme. (B) The differential modulus K, as measured in simulations before (black triangles) and after (red squares) training. Inset: The corresponding stress during readout. Data from simulations with $k_{off} = 0.5\ \mathrm{s}^{-1}$. (C) Images of simulated network after equilibration but before the onset of training (left) and after training immediately before readout (right). Color corresponds to filament orientation. (D) ΔK_+ (black squares) and filament alignment S (red circles) in simulated networks with varying cross-linker off rate. All simulations shown have $R_{Sim} = 9\ \mu\mathrm{m}^{-2}$, $l = 0.15\ \mu\mathrm{m}$, and $f = 100\ \mathrm{pN/\mu m}$. Error bars are standard deviation of 5 independent simulations.

3.4.3 Dependence on Cross-linker Concentration

I next ask how altering the architecture of the network influences hysteresis by varying the cross-linker concentration, which impacts both network structure and rheology [52,67]. I begin by training experimental networks cross-linked with various concentrations of α-actinin, R_α, and observe a drastic change in the hysteresis. For example, Figure 3.3A shows a typical readout for a network with $R_\alpha = 5\%$, which responds differently to training than the previously shown network with lower R_α. Here, training has a minimal effect on the network for strains $\gamma > 0$, where the readout values of both stress and K do not change with training. In contrast, the differential modulus decreases drastically after training for $\gamma < 0$. Training can thus have a large effect in one direction, here $\gamma < 0$, while having almost no impact in the opposite one. These changes contrast with the previously shown network with $R_\alpha = 1\%$, where training affects K across all strains (Fig 1c). In this case, the effect of training is about equal in both directions. I thus observe asymmetry stemming from two independent responses. Training can make the network stiffer and increase K when $\gamma > 0$, and it can soften the network and decrease K when $\gamma < 0$. While the latter is interesting and is discussed further in the conclusions, here I focus on $\gamma > 0$, where K increases after training.

I further measure changes in K over additional cross-linker concentrations, specifically between $R_\alpha = 0.05$ and 10 molar percent relative to actin. Remarkably, ΔK_+ has a non-monotonic dependence on cross-linker concentration. While increasing cross-linker concentration initially corresponds to an increase in ΔK_+, for $R_\alpha > 1\%$ the degree of mechanical hysteresis actually decreases (Figure 3.3B). Maximum hysteresis is thus achieved at $R_\alpha \approx 1\%$. I can understand the initial increase in ΔK_+ with concentration by comparing it to the onset of

strain stiffening. At low concentration of $R_\alpha \leq 0.2\%$ where ΔK_+ is close to zero (Figure 3.3B, gray region), networks have a linear response to shear. Figure 3.3C shows a typical example at $R_\alpha = 0.2\%$, where K is relatively constant regardless of strain. ΔK_+ begins to increase at $R_\alpha > 0.2\%$, which is importantly also the onset of a nonlinear shear response. At these concentrations K increases with the magnitude of strain, as shown in Figure 3.3D which depicts a typical example at $R_\alpha = 0.5\%$. The correspondence between strain stiffening and the increase in ΔK_+ is consistent with previous work, which found that similar nonlinearity was required for asymmetric response to strain in simulated actin networks [75]. It therefore makes sense that the onset of strain stiffening and hysteresis occur at the same concentration. While nonlinear shear response explains the increase in hysteresis at small cross-linker concentrations, to understand why it decreases at higher concentrations I turn to simulations.

In simulations, I can directly probe the microscopic structure of networks to investigate why mechanical hysteresis decreases at high cross-linker density. First, I perform simulations from cross-linker concentrations of 3 μm^{-2} to 15 μm^{-2} to ensure the results are consistent with experiments. Indeed, in these simulations ΔK_+ exhibits a non-monotonic dependence on cross-linker concentration (Figure 3.3E). As shown in Figure 3.2C, in simulation, training is related to an increase in network alignment, so I ask whether such an effect could explain the non-monotonicity. As before, I interrogate the alignment of the network after training but before readout. I find that when I plot alignment after training against ΔK_+ for each trial, a strong correlation emerges (Figure 3.3F). This plot indicates that while at low cross-linker concentrations the network is able to rearrange in response to training, at higher concentrations, the greater number of cross-linkers actually prevents such rearrangements and thus precludes the trained network from exhibiting a strong increase in K relative to untrained networks. The sole

outlier occurs at the lowest cross-linker concentration, where the density of cross-linkers is small enough to allow rearrangement without a corresponding increase in hysteresis. No matter how much they align under training stress, strain weakening networks do not exhibit mechanical hysteresis. Adjusting cross-linker density is one way to tune the mechanical hysteresis of a

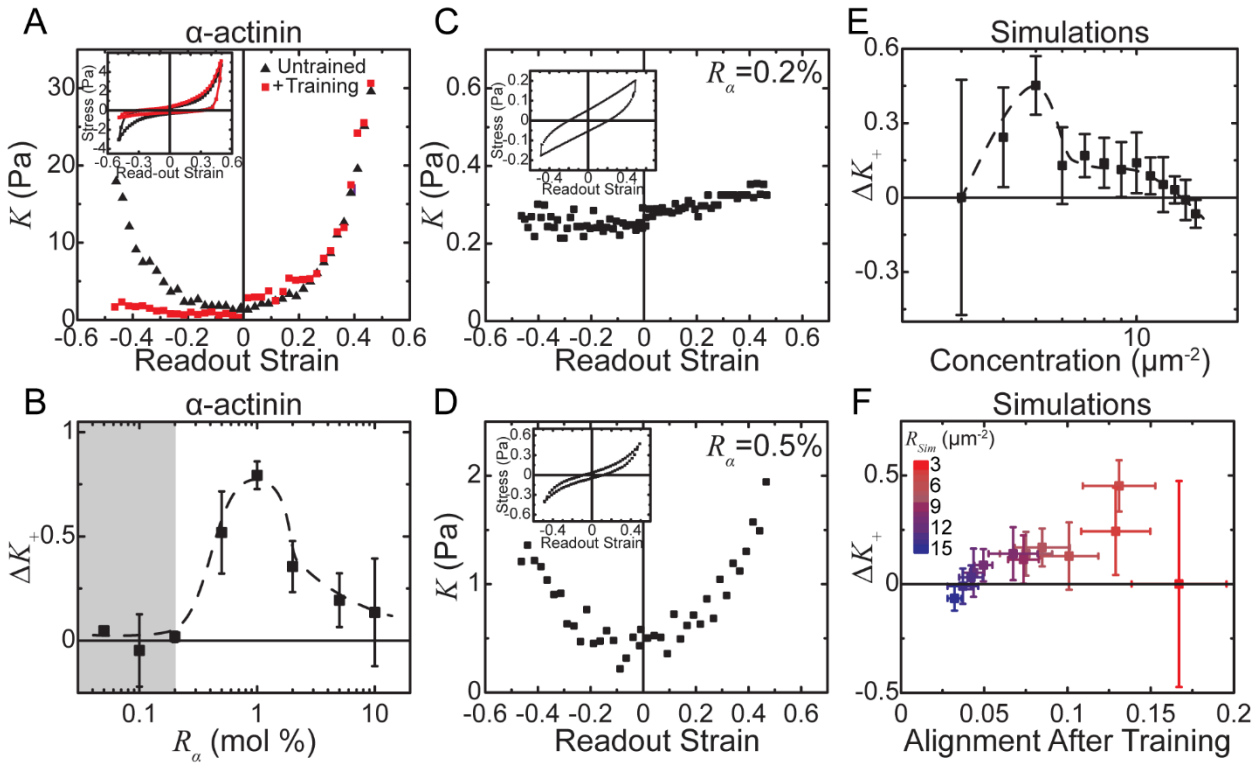

Figure 3.3: Hysteresis varies with cross-linker concentration. (A) K as a function of strain for a network with $R_\alpha = 5\%$ before (black triangles) and after (red squares) training. Inset: The corresponding stress vs. strain. (B) Hysteresis, characterized by ΔK_+, plotted as a function of α-actinin concentration. ΔK_+ is small at low and high concentrations with a peak around $R_\alpha = 1\%$. Gray region represents concentrations networks that do not strain stiffen. (C,D) The differential modulus K during readout of typical untrained networks with (C) $R_\alpha = 0.2\%$, where the network has a linear response to strain, or (D) $R_\alpha = 0.5\%$, where the network strain stiffens. Inset: the corresponding stress measured during readout. (E) ΔK_+ for different cross-linker concentrations in simulated networks. (F) More alignment of filaments after training correlates with increased ΔK_+ in simulations across all cross-linker concentrations that permit strain stiffening. Data is for $l = 0.15$ μm, $f = 100$ pN/μm, and $k_{off} = 0.5\ \mathrm{s}^{-1}$. Error bars in (B), (E), and (F) are standard deviation of at least two independent experimental samples or five independent simulations. Dotted lines in (B,E) are to guide the eye.

network by controlling both shear stiffening and filaments' ability to rearrange under stress. I now ask whether there are concentration independent mechanisms of tuning the response.

3.4.4 Impact of Cross-linker Properties

Thus far I have considered only α-actinin as the experimental cross-linker, but I know that networks connected by various cross-linkers can exhibit unique mechanical properties. As such, I now investigate how the physical properties of the cross-linkers in these networks affects mechanical hysteresis. Specifically, I compare networks cross-linked by α-actinin to ones cross-linked with two variants of filamin: from Dictyostelium discoideum (ddFLN) and from humans (FLN) (Figure 3.4A). These proteins allow me to study the importance of cross-linker length and flexibility on mechanical hysteresis. While, at 40 nm, ddFLN is about the same length as α-actinin, it is much more flexible [60,63] and therefore allows me to alter flexibility without changing length. FLN is similarly flexible, but with a contour length of approximately 160 nm [64]. Because it is much longer than the other two cross-linkers, it can be used to measure the impact of cross-linker length. These physical differences greatly impact the rheological properties of untrained networks, leading me to investigate their effect on mechanical hysteresis.

I find that, while ΔK_+ has different values and peaks at various concentrations depending on cross-linker, the non-monotonic dependence of hysteresis on cross-linker concentration is robust across all cross-linkers used. First, changing cross-linkers does not eliminate hysteresis, and networks cross-linked with ddFLN also develop hysteresis in response to training. Furthermore, ΔK_+, which increases at low cross-linker concentrations before peaking and subsequently decreasing at higher concentrations, has similar dependence on concentration as for networks cross-linked with α-actinin (Fig 4b). Despite the qualitative similarities, for networks cross-linked with ddFLN, the maximum hysteresis achieved, $\Delta K_+ = 0.47 \pm 0.05$, is smaller than that

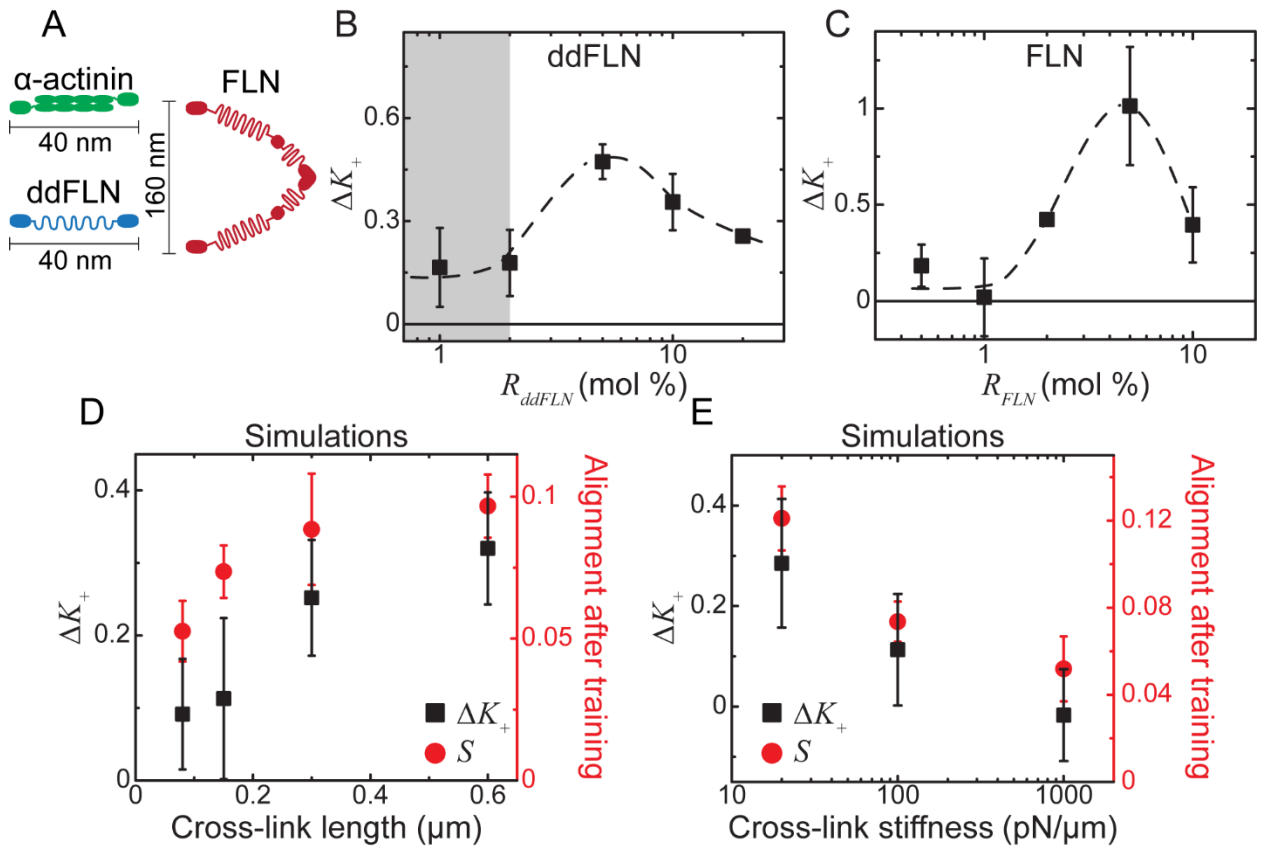

Figure 3.4: Hysteresis persists across a range of cross-linker properties. (A) Cartoon depiction of the different cross-linkers used. (B,C) ΔK_+ at varying concentrations of (B) ddFLN or (C) FLN. Dotted lines are to guide the eye. (D,E) ΔK_+ (black squares) and nematic order parameter S (red circles) in simulated networks with varying cross-linker (D) length, (E) stiffness. Simulations are with $R_{Sim} = 9\ \mu m^{-2}$, $l = 0.15\ \mu m$, $f = 100\ pN/um$, and $k_{off} = 0.5\ s^{-1}$, unless otherwise noted. Error bars in each panel are standard deviation of at least two independent experimental samples or five independent simulations.

of α-actinin networks, which have a maximum $\Delta K_+ = 0.79 \pm 0.05$. Additionally, these maxima occur at different concentrations. Whereas in α-actinin networks ΔK_+ peaks at $R_\alpha \approx 1\%$, ddFLN networks show a peak ΔK_+ at $R_{ddFLN} \approx 5\%$. Notably, though it occurs at a different concentration, the initial increase in ΔK_+ in ddFLN networks still corresponds to the onset of strain stiffening (Figure 3.5). Similarly, hysteresis in human FLN networks has a non-monotonic concentration dependence, but with a higher peak value (Figure 3.4C). As with ddFLN, the

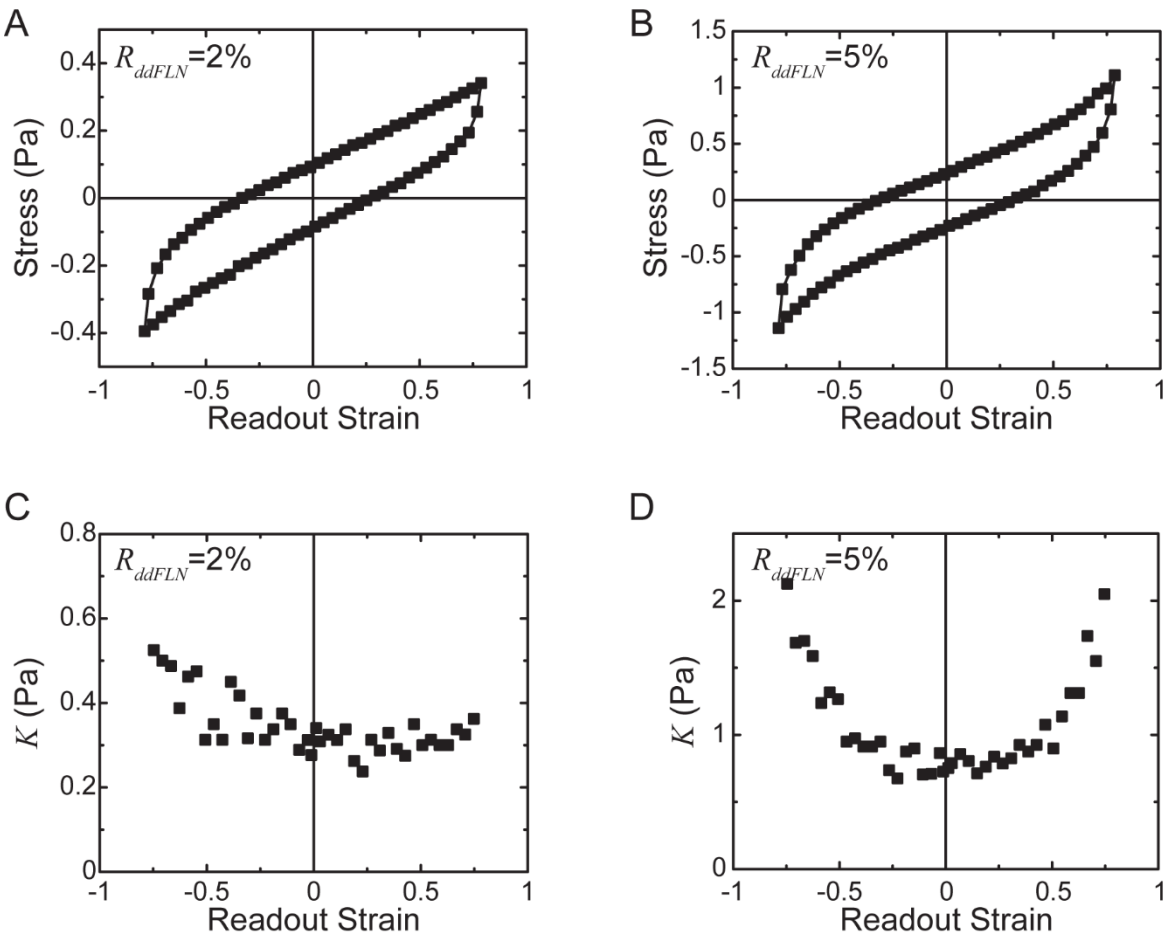

Figure 3.5: Strain stiffening in ddFLN networks. (A,B) Stress during readout for untrained ddFLN networks with (A) $R_{ddFLN} = 2$ or (B) $R_{ddFLN} = 5\%$, concentrations at which the network has a linear or nonlinear response to strain, respectively. (C,D) The corresponding differential modulus K for networks with (C) $R_{ddFLN} = 2\%$ or (D) $R_{ddFLN} = 5\%$.

concentration dependence of ΔK_+ in FLN networks peaks at $R_{FLN} \approx 5\%$. However, with $\Delta K_+ = 1.01 \pm 0.31$, the maximum response of FLN networks is about twice as high as of those cross-linked with ddFLN. These cross-linkers follow the same trend observed in α-actinin networks, where hysteresis depends non-monotonically on cross-linker concentration. On the other hand, cross-linker properties do affect the magnitude of hysteresis. Because natural cross-linkers vary along a number of axes simultaneously, it is difficult to untangle how each physical difference

contributes to the change in response. As such I turn again to simulation, where I are able to alter cross-linker properties independently.

Inspired by the difference between FLN and the other two cross-linkers, I examine how cross-linker length and flexibility impact mechanical hysteresis. In these simulations I fix $k_{off} = 0.5\ s^{-1}$ and $R_{Sim} = 9$ μm^{-2}, a concentration at which there is still some hysteresis but where the high concentration precludes most of the training induced alignment seen at the peak. As I vary cross-linker length from $l = 0.08$ μm to $l = 0.6$ μm, I find a corresponding increase in the magnitude of ΔK_+ from $\Delta K_+ = 0.09 \pm 0.08$ to $\Delta K_+ = 0.32 \pm 0.08$ (Figure 3.4D). This increase is accompanied by an increase in filament alignment. Another potentially important difference between experimental cross-linkers is their stiffness. I vary stiffness of $l = 0.15$ μm cross-linkers from $f = 20$ pN/μm to $f = 1000$ pN/μm and find that both ΔK_+ and S decrease with increasing stiffness (Figure 3.4E). Networks with longer or more flexible cross-linkers are thus more able to rearrange during training, leading to increased hysteresis, similar to the effect seen at high k_{off} or cross-linker concentrations. It makes sense that short or rigid cross-linkers constrain the rearrangement of actin filaments more than long or flexible cross-linkers. I thus look at how well alignment predicts hysteresis.

When I varied cross-linker concentration and properties I found that the changes in hysteresis correlated with alterations in network alignment after training, leading me to ask how well alignment explains hysteresis across all conditions. Remarkably, when I plot alignment against ΔK_+, changes due to altering different cross-linker physical properties or concentration collapse to a single line (Figure 3.6). This trend suggests that the ability of the constituent filaments to rearrange under training stress is the main determinant of ΔK_+ in these networks. I thus find two

conditions necessary for mechanical hysteresis: the network needs to strain stiffen, and filaments must be able to rearrange under stress.

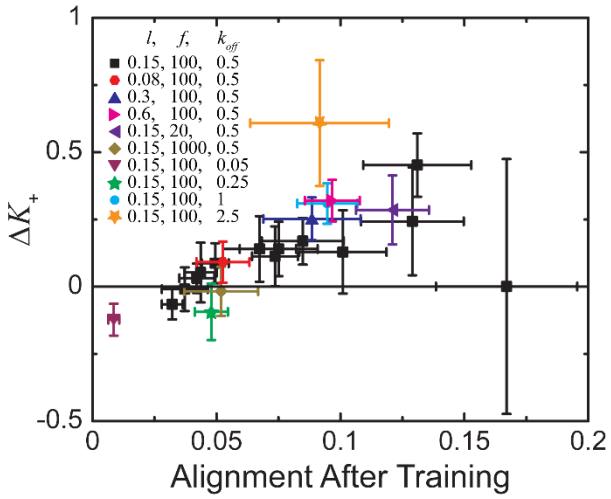

Figure 3.6: ΔK_+ increases with filament alignment across all cross-linker parameters in simulations. All data with $R_{Sim} = 9\ \mu m^{-2}$, except black squares which represent a variety of concentrations as shown in Fig 3f. Error bars are standard deviation of five independent simulations.

3.5 Conclusion

I have shown that cross-linked actin networks display mechanical hysteresis in the form of a direction-dependent response to shear after the application of a training stress. This asymmetry results from an increase in K compared to the untrained network for $\gamma > 0$, and a decrease in K for $\gamma < 0$. I find that this increase, characterized by ΔK_+, changes non-monotonically with cross-linker concentration. Importantly, ΔK_+ begins to increase at the same concentration as the onset of strain stiffening. Using simulations where I can directly observe internal structural changes, I find that the decrease in ΔK_+ at high concentrations corresponds to a drop in filament alignment after training. Furthermore, increasing the unbinding rate, flexibility, or length of cross-linkers also increases alignment, leading to higher values of ΔK_+. This form of mechanical hysteresis

thus depends on two conditions: the network having a nonlinear response to strain and the ability of the constituent filaments to rearrange under stress.

While alignment describes the increase in K for $\gamma > 0$, I also observe a second manifestation of mechanical hysteresis that is not so readily explained. In addition to its increase at positive strains, I observe that training leads to a decrease in K for $\gamma < 0$. This effect increases with cross-linker density and becomes especially pronounced at high concentrations even as filament alignment and ΔK_+ decrease. It is thus possible to tune not only the degree of hysteresis observed but also its structure. These simulations, however, are unable to replicate the effect of cross-linker concentration on K for $\gamma < 0$. Instead, in simulations the decrease in K at these strains is remarkably consistent regardless of the concentration or physical properties of the cross-linkers. This discrepancy could be due to the lack of filament entanglement in the simulation, but further research will be necessary to determine how this might affect K for $\gamma < 0$.

This study demonstrates a hysteresis response in cross-linked polymers that can be tuned by adjusting cross-linker properties and concentration. It can therefore inform the creation of materials that passively adapt to stress. It additionally suggests ways that the degree of mechanical hysteresis can be tuned through changes in the concentration and physical properties of the cross-linkers. While I have demonstrated several knobs that can be tuned to change this response, these results suggest that any other method of altering the amount of achievable alignment should also allow for the tuning of mechanical hysteresis. Future studies could look at additional ways to tune these responses. For example, it is possible that other factors such as actin turnover rate or length could affect the ability of filaments to both align under stress and maintain this alignment over time, allowing the creation of materials that adapt more quickly to stress. Additionally, these factors could tune how quickly networks relax back to their untrained

state, leading to mechanical hysteresis with shorter or longer lifetimes. It might also be possible to encode multiple hysteretic responses by training the network in an orthogonal direction. Finally, none of the required conditions are exclusive to actin networks, so other polymer networks could exhibit similar hysteresis, allowing the creation of stiffer, artificial materials that similarly adapt to stress. These studies would provide a greater understanding of how hysteresis responses can arise in both biological and artificial cross-linked networks.

CHAPTER 4

REGULATION OF ACTIN TURNOVER BY CROSS-LINKERS AND MYOSIN ACTIVITY

4.1 Preface

All experiments were performed by the author, except for TIRF imaging which was performed by Jonathan Winkelman. Cristian Suarez purified profilin and fluorescent cofilin, and he assisted with purification of mDia1. Cristian and David Kovar provided advice on protein use and sedimentation assays. Margaret Gardel provided input at every stage.

4.2 Introduction

To move and adapt to external stimuli, cells must be able to rapidly restructure the actin cytoskeleton. One method cells use is a dynamic process called turnover, where polar actin filaments continuously polymerize on their ATP-bound barbed ends while depolymerizing on their ADP-bound pointed ends [21]. This process is essential in cells and when it is prevented, for example with the addition of the drug phalloidin, they die [28]. As such, cells possess a myriad of proteins to regulate turnover by controlling the rate of nucleation, polymerization, severing, and depolymerization of actin filaments [12].

One important protein behind the regulation of turnover is cofilin, which enhances the severing rate of actin. Cofilin binds preferentially and cooperatively to ADP-actin at the pointed end [45,46], where it creates a mechanically weak point at the boundary between cofilin-coated and naked filaments. The filament then severs at this point due to thermal fluctuations [48,49]. Cofilin binding also increases the helicity of actin filaments, which can induce torsional stress

[24,25]. After severing, the ADP-bound daughter filament is unstable and would depolymerize on its own; cofilin accelerates this process [50].

In addition to components that regulate actin polymerization and severing, there are many actin binding proteins that control the local network architecture in cells and whose effect on turnover are less well studied. For example, actin can form space-spanning networks, parallel bundles, or apolar bundles depending on the cross-linkers used [18]**.** Additionally, these cross-linkers can dampen thermal fluctuations [99]. Since cofilin-mediated severing depends on these fluctuations, changes in actin architecture that affect them could have a similar impact on cofilin activity. Indeed, structure has been found to influence cofilin severing, with faster disassembly in branched versus bundled actin [100]. Previous research has also investigated the role of cross-linkers on disassembly, finding that cofilin severing is enhanced by bundling with either fascin [101], a short rigid cross-linker that forms parallel bundles, or biotin and neutravidin [25], a method of permanent cross-linking which also creates short, rigid bonds. Wioland *et al.* attributed this increase in severing to the introduction of twist constraint, which increased the torsional stress generated by cofilin binding. However, it is unclear whether a similar effect would occur in actin cross-linked by longer or less rigid cross-linkers which might provide less restraint than their shorter counterparts.

Another protein that has been linked to turnover is the molecular motor myosin. Myosin has been found to be able to disassemble actin in cells [35] and to be essential for turnover in cytokinesis [102,103] and neuronal growth cones [104]. This role in turnover is supported by reconstituted networks where myosin has similarly been shown to be able to disassemble actin [98,105] and, through buckling, to sever filaments [96,106]. Recently, myosin disassembly of branched, membrane-bound actin *in vitro* was found to be able to facilitate the assembly of new

filaments [107]. The underlying mechanics behind this process, however, are poorly understood and it is unclear whether it will persist in different actin architectures.

In this work, I address two questions surrounding actin turnover using a minimal system that allows me to regulate and measure turnover in reconstituted networks. First, I ask how cross-linking, specifically via α-actinin, impacts actin's turnover rate and find that the presence of α-actinin prevents cofilin-mediated severing and turnover. Next, I investigate the role of myosin in this process, as well as the mechanisms through which it can influence turnover. Here, I find that not only can myosin replace cofilin to sever actin and accelerate turnover, but this turnover persists even in the presence of α-actinin. I thus identify two methods of severing which can accelerate actin dynamics, and which are affected differently by α-actinin bundling.

4.3 Materials and Methods

4.3.1 Protein Purification

Actin, α-actinin and mDia1 are purified as described in Appendix A.2.

Skeletal muscle myosin II is purified from chicken breast as described in [161] and labeled with Alexa 488 or 647 [162] and is a gift from Samantha Stam. Human cofilin and profilin are separately expressed in E. coli and purified as previously described [41]. Human cofilin is a gift from Patrick McCall. Yeast cofilin is from S. cerevisiae and was expressed in E. Coli strain Rosetta2(DE3)pLysS, purified, and labelled as previously described [49]. All proteins are drop-frozen in liquid nitrogen and stored at -80 ˚C until use. After thawing, proteins are stored at 0-4°C and used within 7 days, except for actin and myosin which are used within 24 hours, and profilin which is used within 3 months.

To remove inactive heads, before use myosin is mixed with phalloidin stabilized filamentous actin (F-actin) in 1:4 myosin to actin molar ratio in a buffer composed of 20 mM MOPS, 500 mM KCl, 4 mM $MgCl_2$, 0.1 mM EGTA, 1 mM ATP, pH 7.4 and centrifuged at 223,000 g for 30 min, with the supernatant being retained and used for experiments.

4.3.2 Confocal Network Preparation

For confocal microscopy, the experimental chamber is composed of a glass cylinder (3 Corning Life Sciences; 166-10) epoxied to a glass coverslip (Fisherbrand, #1.5). The coverslip surface is passivated against protein adhesion through an oil-surfactant layer as described in Appendix A.3. Shortly before use, a roughly 4x4 cm Teflon square is placed in the center of the coverslip which was then exposed to UV/ozone for 10 min.

Immediately before use, G-actin incubates in ME buffer for 2 min. To form actin networks, 2 μM actin monomer (0.2 μM labelled with TMR) is added to KMEI along with 6 μM profilin, 0.01 μM mDia1, 2 mM ATP, 0-5 nM filamin, 0.2 wt% 15 cP methylcellulose, and an oxygen scavenging system (4.5 mg/mL glucose, 2.7 mg/mL glucose oxidase (Calbiochem; 345486), 1,700 units/mL catalase (Sigma; 02071), and 0.5 vol% β-mercaptoethanol). This mixture is immediately added to the sample chamber. Samples are incubated for at least 90 min before being photobleached for FRAP and 120 min before the addition of 5-35 nM of myosin.

4.3.3 Confocal Microscopy

For confocal microscopy, samples are imaged using a Ti-E (Nikon) inverted microscope equipped with a CSU-X confocal scanner (Yokogawa) and a 40x 1.30NA objective (Nikon), illuminated using a 491, 561, or 642 nm laser (Cobolt, MPB Communications, Coherent). Images are collected using a Zyla sCMOS (Andor) camera. Samples are photobleached by illuminating for 3-5 s with a 405 nm laser directed to a circular region using a Mosaic mirror

array (Andor). Samples with myosin are photobleached after myosin deposits at the bottom of the chamber but before it begins to clump into asters, which occurs approximately 400 s after the addition of myosin.

4.3.4 FRAP Image Analysis

All image analysis is done in ImageJ or using custom MATLAB code. Prior to analysis, the dark intensity measured in regions outside the laser's illumination is subtracted. Photobleached regions are tracked either by using the StackReg plugin for ImageJ [163] or by hand. To negate the impact of uneven illumination near the image edge, when photobleached region moved close to the edge of the field of view, all subsequent recovery data is discarded. The average intensity in a 10 μm radius circle at the center of the photobleached region is measured to track intensity recovery.

As previously observed [164], although myosin is uniformly distributed within a given field of view, myosin density varies across the whole network. As a result, I quantify myosin using its local density. Myosin images are cropped to remove the effects of uneven illumination near the edges, then the ImageJ smooth function is applied twice to remove noise. The identify particles function is used to count the number of myosin puncta in each frame, ignoring any particles smaller than 0.25 μm^2. The resulting number is divided by the area of the image to calculate density. When comparing to FRAP data for Figure 4.4D, myosin density 100 s after photobleaching is used.

4.3.5 TIRF Microscopy

Total internal reflection fluorescence microscopy (TIRF) was conducted using a Ti-E (Nikon) inverted microscope equipped with a 100x 1.49 NA objective (Nikon) illuminated using a 561 or 642 nm laser (MPB Communications, Coherent). Microscope slides and coverslips are

cleaned using UV/ozone, then incubated overnight in a solution of 1 mg/mL mPeg-Silane (5,000 MW) in 95% ethanol, pH 2.0. Flow cell chambers are composed of passivated coverslips attached with parallel strips of double sided tape. 2 μM of actin (0.2 μM labelled with TMR) in a buffer composed of KMEI with 2 mM ATP, 0.2 wt% 15 cP methylcellulose, oxygen scavenging system and 0 or 1 μM α-actinin is added to the chamber. Actin polymerizes for at least 600 s before 0.04 μM fluorescent cofilin is added.

4.3.6 Sedimentation Assay

For the sedimentation assay, 20 μM of actin is added to KMEI buffer and allowed to polymerize for at least 60 min. 3 μM of the resulting F-actin are mixed with various concentrations of α-actinin. After an additional 30 min, 3 μM of yeast cofilin is added. The solution is then centrifuged at 100,000 g for 20 min after which the supernatant and resuspended pellet are collected and run on a precast SDS-page gel (Bio-Rad; 4561043). Band intensity is measured in ImageJ by taking the total intensity in a rectangular region completely surrounding a single band and subtracting the background intensity measured in an identical region directly above or below.

4.3.7 Imaging Actin Length Buckling

Filament buckling is imaged using sparsely labelled networks in which 4% of filaments are labelled. 2 μM of unlabeled G-actin is added to KMEI with 6 μM profilin, 0.1-0.01 μM mDia1, 2 mM ATP, 2 μM phalloidin, and the previously described oxygen scavenging system, and allowed to polymerize for at least 90 min. Simultaneously, a second population of labeled G-actin (1.8 μM unlabeled, 0.2 μM TMR-actin) is similarly prepared. The two solutions are mixed, resulting in a 1:25 ratio of labeled to unlabeled filaments, and 180 μL of the mixture is added to a

cylindrical imaging chamber along with 18 μL of 3 wt% methylcellulose. At least 30 min later, 10-35 nM of myosin is added.

4.3.8 Measuring Actin Length and Curvature

Actin filaments are traced using the JFilament plugin for ImageJ [165], from which length and curvature are calculated using custom MATLAB code. Length is measured in four independent samples, two with 0.01 μM mDia1 and two with 0.1 μM. For initial length, $n > 200$ filaments are measured per sample from either before the addition of myosin or within 100 s of myosin being added, which is before the start of myosin induced flows. Length with myosin is similarly measured in $n > 200$ filaments at $t \geq 1500$ s for 0.01 μM mDia1 or $t \geq 300$ s for 0.1 μM mDia1, which is after myosin contractions begin. While the data shown in Figure 4.7 represents all trials combined, average filament length decreases with myosin in both samples with 0.01 μM mDia1 when taken separately and is unchanged by myosin in both samples with 0.1 μM mDia1. Curvature is measured at each point of randomly selected filaments, after which a rolling median is taken along the length of the filament to smooth noise and remove outliers. Selected filaments are tracked over time and the maximum curvature achieved at any time point is measured.

4.4 Results and Discussion

4.4.1 α-actinin Prevents Cofilin from Severing Actin

To study turnover *in vitro*, I must first increase the turnover rate in reconstituted networks. While in cells actin filaments turn over on the order of seconds to minutes, purified actin has negligibly slow turnover on the order of hours without additional actin binding proteins to accelerate the process [41]. I enhance and regulate the turnover rate *in vitro* using a system

adapted from McCall *et al.*, which controls the depolymerization and nucleation of actin through the proteins cofilin, profilin, and mDia1 (Figure 4.1A). Cofilin increases depolymerization at the barbed end by enhancing the severing rate of actin, after which the cofilin covered daughter filament is inherently unstable and depolymerizes. Profilin and the formin mDia1 control the nucleation and polymerization rates. Profilin, which greatly reduces the nucleation of actin monomers into oligomers [33], prevents the formation of new filaments, and therefore ensures that any actin removed by cofilin can only polymerize onto an existing barbed end. Since profilin would greatly slow the initial formation of actin networks, I use the formin mDia1, which enhances actin nucleation [31,32]. A higher mDia1 concentration increases the number of filaments and thus decreases their average length. After forming a new filament, mDia1 remains bound to the barbed end where, in conjunction with profilin, it increase the polymerization rate [34]. Together, these three proteins increase the turnover rate in reconstituted actin networks [41].

Using this system, I first investigate the effect of the α-actinin, a rigid cross-linker that is ~35 nm long [62], on actin turnover. Here, I use 1 μM of α-actinin, which is sufficient to bundle actin in these networks. To measure turnover rate, I use fluorescence recovery after photobleaching (FRAP), where I photobleach a circular region with radius ≈22 μm of fluorescent actin and measure the extent to which the intensity recovers. Using FRAP, I examine networks containing 1 μM of human cofilin, half the concentration of actin, which is the ideal concentration for maximum severing [49]. I find that the photobleached region recovers over time (Figure 4.1B). McCall *et al*. previously observed a similar recovery, and found that it corresponded to turnover of actin filaments as bleached monomers are replaced with fluorescent ones [41]. In contrast, the addition of α-actinin prevents the dark region from recovering. To quantify the difference in

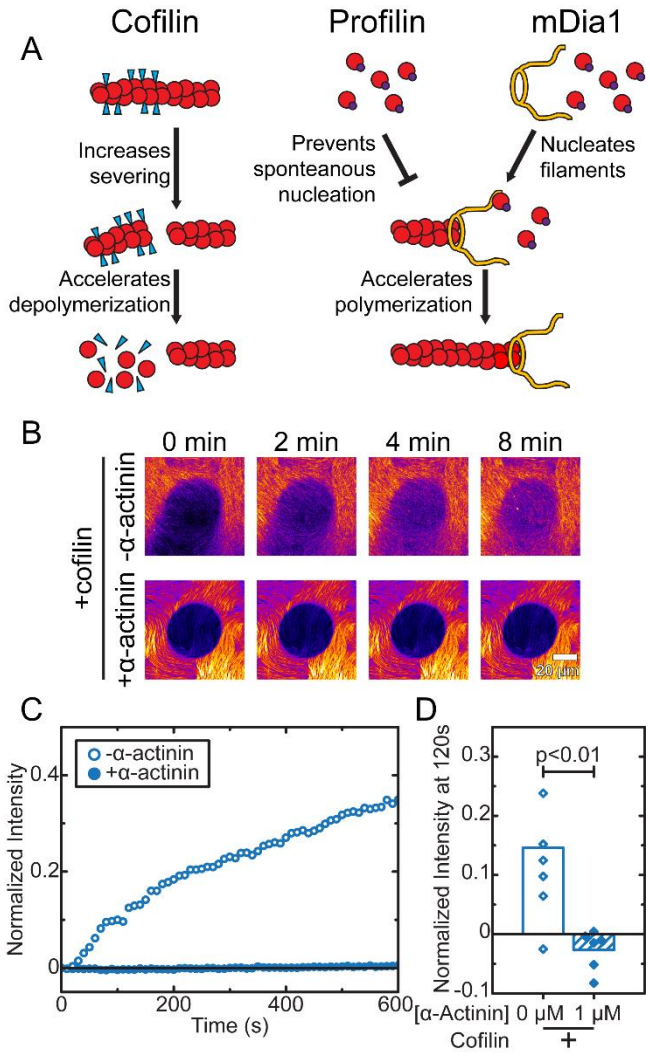

Figure 4.1: α-actinin suppresses turnover in networks with cofilin. (A) Schematic of proteins used to enhance turnover *in vitro*. Cofilin binds at the pointed end of actin filaments, where it increases the severing rate and accelerates the depolymerization of the cofilin coated daughter filament. In conjunction, profilin and the formin mDia1 regulate the nucleation of actin monomers into filaments and accelerate polymerization at the barbed end. (B) Pseudocolor images depicting fluorescence recovery after photobleaching at time $t = 0$ in networks without (top) or with (bottom) 1 μM of α-actinin. Scale bar is 20 μm. (C) Normalized intensity over time, measured as the average intensity in a 10 μm radius circle at the center of the photobleached regions depicted in Figure 4.1B. (D) Normalized intensity 120 s after photobleaching for networks without (open) or with (closed) α-actinin. Diamonds represent individual trials, while bars are averages across all trials. The means are significantly distinct with p=0.008. P values here and in all figures were measured using a 2-sample t-test without assuming equal variance. Data are from networks with cofilin concentrations of 1 μM.

fluorescence recovery, I measure average intensity I in a circle of radius 10 μm at the center of the photobleache region. By measuring I only in the center of the region, I limit the effect of flows and fluctuations at the edges. Intensity is additionally normalized as $I_{normal} = (I - I_{bleach})/(I_{initial} - I_{bleach})$, where $I_{initial}$ and I_{bleach} are the intensities immediately before and after photobleaching, respectively. $I_{normal} = 1$ thus corresponds to full recovery, while $I_{normal} = 0$ represents no recovery. I then look at changes in I_{normal} after photobleaching at time $t = 0$. Without cross-linking, the intensity steadily increases over time (Figure 4.1C). However, in networks with α-actinin, the intensity is constant and remains at its initial value of $I_{normal} \approx 0$. I repeat this assay over many samples and measure the normalized intensity 120 s after photobleaching. 120 s is chosen since for shorter times the recovery is small compared to noise, while over longer times the region can drift out of frame, but choosing different time durations does not impact these results (Figure 4.6). I observe a statistically significant decrease in intensity with the addition of α-actinin (Figure 4.1D). In fact, in cross-linked networks I consistently observe no recovery at all. While uncross-linked networks have a normalized intensity of 0.15 on average 120 s after photobleaching, in the presence of α-actinin the average normalized intensity is negative. Since this recovery is driven by turnover, I conclude that α-actinin prevents actin turnover in these networks.

To probe the mechanism behind this decrease in turnover, I examine the effect of α-actinin on cofilin binding and severing. Using total internal reflection fluorescence microscopy (TIRF) and fluorescent yeast cofilin, I can directly image both binding and severing of actin filaments. I note that while the fluorescent cofilin is from yeast instead of humans, α-actinin similarly prevents florescence recovery in these networks. With no cross-linking, as cofilin binds to actin the filaments depolymerize relatively quickly, and after 8 min I observe a much lower density of

filaments (Figure 4.2A). In contrast, actin cross-linked by α-actinin is unchanged by the addition of cofilin. I quantify depolymerization by measuring the average intensity in the actin channel across the entire field of view, I_{Actin}, divided by its value 100 s after the addition of cofilin, $I_{t=100}$. While the intensity of uncross-linked actin decreases quickly, in the presence of α-actinin

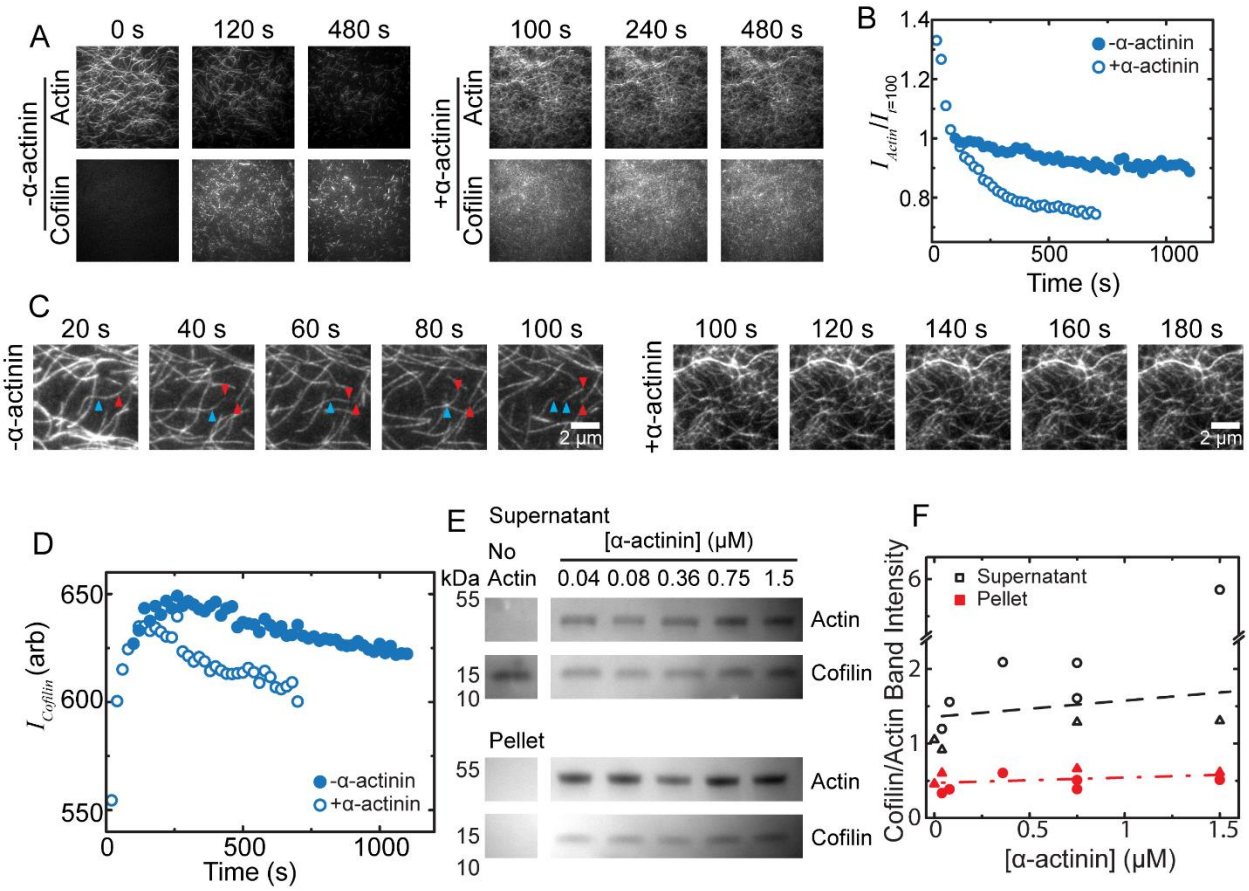

Figure 4.2: α-actinin reduces cofilin severing but not binding. (A) TIRF images showing actin disassembly after the addition of cofilin at time $t = 0$ in networks with no α-actinin (left) compared to those with 1 μM of α-actinin (right). (B) Average actin intensity across the entire frame, divided by its value at 100 s. (C) Zoomed in images of the networks from Figure 4.2A depicting two severing events (arrows) in an actin network with no α-actinin (*left*). In networks with α-actinin, no severing events are observed (*right*). (D) Average cofilin intensity over time for the networks depicted in Figure 4.1A. Data in (A-D) are from networks with 0.04 μM cofilin. (E) Image of gel from sedimentation assay comparing cofilin binding at various concentrations of α-actinin, as well as a control prepared with no actin. (F) Ratio of intensities in the cofilin over the actin bands for the supernatant (black, open symbols) or pellet (red, closed). Different symbol shapes correspond to independent trials. Dotted lines are fits to guide the eye.

$I_{Actin}/I_{t=100}$ is relatively stable and decreases much more slowly over time (Figure 4.2B). α-actinin therefore greatly reduces cofilin's ability to depolymerize actin networks. Additionally, I directly observe severing of unbundled actin filaments, but I could not identify any severing events in actin cross-linked with α-actinin (Figure 4.2C). Having observed that α-actinin prevents cofilin from severing and depolymerizing actin, I next explore the underlying mechanism. One possibility is that α-actinin prevents cofilin from binding. To test this possibility, I first measure the average cofilin intensity in TIRF and find it is unaffected by the addition of α-actinin (Figure 4.2D). I note that without further calibration this intensity does not measure cofilin concentration. However, the similarities suggest these is roughly equivalent cofilin in both

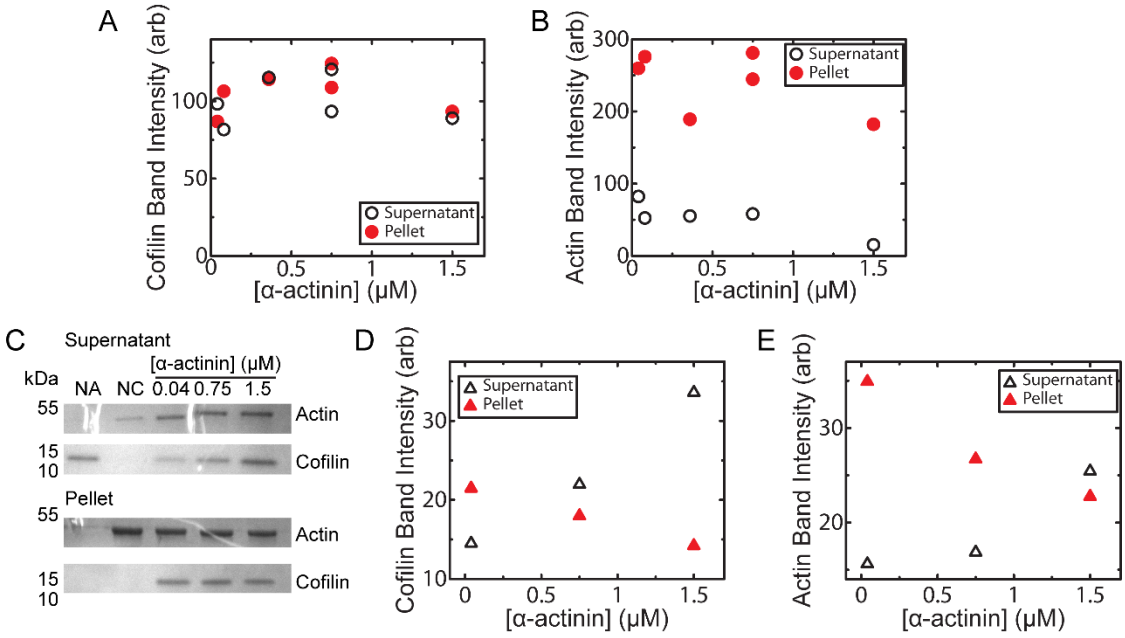

Figure 4.3: Sedimentation assay results for actin and cofilin. (A,B) Band intensity for cofilin (A) or actin (B) corresponding to the trial depicted in Figure 4.1E and the circles in Figure 4.1F. (C-E) Results of a second, independent trial corresponding to the triangles in Figure 1F. (C) Image of gel from sedimentation assay comparing cofilin binding at various concentrations of α-actinin, as well as a control prepared with no actin (NA) or no cofilin (NC). (D,E) Band intensity for cofilin (D) or actin (E).

cases. I further measure cofilin binding using a sedimentation assay where actin filaments, along with cofilin and various concentrations of α-actinin, are centrifuged at 100,000 g. At this acceleration, filaments will sediment along with any cofilin bound to them, while unbound cofilin remain suspended in solution. Higher binding affinity leads to a higher concentration of cofilin in the pellet and lower concentration in the supernatant [166]. I measure the resulting concentrations of cofilin and actin by measuring band intensity on an SDS-page gel (Figure 4.2E). The intensity of the actin band can vary (Figure 4.3), so I measure the ratio of the cofilin to actin band intensities to measure the concentration of cofilin relative to actin. In both the supernatant and pellet, this ratio is independent of α-actinin concentration, suggesting that α-actinin does not influence cofilin binding (Figure 4.2F). While α-actinin prevents cofilin from severing actin filaments, it does not do so by preventing binding.

4.4.2 Myosin Activity Enhances Actin Turnover

Finding that α-actinin prevents cofilin mediated severing, I ask if myosin can be used instead to sever filaments and enhance turnover. I now use FRAP to examine turnover in networks with no cofilin. With no myosin, the photobleached region stays dark with $I_{normal} \approx 0$ over 600 s (Figure 4.4A, B). As previously seen with α-actinin, fluorescence recovery in these networks depends on cofilin mediated severing, so it is unsurprising that it vanishes when cofilin is removed completely. The addition of myosin, however, rescues fluorescence recovery, leading to a steady increase in intensity over time (Figure 4.4A, B). Repeating this measurement over many samples shows a consistent and statistically significant increase in intensity compared to cases without myosin (Figure 4.4C). Furthermore, this increase depends on myosin activity. Eventually, all the myosin clusters and flows stop, at which point there is no longer recovery in new photobleached regions (Figure 4.4C, “After”). This recovery therefore depends not only on

the presence of myosin, but on its activity. While these measurements are taken at various concentrations of myosin, interestingly above small concentrations this recovery does not depend on myosin density and plateaus for densities greater than ~0.005 μm^{-2} (Figure 4.4D). Previous work found that myosin generated strain similarly plateaus above a critical myosin density, suggesting cooperativity and a transition in force percolation [164]. Overall, myosin is able to enhance recovery after photobleaching. Since myosin induced recovery resembles that previously discussed in cofilin networks, I ask if it also originates from actin turnover.

While observed recovery could be due to actin turnover, it could also be due to another process such as diffusion of filaments or advection from myosin induced flows, so I seek to differentiate between these possible origins. First, I add the drug phalloidin, which is known to stop actin turnover by preventing filament disassembly [28]. With phalloidin and myosin, a photobleached region still recovers over time, albeit slower than in networks without phalloidin (Figure 4.5A). However, while I still observe an increase in recovery with the addition of myosin compared to the case with no motors, it is significantly less than in the networks with no phalloidin (Figure 4.5B). While some of the observed myosin induced recovery might have a different origin, a significant part depends on the disassembly of actin filaments.

I can also exploit the uniformity of turnover throughout the network to differentiate between possible mechanisms behind recovery. On average, turnover is independent of location and occurs in all filaments equally. Recovery due to turnover is therefore consistent throughout the photobleached area. In contrast, both diffusion and advection affect the edges first as new actin flows into the dark region [41]. As a result, turnover driven recovery is independent of the size of the photobleached region, while recovery due to diffusion or advection decreases with the size as it takes longer for filaments to travel from the edges to the center. Indeed, when I approximately

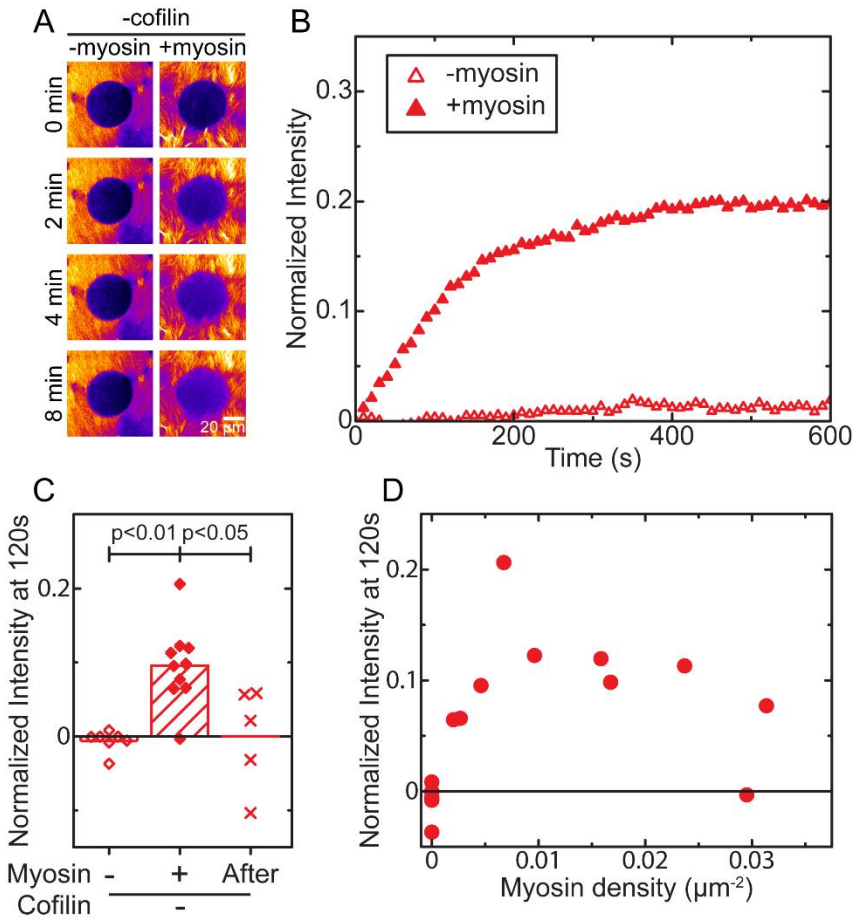

Figure 4.4: Myosin enhances the rate of fluorescence recovery in systems without cofilin. (A) Pseudocolor images depicting fluorescence recovery of photobleached regions in networks without (left) or with (right) myosin. (B) Normalized intensity over time quantifying the recovery depicted in Figure 4.4A. (C) Normalized intensity 120 s after photobleaching for networks with no myosin (open diamonds), with myosin (closed diamonds), or after myosin generated flows have stopped (X's). (D) Normalized intensity 120 s after photobleaching for various densities of myosin.

double the radius of the region from ≈22 μm to ≈42 μm, there is no significant change in fluorescence recovery (Figure 4.5C). I can also differentiate between mechanisms by examining the intensity profile of the photobleached region and how it changes during recovery. Here, since turnover driven recovery occurs at the same rate throughout it preserves the shape of the intensity profile, whereas advection or diffusion first affect the edges. I quantify this profile by calculating the azimuthally averaged intensity as a function of radius from the center of the

region, $\langle I \rangle$, and subtracting $\langle I \rangle_{Max}$, its maximum value within radius r <32 μm. Plotting $\langle I \rangle - \langle I \rangle_{Max}$ reveals that recovery is uniform throughout and occurs at the same rate regardless of radius (Figure 4.5D). Furthermore, the general shape of the region is constant. Notably, there is almost no change in shape at 120 s, the time at which I measure recovery (Figure 4.5D, black dotted line). Finally, I quantify changes to the intensity profile by looking at the width of the dark region over time. Width increases during diffusion driven recovery but remains constant in uniform recovery such as turnover [41]. Indeed, I find that width is constant over time, consistent with recovery due to turnover. The observed recovery both depends on filament disassembly and is constant throughout the photobleached region, leading me to conclude that it is due to turnover of actin filaments.

4.4.3 Buckling and Severing by Myosin Increases Actin Turnover Rate

I next investigate the mechanics behind myosin-mediated turnover by testing the importance of actin buckling and severing. Previously, preventing cofilin severing eliminated turnover. Since myosin is able to replace cofilin and enhance turnover, it is possible that myosin is similarly taking the role of severing actin. Earlier work has found that myosin can sever actin by buckling filaments until they break [96], so I aim to decrease the amount of buckling in these networks by decreasing the average filament length. Shorter filaments behave more like rigid rods and are thus less susceptible to buckling [18]. To decrease length, I increase the concentration of mDia1 from 0.01 μM to ≥0.1 μM. Using FRAP to measure turnover, I find that higher concentrations significantly reduce the observed recovery (Figure 4.7A). While I vary the concentration of mDia1 between 0.1 and 0.4 μM, changes over this range of concentrations do not impact the recovery rate. I note that higher formin concentration increases the number of barbed ends which could potentially increase the polymerization rate. The fact that more barbed ends does not lead

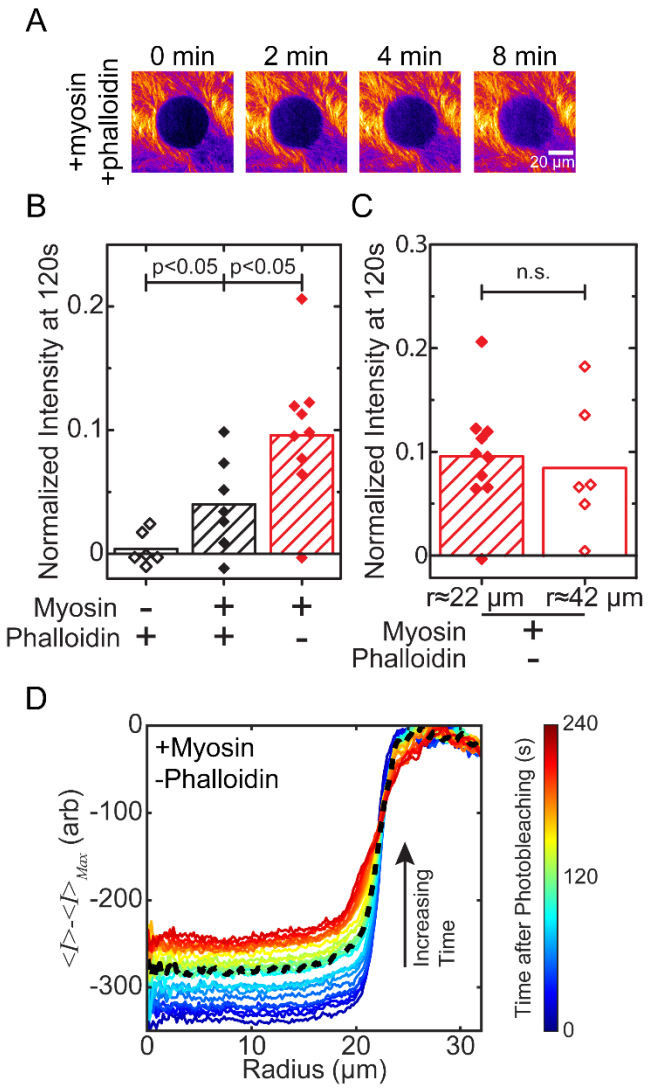

Figure 4.5: Fluorescence recovery depends on actin disassembly and is uniform throughout the photobleached region consistent with turnover-mediated recovery. (A) Pseudocolor images depicting fluorescence recovery of photobleached regions in networks with myosin and the drug phalloidin, which prevents actin disassembly. (B) Normalized intensity 120 s after photobleaching in phalloidin networks (black) with (closed diamonds) or without (open diamonds) myosin. Recovery is significantly less than in networks without phalloidin (red). (C) Comparison of intensity recovery in photobleached regions of radius ≈22 μm (closed diamonds) or ≈42 μm (open diamonds). There is no statistically significant difference in mean recovery between these cases. (D) Azimuthally averaged intensity, minus its maximum value, as a function of radius from the center of the photobleached region at various times after photobleaching. The dotted black line depicts the profile 120 s after photobleaching. Data in (C, D) are from networks with myosin and no cofilin. Diamonds represent individual samples while bars are averages across all trials.

to faster recovery is consistent with previous results that found severing rate limits turnover in this system [41]. Having found that shortening actin reduces myosin driven turnover, I now ask whether it is due to a decrease in actin buckling.

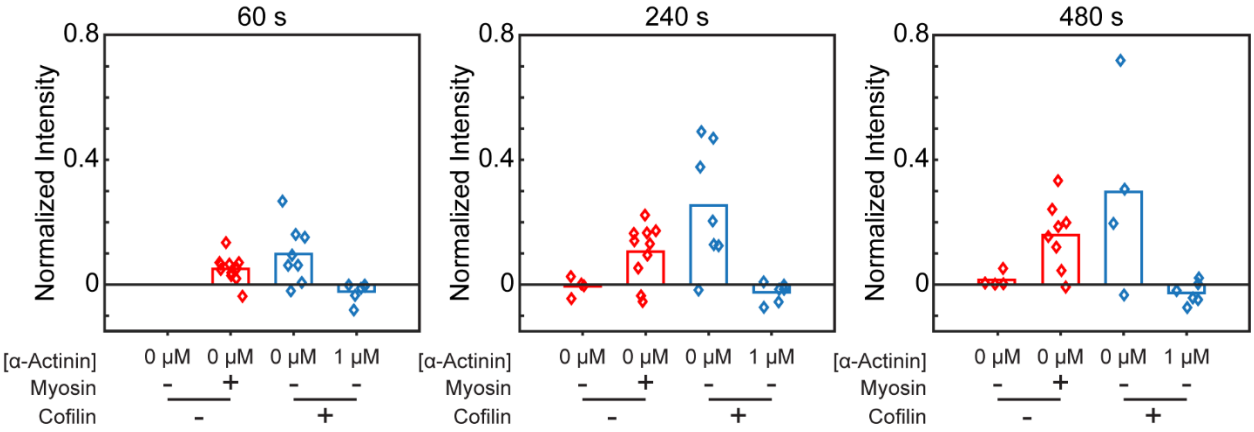

Figure 4.6: Results do not depend on time after photobleaching. Normalized intensity 60 s (*left*), 240 s (*center*), or 480 s (*right*) after photobleaching in networks with 0 μM (red) or 1 μM (blue) cofilin. Diamonds represent individual trials, while bars are the mean across all trials.

To directly quantify whether shorter actin is less prone to buckling and severing, I image networks where only 4% of actin filaments are fluorescently labeled, allowing me to visualize their movement as the network contracts. In these networks, I can track individual filaments in these networks to observe their buckling over time (Figure 4.7B). Since myosin is known to sever actin by inducing large curvatures [96], I measure the maximum curvature achieved at any point along the length of a filament. This curvature increases over time as the network contracts, beginning ~500 s after the addition of myosin (Figure 4.7C). Having found that myosin does increase curvature, I compare buckling across different formin concentrations by measuring the maximum curvature achieved at any time. On average, filaments in networks with 0.01 μM mDia1 reached significantly higher curvatures than those in networks with 0.1 μM mDia1 (Figure 4.7D). Higher formin concentration thus decreases actin buckling, leading me to ask if it

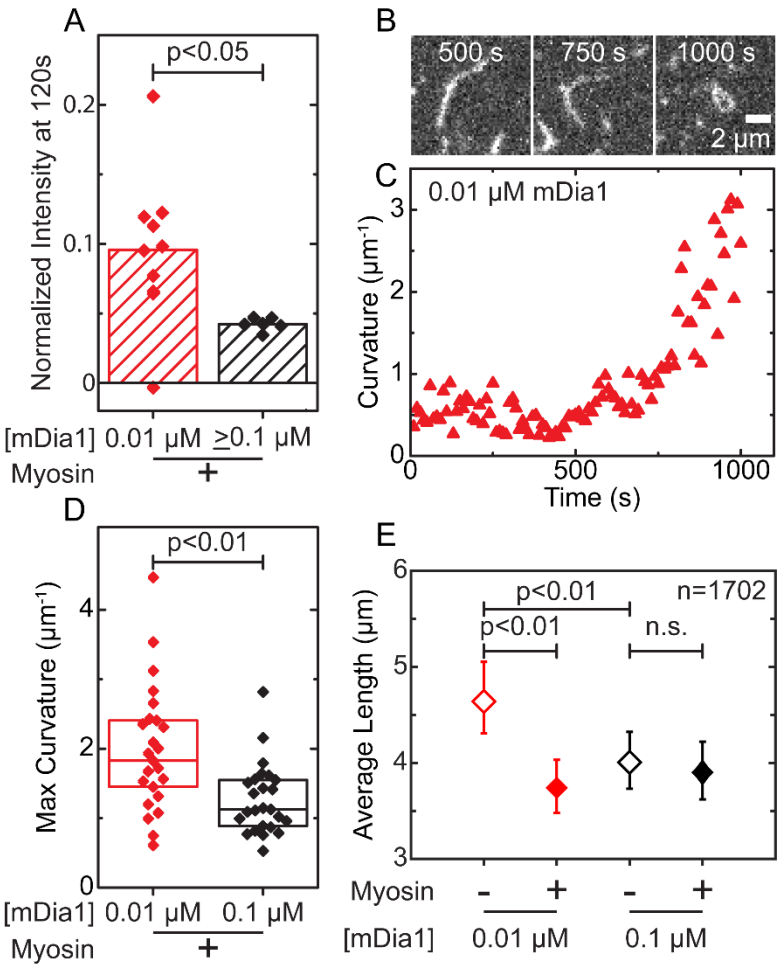

Figure 4.7: Shorter actin reduces myosin driven turnover by decreasing filament buckling and severing. (A) Intensity recovery significantly decreases when average filament length is shortened by increasing the mDia1 concentration from 0.01 μM to ≥0.1 μM. Diamonds represent individual networks while bars are averages across all samples. (B) Images depicting a filament buckling in a sample with 0.01 μM mDia1 after the addition of myosin at time t=0 s. (C) The maximum curvature at each time point for the filament shown in Figure 4.7C. (D) The maximum curvature measured at any time point in networks with 0.01 μM (red) or 0.1 μM (black) mDia1. Diamonds represent individual filaments, while center lines represent the median and boxes represent the 25% to 75% range. (E) The average contour length of actin filaments before (open diamonds) and after (closed diamonds) the start of myosin driven flows and contraction. Data are from networks with 0.01 μM (red) or 0.1 μM (black) mDia1, with each point representing n >400 filaments across 2 independent samples. Error bars depict the 5% to 95% confidence interval measured by bootstrapping.

similarly decreases severing. As a proxy for severing, I measure changes in the contour length of actin with the start of myosin mediated flows. At 0.01 μM of mDia1, average length decreases by

almost a micron, from 4.6 μm to 3.7 μm, with myosin activity (Figure 4.7E). In contrast, when mDia1 concentration is increased to 0.1 μM, myosin does not have a significant impact on average filament length. Myosin therefore decreases actin length, presumably due to severing, at 0.01 μM of mDia1 but not at 0.1 μM. Additionally, when the concentration of mDia1 is increased from 0.01 μM to 0.1 μM, the initial average length decreases from 4.6 μm to 4.0 μm, confirming that filament length is inversely dependent on formin concentration. Decreasing filament length by increasing mDia1 concentration thus decreases buckling and severing of actin filaments. Since shorter actin has both a lower turnover rate and is less prone to severing, I conclude that myosin buckling is responsible for its increase in turnover rate.

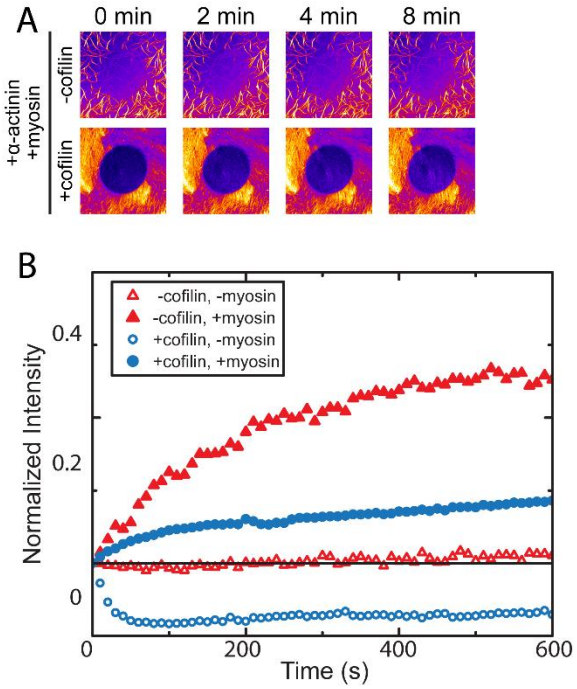

Figure 4.8: Myosin increases turnover rate of actin in α-actinin bundles. (A) Images depicting FRAP in networks with myosin and 1 μM α-actinin. (B) Intensity recovery in networks with α-actinin, with (closed symbols) or without (open symbols) myosin and with (blue circles) or without (red triangles) 1 μM cofilin.

4.4.4 Myosin Increases Turnover in Bundled Filaments

Having found that myosin can enhance actin turnover, I return to α-actinin cross-linked networks to see if this form of severing is effective in bundled filaments. Using FRAP, I measure turnover in networks with α-actinin and myosin, both with and without cofilin (Figure 4.8A). As observed earlier, without myosin there is no recovery in these networks (Figure 4.8B, open symbols). The addition of myosin, however, causes the intensity to recover over time (Figure 4.8B, closed symbols). Myosin is thus able to sever actin in α-actinin cross-linked, even while cofilin cannot.

4.5 Conclusions

Altogether, I find two strategies for severing actin to enhance turnover, the efficiencies of which depend on the presence of cross-linkers. Cofilin mediated turnover is prevented by α-actinin, although this cross-linker does not prevent cofilin from binding to actin. Instead, bundled filaments might have fewer thermal fluctuations which are essential for cofilin severing [48]. These results contrast studies where short, rigid cross-linking increased the rate at which cofilin severed actin by constraining twist [25,101]. One difference is that α-actinin, which is ~7 times the length of fascin [61,62], is longer than previously used cross-linkers, and therefore might constrain filaments less and generate less torsional stress. Future work could explore the effect of other cross-linkers on cofilin activity and test whether bundling with different long cross-linkers has a similar effect as with α-actinin. Alternatively, noncross-linker methods of bundling actin, such as by using a high concentration of crowding agent, could dampen thermal fluctuations without constraining twist.

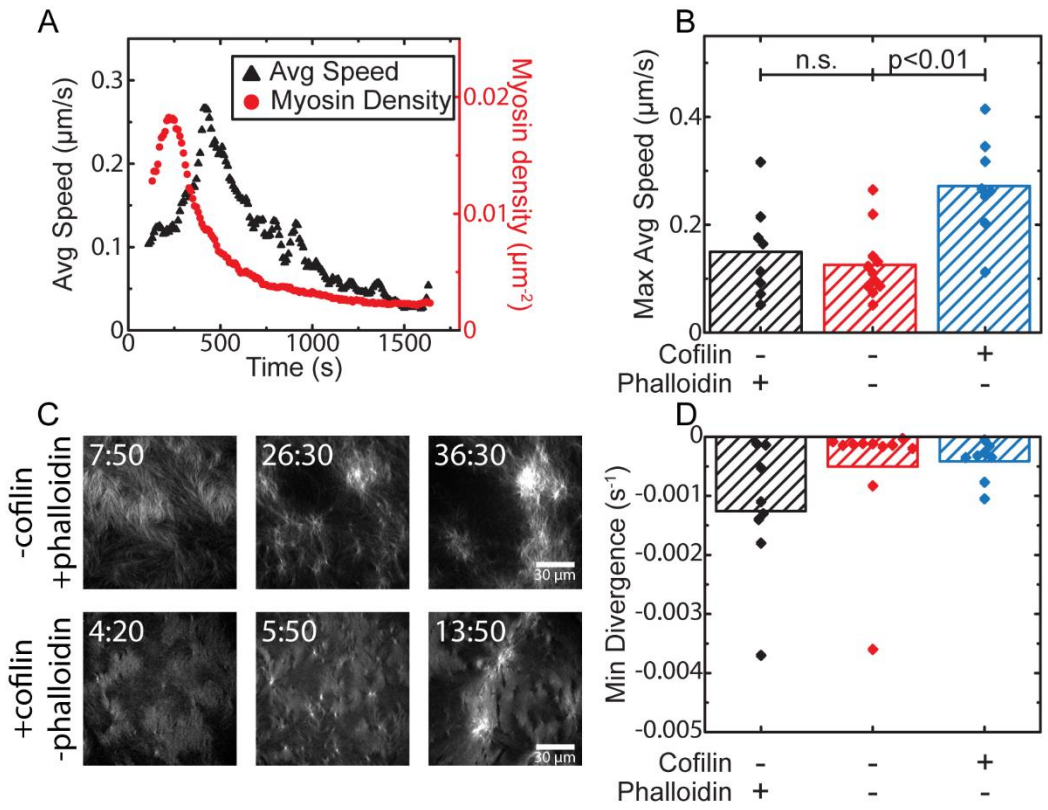

Figure 4.9: Turnover makes myosin induced flows faster but less contractile. (A) The speed of myosin induced flows (black triangles), averaged over an entire field of view, initially increases then decays as myosin (red circles) first gathers then clusters. (B) Cofilin (blue) significantly increases the maximum speed at any time compared to networks with no cofilin (red) or with phalloidin (black). (C) Images depicting actin flows after myosin is added at time $t = 0$. Networks with phalloidin (*top*) eventually contract into asters, while networks with cofilin (*bottom*) do not. (D) Minimum divergence achieved at any time in networks with phalloidin (black), no phalloidin or cofilin (red), or with cofilin (blue). Actin networks with cofilin are less contractile than networks those with phalloidin. Diamonds represent individual samples while bars are averages across all trials.

I also find that myosin induced severing is similarly able to increase the rate of turnover. In contrast to cofilin mediated turnover, however, this increase persisted even when actin was bundled with α-actinin suggesting myosin can still generate sufficient forces between bundled actin to sever filaments. Since α-actinin forms apolar bundles, myosin can still exert force between two filaments in a bundle even if they are not moving relative to each other.

One interesting follow up would therefore be to measure myosin-mediated turnover in polar bundles, where motors might not be able to build up the same amount of force. Future work could also investigate the reverse question of how turnover influences myosin forces and flows. Turnover has been found to relax stresses and fluidize actin networks [41], which might prevent myosin from building up long range forces, while more fluid networks might be more susceptible to flow. In fact, I observe that cofilin led to faster but less contractile flows. After the addition of motors, network speed averaged over a field of view increases as myosin deposits, then decreases when myosin density decreases as the motors cluster (Figure 4.9A). To measure speed, I take the maximum speed achieved at any time. Compared to networks with phalloidin, the presence of cofilin significantly increases the maximum average speed (Figure 4.9B). However, turnover also prevents the contraction of actin into asters by making flows less contractile overall, as measured by the minimum divergence measured at any time (Figure 4.9C, D). While these results show turnover does have an impact on myosin induced flows, additional research could further investigate this question and measure the effect of turnover on myosin stresses and activity.

These results suggest that different methods of severing therefore are not only viable to accelerate turnover, but also might be necessary depending on local actin architecture. Cells could use different strategies to disassemble actin at various locations throughout their interior depending on which cross-linkers are present. One relevant example is during cytokinesis, where cells form an actomyosin contractile ring which additionally contains both cofilin and α-actinin [167]. The function of this ring also depends on dynamic actin [168], so changes in cross-linkers that disrupt actin disassembly could impact its function. In fact, previous research has found that overexpressing α-actinin during cytokinesis disrupts actin turnover, leading to failure [169].

Understanding the effects of cross-linkers on various methods of disassembling actin could inform how cells regulate turnover.

CHAPTER 5

CONCLUSION

5.1 Summary

In this work, I investigate the connection between structure, mechanics, and dynamics in reconstituted actin. Chapters 2 and 3 focus on the interplay between structure and mechanical properties. Chapter 2 describes how actin changes the internal structure of phase separated droplets. Adding short actin filaments creates nematic order in otherwise anisotropic FUS droplets. Furthermore, the shape and physical properties of these droplets are tunable by changing actin concentration and length. As droplet size increases or shorter actin is used, the droplets become less elongated and transition from tactoids to ellipsoids to spheres. These droplets are well-described by a bipolar tactoid model, which explains how internal structure defines material properties, leading to the observed shapes.

In Chapter 3, I discuss how networks can adapt their rheological properties to external stimuli through structural changes. Cross-linked networks develop mechanical hysteresis in response to a training stress, causing the network to reversibly stiffen in the direction of training. Such a response is non-monotonic with cross-linker concentration, leading to an ideal concentration for maximized hysteresis. By changing cross-linker properties in experimental and simulated networks, I find that hysteresis requires both nonlinearity where networks strain stiffen and constituent filaments that can align under stress.

Finally, in Chapter 4 I investigate how cross-linkers and myosin regulate actin turnover dynamics. I find that bundling actin with α-actinin prevents cofilin mediated severing and

turnover. Additionally, adding myosin enhances turnover even in networks without cofilin. In these systems, myosin induced buckling instead severs filaments. Remarkably, myosin can increase turnover in actin cross-linked with α-actinin. These results suggest different methods of turnover might be necessary in cells depending on local architecture.

These results inform on both the working of cells and the manufacturing of new biologically inspired materials. Chapter 2 reveals a mechanism through which cells could organize filamentous proteins, as well as a method of constructing and tuning the structure of artificial droplets. The hysteresis explored in Chapter 3 provides a general technique for constructing materials capable of passively adapting to external stress, as none of the necessary conditions are exclusive to actin. Additionally, while it is unlikely that cells utilize this exact method to respond to external stimuli, this research reveals how even slight nematic ordering impacts the rheology of actin networks and therefore could be relevant to their properties in cells. Finally, the work in Chapter 4 explicitly informs on cellular processes, specifically on turnover which is essential for cellular viability, and is thus directly applicable to cells. Furthermore, while artificial materials cannot currently imitate the complexity of turnover, learning how cells regulate these dynamics informs on how to recreate them for potential materials in the future.

5.2 Future Work

In addition to informing on cell mechanics and the creation of new materials, this work raises several open questions and provides interesting directions for future research. While some of these questions are discussed in their respective chapters, here I highlight a few of particular interest.

One promising area is further investigating how turnover influences myosin forces and flows. Like myosin, turnover is an active process, albeit one that relaxes instead of imparts stresses. Turnover in actomyosin networks therefore presents a model system to study the interplay of multiple active processes. In Chapter 4, I found that cofilin lead to faster but less contractile flows. Additional analysis could further inform on these networks. Recently, many methods of analysis have been developed to better understand active processes. One example is measuring the degree to which detailed balance is broken. Equilibrium systems must respect detailed balance, meaning there can be no net flux in probability phase space. Active processes, on the other hand, can violate detailed balance, and measuring the resulting flux informs on how energy is dissipated in the system [170–172]. Theoretical work has shown that such analysis applied to bending modes of actin reveals the length scales at which myosin activity injects energy into the system [170], and broken detailed balance has recently been used to measure energy dissipation at various stages of contraction in sparsely labeled actomyosin networks similar to the ones created in Section 4.4.3 [171]. Such methodology could be applied to networks with cofilin to investigate how turnover impacts active myosin forces. Differential dynamic microscopy, which measures the rate at which density fluctuations decay to inform on flows, is a technique that has been used to study active actin-microtubule networks [173,174] and could be similarly applied to actomyosin networks with enhanced turnover. One issue with these methods is that the necessary statistics require an abundance of data. However, in the described reconstituted networks, myosin relatively quickly forms asters, limiting the time period over which data can be collected. These time periods could be extended by forming actin networks in extract from *Xenopus laevis* eggs, which contain the necessary components to enhance turnover and have been found to

permit long lasting myosin flows [175]. The effect on myosin activity could be measured by comparison with networks where turnover is prevented through the addition of phalloidin.

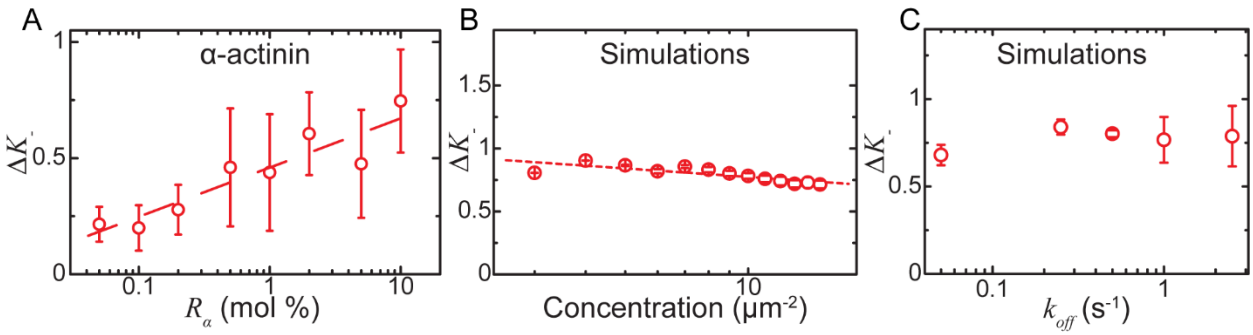

Figure 5.1: Hysteresis at negative strains. ΔK_- increases with cross-linker concentration in (A) experimental networks but is relatively constant in (B) simulated networks. (C) ΔK_- is independent of cross-linker binding/ unbinding rate in simulations. In simulated networks, ΔK_- similarly has no dependence on cross-linker length or stiffness. Bars are standard deviation over at least 2 independent samples. Dotted lines are fits to guide the eyes.

Future work could also probe hysteresis at negative strains. As mentioned in Chapter 3, training can increase differential modulus K when $\gamma > 0$, and it can decrease K when $\gamma < 0$. However, my previous analysis focused purely on the increase at positive strains, leaving the effect of training at $\gamma < 0$ as an open question. This omission is due to discrepancies between experiments and simulations at these strains. Softening at negative strains is measured by defining ΔK_- as

$$\Delta K_- = \frac{K_{Untrained} - K_{Trained}}{K_{Untrained}} \qquad 5.1$$

at $\gamma = -0.8 * \gamma_{max}$. Note two differences between ΔK_- and ΔK_+ as defined in Equation 5.1. First ΔK_- measures the effect of training at $\gamma < 0$. Second, ΔK_- is defined as the negative of ΔK_+ so both values are positive under the corresponding hysteresis response. In experimental networks, ΔK_- increases with cross-linker concentration (Figure 5.1). In contrast, ΔK_- is independent of both cross-linker concentration and physical properties in simulations. The cause

of this discrepancy is unknown. Understanding the aspects of simulations causing ΔK_{-} to be constant would inform on the origin of softening at negative strains and how to tune such a response.

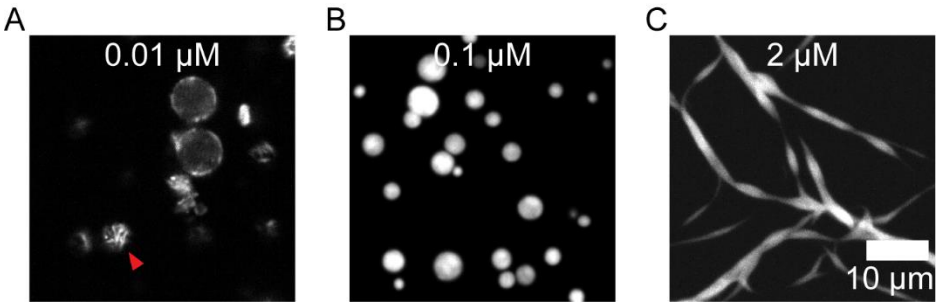

Figure 5.2: FUS composites with long actin. Images of long actin filaments (with no capping protein) partitioned into FUS. (A) At 0.01 μM, actin is primarily at the droplet edges. Red arrow highlights the top of a droplet, where individual bundles are visible. (B) At 0.1 μM of actin, FUS forms composite droplets with actin throughout. (C) At 2 μM, actin is bundled by FUS.

While Chapter 2 focused on composite droplets with short actin, additional research could investigate composite droplets with long filaments. The protein Tau has been found to bundle microtubules [176], suggesting FUS could have a similar effect on long actin. Preliminary results found that long actin composites form a variety of structures depending on actin concentration (Figure 5.2). With no capping protein, FUS still partitions actin into droplets at concentrations of 0.1 μM and below. However, at 0.01 μM filaments are primarily at droplet edges, similar to droplets previously seen when actin partitioned into coaservates [136]**.** On the other hand, at higher concentrations of 2 μM, FUS bundles actin. Understanding the structures FUS forms with long actin would further expand the possibilities for creation of droplets with desired properties and inform on the ability of cells to form structures of filamentous proteins via phase separation.

Overall, this work investigates the interplay of structure, dynamics, and mechanics in three experimental systems. This research both informs on these systems and reveals open questions requiring further study. Of particular interest are questions about the influence of turnover on

myosin activity, hysteresis at $\gamma < 0$, and composites formed with FUS and long actin filaments. Future work into these any of these areas would inform on both cellular mechanics and the creation of novel materials.

APPENDIX A

STANDARD MATERIALS AND METHODS

A.1. Actin Buffer Solutions

Three buffers are used for actin. Actin is stored in calcium buffer-G (CaBG), which has a sufficiently low salt concentration that actin remains in its monomeric state and does not polymerize into filaments. KMEI (also called F-Buffer) has a higher concentration of salt and is used to initialize polymerization. In cells, actin monomers bind Mg^{2+}, while purified actin is stored in a Ca buffer [12]. Magnesium exchange buffer (ME) replaces bound Ca^{2+} ions with Mg^{2+}. For the work described in Chapters 2 and 4, monomers are incubated in ME for 2 min before use. The recipes for all three buffers are as follows:

CaBG: 0.1 mM $CaCl_2$, 2 mM TRIS, 0.2 mM ATP, 0.5 mM DTT, 1 mM NaN_3, pH 8.0

KMEI: 50 mM KCl, 1 mM $MgCl_2$, 0.2 mM EGTA, 10 mM Imidazole, pH 7.0

ME: 50 μM $MgCl_2$, 0.2 mM EGTA

A.2. Protein Purification

After purification, all proteins are flash frozen in liquid nitrogen and stored at -80 $^{\circ}$C until use. After thawing, proteins are kept at 0-4 $^{\circ}$C.

A.2.1. Actin

Monomeric actin (G-actin) is purified from rabbit skeletal muscle acetone powder (Pel Freeze Biologicals, Product code: 41008-3) using a procedure adapted from [177]. Acetone powder is mixed into CaBG. The resulting solution is centrifuged at 20,000 g for 30 min after which the supernatant is filtered through glass wool. This centrifuging and filtering is repeated.

Next, the salt concentration is increased first to 50 mM KCl and 2 mM $MgCl_2$ to polymerize actin, then to 0.8 M KCl to dissociate tropomyosin. The solution is spun at 90,000 g for 1.5-2 hours to sediment filaments, after which the pellet is resuspended in CaBG and dounced. For unlabeled actin, the resuspended pellet is dialyzed in CaBG overnight then again centrifuged at 90,000 g for 1.5-2 hrs. The supernatant is then run over an S300 sizing column.

Actin is labeled using tetramethylrhodamine-6-maleimide (TMR) dye (Life Technologies). For labeled actin (TMR-actin), after douncing the resuspended pellet is dialyzed in CaBG without DTT for at least 2 hours, but up to 3 days. TMR is dissolved in dimethylformamide and added dropwise to actin over the course of ~1 hr. The reaction is allowed to proceed for 16-20 hrs, after which the solution is centrifuged at 100,000 g for 2 hrs and concentrated to ~10 mL using an Amicon Ultra Spin Concentrator (MilliporeSigma). The solution is then dialyzed overnight in CaBG then run over a DAEA column (HiTrap) using FPLC. Finally, TMR-actin is dialyzed overnight in KMEI and run over an S300 sizing column.

After purification, both dark and labeled actin is stored in CaBG. After thawing, TMR-actin is centrifuged at 259,000 g for 30 min with the supernatant being retained to remove clumps.

A.2.2. ddFLN and α-actinin

Dictyostelium discoideum filamin (ddFLN) and α-actinin are each expressed in E. coli BL21-Codon Plus(DE3)-RP cells and purified using a HIS tag as described in [178]. Protein expression is triggered using IPTG, after which cells are incubated at 16 $^{\circ}$C overnight. Sonication is used to rupture cells. Talon affinity resin binds the HIS tag, after which proteins are eluted with a buffer composed of 50 mM NaH_2PO_4, 500 mM NaCl, 10 vol% glycerol, 250 mM Imidazole, 10 mM β-mercaptoethanol, pH 8.0. Finally, FPLC is performed with a Q HP column (HiTrap). ddFLN is stored in FLN storage buffer (10 mM Tris-HCl, 50 mM KCl, 1 mM EGTA, 1 mM $MgCl_2$, 1 mM

DTT, pH 7.4). α-actinin is stored in a buffer composed of 20 mM Tris-HCl, 10 vol% glycerol, 100 mM NaCl, 0.2 mM EDTA, 0.01 wt% NaN_3, 1 mM DTT, pH 8.0.

A.2.3. Human FLN

Human filamin (FLN) is expressed in insect Sf9 cells using Baculovirus and purified using a FLAG tag. Virus is prepared by transforming 1 ng/μL of FLN DNA into DH10Bac cells. Sf9 cells are grown to 2×10^6 cells/mL then split, a process that is repeated at least once more. 12.5 mL of Baculovirus is next added to 1 L of Sf9 cells at a density of 2×10^6 cells/mL. Cells are incubated for 48 hrs at 27°C while shaking then harvested by spinning at 4000 g for 20 min at 4°C. The pellet is resuspended in 50 mL of buffer composed of 10 mM Tris-HCl, 100 mM NaCl, 1 vol% Triton X-100, 10 mM EGTA, 1 mM EDTA, 5 mM β-mercaptoethanol, 10 μg/mL chymostatin, 10 μg/mL leupeptin, 10 μg/mL pepstatin, 10 μg/mL PMSF, pH 8.5. Solution is dounced then sonicated to break open cells, then centrifuged at 3000 g for 10 min. 0.5 mL of anti-FLAG resin is added to the supernatant, which is then incubated for 30 min while shaking at 4°C. The solution is then centrifuged at 3000 g for 10 min and the pellet is resuspended in AB wash buffer (150 mM KCl, 20 mM Imidazole, 5 mM $MgCl_2$, 1 mM PMSF, 1 mM DTT, 1 mM EDTA, 1 mM EGTA, 3 mM ATP, 10 μg/mL Aprotinin, 10 μg/mL Leupeptin, pH 7.5). The resuspended pellet is then applied to a Pierce column and rinsed three times with AB wash buffer. FLN is then eluted using AB wash buffer plus 0.2 mg/mL FLAG peptide. Protein is dialyzed overnight and stored in FLN storage buffer (see Section A.2.2).

A.2.4. mDia1

mDia1 is expressed in E. coli BL21-Codon Plus(DE3)-RP cells and purified using a SNAP tag as described in [178]. Protein expression is triggered using IPTG, after which cells are incubated at 16 $^{\circ}$C overnight. Sonication is used to rupture cells. Talon affinity resin is used to

bind the SNAP tag, after which proteins are eluted with a buffer composed of 50 mM NaH_2PO_4, 500 mM NaCl, 10 vol% glycerol, 250 mM Imidazole, 10 mM β-mercaptoethanol, pH 8.0. mDia1 is stored in a buffer composed of 20 mM HEPES, 100 mM KCl, 0.01 wt% NaN_3, 10 vol% glycerol, 1 mM DTT, pH 7.4.

A.3. Microscopy Reagents

A.3.1. Oil-surfactant Coating

2 wt% of the surfactant PFPE-PEG-PFPE (008; RAN Biotechnologies) is first dissolved in Novec-7500 Engineered Fluid (3M). The oil-surfactant solution is sonicated for 30 min in a bath sonicator, filtered through a 0.2 μm pore sized membrane (6784-1302; GE Healthcare), then flushed with nitrogen gas and stored at 4°C until use. Immediately prior to adding the sample, 4 μL of oil-surfactant solution is added to the sample chamber to create a thin layer of oil-surfactant at the coverslip. After coating the coverslip, excess solution is removed. Each time its container is opened, the oil-surfactant is again flushed with nitrogen gas.

A.3.2. Silane Treated Coverslips

Coverslips are first cleaned by sonicating in ethanol, then immersed in 2 vol% triethoxy(octyl)silane (440213; Sigma-Aldrich) in isopropanol for 10 min and submerged 24 times in water to rinse to form a silane layer. The water is replaced every 6 repetitions. Coverslips are dried overnight at 30°C, although other methods of drying were not found to affect performance. For Chapter 4, a roughly 4x4 cm Teflon square is placed in the center of the coverslip which was then exposed to UV/ozone for 10 min before use. This process removes the silane from any area uncovered by Teflon. As a result, the oil-surfactant only sticks to the center of the chamber, which decreases bulk flows in space-spanning networks.

A.3.3. Cylindrical Chambers

Imaging chambers are composed of a glass cylinder glued to a silane treated coverslip using 5 minute epoxy (Devcon). The epoxy is allowed to dry for at least 6 minutes, then the oil-surfactant and sample are added. A second, non-silane treated coverslip is placed on top of the chamber to reduce evaporation.

BIBLIOGRAPHY

[1] K. E. Kasza, A. C. Rowat, J. Liu, T. E. Angelini, C. P. Brangwynne, G. H. Koenderink and D. A. Weitz, "The cell as a material" *Curr. Opin. Cell Biol.*, 2007, **19**, 101–107.

[2] E. Fischer-Friedrich, Y. Toyoda, C. J. Cattin, D. J. Müller, A. A. Hyman and F. Jülicher, "Rheology of the Active Cell Cortex in Mitosis" *Biophys. J.*, 2016, **111**, 589–600.

[3] N. Schierbaum, J. Rheinlaender and T. E. Schäffer, "Combined atomic force microscopy (AFM) and traction force microscopy (TFM) reveals a correlation between viscoelastic material properties and contractile prestress of living cells" *Soft Matter*, 2019, **15**, 1721–1729.

[4] A. Mongera, P. Rowghanian, H. J. Gustafson, E. Shelton, D. A. Kealhofer, E. K. Carn, F. Serwane, A. A. Lucio, J. Giammona and O. Campàs, "A fluid-to-solid jamming transition underlies vertebrate body axis elongation" *Nature*, 2018, **561**, 401–405.

[5] T. Lecuit, P.-F. Lenne and E. Munro, "Force Generation, Transmission, and Integration during Cell and Tissue Morphogenesis" *Annu. Rev. Cell Dev. Biol*, 2011, **27**, 157–184.

[6] K. E. Cavanaugh, M. F. Staddon, E. Munro, S. Banerjee and M. L. Gardel, "RhoA Mediates Epithelial Cell Shape Changes via Mechanosensitive Endocytosis" *Dev. Cell*, 2020, **52**, 152-166.e5.

[7] C. P. Heisenberg and Y. Bellaïche, "Forces in tissue morphogenesis and patterning" *Cell*, 2013, 153, 948–962.

[8] W. M. Bement, P. Forscher and M. S. Mooseker, "A novel cytoskeletal structure involved in purse string wound closure and cell polarity maintenance" *J. Cell Biol.*, 1993, **121**, 565–578.

[9] V. Ajeti, A. P. Tabatabai, A. J. Fleszar, M. F. Staddon, D. S. Seara, C. Suarez, M. S. Yousafzai, D. Bi, D. R. Kovar, S. Banerjee and M. P. Murrell, "Wound healing coordinates actin architectures to regulate mechanical work" *Nat. Phys.*, 2019, **15**, 696–705.

[10] A. Nusrat, C. Delp and J. L. Madara, "Intestinal epithelial restitution characterization of a cell culture model and mapping of cytoskeletal elements in migrating cells" *J. Clin. Invest.*, 1992, **89**, 1501–1511.

[11] P. W. Gunning, U. Ghoshdastider, S. Whitaker, D. Popp and R. C. Robinson, "The evolution of compositionally and functionally distinct actin filaments" *J. Cell Sci.*, 2015, **128**, 2009–2019.

[12] T. D. Pollard, "Actin and actin-binding proteins" *Cold Spring Harb. Perspect. Biol.*, 2016, **8**, 1–17.

[13] A. Diz-Muñoz, O. D. Weiner and D. A. Fletcher, "In pursuit of the mechanics that shape cell surfaces" *Nat. Phys.*, 2018, **14**, 648–652.

[14] J. Mueller, G. Szep, M. Nemethova, I. de Vries, A. D. Lieber, C. Winkler, K. Kruse, J. V. Small, C. Schmeiser, K. Keren, R. Hauschild and M. Sixt, "Load Adaptation of Lamellipodial Actin Networks" *Cell*, 2017, **171**, 188-200.e16.

[15] S. Banerjee, M. L. Gardel and U. S. Schwarz, "The Actin Cytoskeleton as an Active Adaptive Material" *Annu. Rev. Condens. Matter Phys. 2020*, 2020, **11**, 421–439.

[16] M. Mokbel, K. Hosseini, S. Aland and E. Fischer-Friedrich, "The Poisson Ratio of the Cellular Actin Cortex Is Frequency Dependent" *Biophys. J.*, 2020, **118**, 1968–1976.

[17] W. Pomp, K. Schakenraad, H. E. Balcıoğlu, H. van Hoorn, E. H. J. Danen, R. M. H. Merks, T. Schmidt and L. Giomi, "Cytoskeletal Anisotropy Controls Geometry and Forces of Adherent Cells" *Phys. Rev. Lett.*, 2018, **121**, 178101.

[18] L. Blanchoin, R. Boujemaa-Paterski, C. Sykes and J. Plastino, "Actin Dynamics, Architecture, and Mechanics in Cell Motility" *Physiol. Rev.*, 2014, **94**, 235–263.

[19] A. Akhmanova and J. A. Hammer, "Linking molecular motors to membrane cargo" *Curr. Opin. Cell Biol.*, 2010, 22, 479–487.

[20] L. Yolland, M. Burki, S. Marcotti, A. Luchici, F. N. Kenny, J. R. Davis, E. Serna-Morales, J. Müller, M. Sixt, A. Davidson, W. Wood, L. J. Schumacher, R. G. Endres, M. Miodownik and B. M. Stramer, "Persistent and polarized global actin flow is essential for directionality during cell migration" *Nat. Cell Biol.*, 2019, **21**, 1370–1381.

[21] B. Bugyi and M. F. Carlier, "Control of actin filament treadmilling in cell motility" *Annu. Rev. Biophys.*, 2010, 39, 449–470.

[22] R. Dominguez and K. C. Holmes, "Actin structure and function" *Annu. Rev. Biophys.*, 2011, **40**, 169–186.

[23] E. M. De La Cruz and M. L. Gardel, "Actin mechanics and fragmentation" *J. Biol. Chem.*, 2015, **290**, 17137–17144.

[24] E. Prochniewicz, N. Janson, D. D. Thomas and E. M. De La Cruz, "Cofilin increases the torsional flexibility and dynamics of actin filaments" *J. Mol. Biol.*, 2005, **353**, 990–1000.

[25] H. Wioland, A. Jegou and G. Romet-Lemonne, "Torsional stress generated by ADF/cofilin on cross-linked actin filaments boosts their severing." *Proc. Natl. Acad. Sci.*, 2019, **116**, 2595–2602.

[26] M. P. Murrell, T. Thoresen and M. L. Gardel, "Reconstitution of contractile actomyosin arrays" *Reconstitution of contractile actomyosin arrays*, Elsevier Inc., 1st edn., 2014, vol. 540.

[27] M. Coué, S. L. Brenner, I. Spector and E. D. Korn, "Inhibition of actin polymerization by latrunculin A" *FEBS Lett.*, 1987, **213**, 316–318.

[28] A. M. Lengsfeld, I. Löw, T. Wieland, P. Dancker and W. Hasselbach, "Interaction of phalloidin with actin" *Proc. Natl. Acad. Sci.*, 1974, **71**, 2803–2807.

[29] C. E. Aitken, R. A. Marshall and J. D. Puglisi, "An oxygen scavenging system for improvement of dye stability in single-molecule fluorescence experiments" *Biophys. J.*, 2008, **94**, 1826–1835.

[30] Y. Harada, K. Sakurada, T. Aoki, D. D. Thomas and T. Yanagida, "Mechanochemical coupling in actomyosin energy transduction studied by in vitro movement assay" *J. Mol. Biol.*, 1990, **216**, 49–68.

[31] I. Sagot, A. A. Rodal, J. Moseley, B. L. Goode and D. Pellman, "An actin nucleation mechanism mediated by Bni1 and profilin" *Nat. Cell Biol.*, 2002, **4**, 626–631.

[32] D. Pruyne, M. Evangelista, C. Yang, E. Bi, S. Zigmond, A. Bretscher and C. Boone, "Role of formins in actin assembly: Nucleation and barbed-end association" *Science*, 2002, **297**, 612–615.

[33] T. D. Pollard and J. A. Cooper, "Quantitative Analysis of the Effect of Acanthamoeba Profilin on Actin Filament Nucleation and Elongation" *Biochemistry*, 1984, **23**, 6631–6641.

[34] D. R. Kovar, E. S. Harris, R. Mahaffy, H. N. Higgs and T. D. Pollard, "Control of the Assembly of ATP- and ADP-Actin by Formins and Profilin" *Cell*, 2006, **124**, 423–435.

[35] C. A. Wilson, M. A. Tsuchida, G. M. Allen, E. L. Barnhart, K. T. Applegate, P. T. Yam, L. Ji, K. Keren, G. Danuser and J. A. Theriot, "Myosin II contributes to cell-scale actin network treadmilling through network disassembly" *Nature*, 2010, **465**, 373–377.

[36] L. Blanchoin and T. D. Pollard, "Hydrolysis of ATP by polymerized actin depends on the bound divalent cation but not profilin" *Biochemistry*, 2002, **41**, 597–602.

[37] M. F. Carlier and D. Pantaloni, "Direct Evidence for ADP-Pi-F-Actin as the Major Intermediate in ATP-Actin Polymerization. Rate of Dissociation of Pi from Actin Filaments" *Biochemistry*, 1986, **25**, 7789–7792.

[38] E. D. Korn, M. F. Carlier and D. Pantaloni, "Actin polymerization and ATP hydrolysis" *Science*, 1987, **238**, 638–644.

[39] N. Selve and A. Wegner, "Rate of Treadmilling of Actin Filaments in Vitro" *Rate of Treadmilling of Actin Filaments in Vitro*, 1986, vol. 187.

[40] D. Drenckhahn and T. D. Pollard, "Elongation of actin filaments is a diffusion-limited reaction at the barbed end and is accelerated by inert macromolecules" *J. Biol. Chem.*,

1986, **261**, 12754–12758.

[41] P. M. McCall, F. C. MacKintosh, D. R. Kovar and M. L. Gardel, "Cofilin drives rapid turnover and fluidization of entangled F-actin" *Proc. Natl. Acad. Sci.*, 2019, **116**, 12629–12637.

[42] K. L. Weirich, S. Banerjee, K. Dasbiswas, T. A. Witten, S. Vaikuntanathan and M. L. Gardel, "Liquid behavior of cross-linked actin bundles" *Proc. Natl. Acad. Sci.*, 2017, **114**, 2131–2136.

[43] C. B. Gurniak, E. Perlas and W. Witke, "The actin depolymerizing factor n-cofilin is essential for neural tube morphogenesis and neural crest cell migration" *Dev. Biol.*, 2005, **278**, 231–241.

[44] K. Moriyama and I. Yahara, "The actin-severing activity of cofilin is exerted by the interplay of three distinct sites on cofilin and essential for cell viability" *Biochem. J.*, 2002, **365**, 147–155.

[45] M. F. Carlier, V. Laurent, J. Santolini, R. Melki, D. Didry, G. X. Xia, Y. Hong, N. H. Chua and D. Pantaloni, "Actin depolymerizing factor (ADF/cofilin) enhances the rate of filament turnover: Implication in actin-based motility" *J. Cell Biol.*, 1997, **136**, 1307–1322.

[46] E. M. De La Cruz, "Cofilin binding to muscle and non-muscle actin filaments: Isoform-dependent cooperative interactions" *J. Mol. Biol.*, 2005, **346**, 557–564.

[47] B. R. Mccullough, L. Blanchoin, J.-L. Martiel, E. M. De and L. Cruz, "Cofilin Increases the Bending Flexibility of Actin Filaments: Implications for Severing and Cell Mechanics" *J Mol. Biol*, 2008, **381**, 550–558.

[48] E. M. De La Cruz, "How cofilin severs an actin filament" *Biophys. Rev.*, 2009, **1**, 51–59.

[49] C. Suarez, J. Roland, R. Boujemaa-Paterski, H. Kang, B. R. McCullough, A.-C. Reymann, C. Guérin, J. L. Martiel, E. M. De La Cruz and L. Blanchoin, "Cofilin tunes the nucleotide state of actin filaments and severs at bare and decorated segment boundaries" *Curr. Biol.*, 2011, **21**, 862–868.

[50] H. Wioland, B. Guichard, Y. Senju, S. Myram, P. Lappalainen, A. Jégou and G. Romet-Lemonne, "ADF/Cofilin Accelerates Actin Dynamics by Severing Filaments and Promoting Their Depolymerization at Both Ends" *Curr. Biol.*, 2017, **27**, 1956–1967.

[51] R. Phillips, J. Kondev, J. A. Theriot and H. G. Garcia, "Beam Theory: Architecture for Cells and Skeletons" in *Physical Biology of the Cell*, Garland Science, New York, Second., 2013, pp. 383–426.

[52] T. T. Falzone, M. Lenz, D. R. Kovar and M. L. Gardel, "Assembly kinetics determine the architecture of α-actinin crosslinked F-actin networks" *Nat. Commun.*, 2012, **3**, 861–869.

[53] K. M. Schmoller, O. Lieleg and A. R. Bausch, "Structural and viscoelastic properties of actin/filamin networks: Cross-linked versus bundled networks" *Biophys. J.*, 2009, **97**, 83–89.

[54] O. Lieleg, M. M. A. E. Claessens and A. R. Bausch, "Structure and dynamics of cross-linked actin networks" *Soft Matter*, 2010, **6**, 218–225.

[55] O. Lieleg, J. Kayser, G. Brambilla, L. Cipelletti and A. R. Bausch, "Slow dynamics and internal stress relaxation in bundled cytoskeletal networks" *Nat. Mater.*, 2011, **10**, 236–242.

[56] T. T. Falzone, P. W. Oakes, J. Sees, D. R. Kovar and M. L. Gardel, "Actin assembly factors regulate the gelation kinetics and architecture of F-actin networks" *Biophys. J.*, 2013, **104**, 1709–1719.

[57] V. Yadav, D. S. Banerjee, A. P. Tabatabai, D. R. Kovar, T. Kim, S. Banerjee and M. P. Murrell, "Filament Nucleation Tunes Mechanical Memory in Active Polymer Networks" *Adv. Funct. Mater.*, 2019, **29**, 1905243.

[58] J. Xu, W. H. Schwarz, J. A. Käs, T. P. Stossel, P. A. Janmey and T. D. Pollard, "Mechanical properties of actin filament networks depend on preparation, polymerization conditions, and storage of actin monomers" *Biophys. J.*, 1998, **74**, 2731–2740.

[59] R. D. Mullins, J. A. Heuser and T. D. Pollard, "The interaction of Arp2/3 complex with actin: Nucleation, high affinity pointed end capping, and formation of branching networks of filaments" *Proc. Natl. Acad. Sci.*, 1998, **95**, 6181–6186.

[60] G. M. Popowicz, M. Schleicher, A. A. Noegel and T. A. Holak, "Filamins: promiscuous organizers of the cytoskeleton" *Trends Biochem. Sci.*, 2006, **31**, 411–419.

[61] S. Jansen, A. Collins, C. Yang, G. Rebowski, T. Svitkina and R. Dominguez, "Mechanism of actin filament bundling by fascin" *J. Biol. Chem.*, 2011, **286**, 30087–30096.

[62] C. M. Hampton, D. W. Taylor and K. A. Taylor, "Novel Structures for α-Actinin:F-Actin Interactions and their Implications for Actin-Membrane Attachment and Tension Sensing in the Cytoskeleton" *J. Mol. Biol.*, 2007, **368**, 92–104.

[63] I. Schwaiger, A. Kardinal, M. Schleicher, A. A. Noegel and M. Rief, "A mechanical unfolding intermediate in an actin-crosslinking protein" *Nat. Struct. Mol. Biol.*, 2004, **11**, 81–85.

[64] J. B. Gorlin, R. Yamin, S. Egan, M. Stewart, T. P. Stossel, D. J. Kwiatkowski and J. H. Hartwig, "Human endothelial actin-binding protein (ABP-280, nonmuscle filamin): A molecular leaf spring" *J. Cell Biol.*, 1990, **111**, 1089–1105.

[65] J. Liu, M. L. Gardel, K. Kroy, E. Frey, B. D. Hoffman, J. C. Crocker, A. R. Bausch and D. A. Weitz, "Microrheology probes length scale dependent rheology" *Phys. Rev. Lett.*, 2006,

96, 118104.

[66] R. G. Larson, "The Structure and Rheology of Complex Fluids" *The Structure and Rheology of Complex Fluids*, Oxford University Press, Oxford, 1999.

[67] O. Lieleg, M. M. A. E. Claessens, C. Heussinger, E. Frey and A. R. Bausch, "Mechanics of bundled semiflexible polymer networks" *Phys. Rev. Lett.*, 2007, **99**, 3–6.

[68] J. H. Shin, M. L. Gardel, L. Mahadevan, P. Matsudaira and D. A. Weitz, "Relating microstructure to rheology of a bundled and cross-linked F-actin network in vitro" *Proc. Natl. Acad. Sci.*, 2004, **101**, 9636–9641.

[69] Y. Tseng, K. M. An, O. Esue and D. Wirtz, "The Bimodal Role of Filamin in Controlling the Architecture and Mechanics of F-actin Networks" *J. Biol. Chem.*, 2004, **279**, 1819–1826.

[70] C. P. Broedersz, M. Depken, N. Y. Yao, M. R. Pollak, D. A. Weitz and F. C. MacKintosh, "Cross-link-governed dynamics of biopolymer networks" *Phys. Rev. Lett.*, 2010, **105**, 1–4.

[71] K. E. Kasza, C. P. Broedersz, G. H. Koenderink, Y. C. Lin, W. Messner, E. A. Millman, F. Nakamura, T. P. Stossel, F. C. MacKintosh and D. A. Weitz, "Actin filament length tunes elasticity of flexibly cross-linked actin networks" *Biophys. J.*, 2010, **99**, 1091–1100.

[72] M. L. Gardel, J. H. Shin, F. C. Mackintosh, L. Mahadevan, P. Matsudaira and D. A. Weitz, "Elastic Behavior of Cross-Linked and Bundled Actin Networks" *Science*, 2004, **304**, 1301–1306.

[73] D. L. Blair, A. R. Bausch, K. M. Schmoller, R. C. Arevalo and P. Fernández, "Cyclic hardening in bundled actin networks" *Nat. Commun.*, 2010, **1**, 134.

[74] S. Majumdar, L. C. Foucard, A. J. Levine and M. L. Gardel, "Mechanical hysteresis in actin networks" *Soft Matter*, 2018, **14**, 2052–2058.

[75] L. C. Foucard, J. K. Price, W. S. Klug and A. J. Levine, "Cooperative buckling and the nonlinear mechanics of nematic semiflexible networks" *Nonlinearity*, 2015, **28**, R89–R112.

[76] J. Xu, J. F. Casella and T. D. Pollard, "Effect of capping protein, CapZ, on the length of actin filaments and mechanical properties of actin filament networks" *Cell Motil. Cytoskeleton*, 1999, **42**, 73–81.

[77] R. Zhang, N. Kumar, J. L. Ross, M. L. Gardel and J. J. De Pablo, "Interplay of structure, elasticity, and dynamics in actin-based nematic materials" *Proc. Natl. Acad. Sci.*, 2017, **115**, E124–E133.

[78] N. Kumar, R. Zhang, J. J. de Pablo and M. L. Gardel, "Tunable structure and dynamics of active liquid crystals" *Sci. Adv.*, 2018, **4**, eaat7779.

[79] P. G. de Gennes and J. Prost, "The physics of liquid crystals" *The physics of liquid crystals*, Oxford University Press, Oxford, 1995.

[80] T. Odijk, "Elastic constants of nematic solutions of rod-like and semi-flexible polymers" *Liq. Cryst.*, 1986, **1**, 553–559.

[81] J. P. Straley, "Frank Elastic Constants of the Hard-Rod Liquid Crystal" *Phys. Rev. A*, 1973, **8**, 2181–2183.

[82] S. J. DeCamp, G. S. Redner, A. Baskaran, M. F. Hagan and Z. Dogic, "Orientational order of motile defects in active nematics" *Nat. Mater.*, 2015, **14**, 1110–1115.

[83] M. Bagnani, G. Nyström, C. De Michele and R. Mezzenga, "Amyloid Fibrils Length Controls Shape and Structure of Nematic and Cholesteric Tactoids" *ACS Nano*, 2019, **13**, 591–600.

[84] M. M. Giraud-Guille, G. Mosser and E. Belamie, "Liquid crystallinity in collagen systems in vitro and in vivo" *Curr. Opin. Colloid Interface Sci.*, 2008, 13, 303–313.

[85] J. E. Kirkwood and G. G. Fuller, "Liquid crystalline collagen: A self-assembled morphology for the orientation of mammalian cells" *Langmuir*, 2009, **25**, 3200–3206.

[86] Z. Dogic and S. Fraden, "Cholesteric phase in virus suspensions" *Langmuir*, 2000, **16**, 7820–7824.

[87] P. Prinsen and P. van der Schoot, "Shape and director-field transformation of tactoids" *Phys. Rev. E*, 2003, **68**, 11.

[88] A. Modlinska, A. M. Alsayed and T. Gibaud, "Condensation and dissolution of nematic droplets in dispersions of colloidal rods with thermo-sensitive depletants" *Sci. Rep.*, 2015, **5**, 1–10.

[89] Y. Trukhina, S. Jungblut, P. Van Der Schoot and T. Schilling, "Osmotic compression of droplets of hard rods: A computer simulation study" *J. Chem. Phys.*, 2009, **130**, 164513.

[90] V. Jamali, N. Behabtu, B. Senyuk, J. A. Lee, I. I. Smalyukh, P. van der Schoot and M. Pasquali, "Experimental realization of crossover in shape and director field of nematic tactoids" *Phys. Rev. E*, 2015, **91**, 042507.

[91] P. W. Oakes, J. Viamontes and J. X. Tang, "Growth of tactoidal droplets during the first-order isotropic to nematic phase transition of F-actin" *Phys. Rev. E*, 2007, **75**, 061902.

[92] D. V. Trivedi, S. Nag, A. Spudich, K. M. Ruppel and J. A. Spudich, "The Myosin Family of Mechanoenzymes: From Mechanisms to Therapeutic Approaches" *Annu. Rev. Biochem.*, 2020, 89, 667–693.

[93] K. Dasbiswas, S. Hu, F. Schnorrer, S. A. Safran and A. D. Bershadsky, "Ordering of

myosin II filaments driven by mechanical forces: Experiments and theory" *Philos. Trans. R. Soc. B Biol. Sci.*, 2018, 373.

[94] B. Alberts, A. Johnson, J. Lewis, D. Morgan, M. Raff, K. Roberts and P. Walter, "The Cytoskeleton" in *Molecular Biology of the Cell*, Garland Science, New York, Sixth., 2015, pp. 889–962.

[95] M. A. Hartman and J. A. Spudich, "The myosin superfamily at a glance" *J. Cell Sci.*, 2012, 125, 1627–1632.

[96] M. P. Murrell and M. L. Gardel, "F-actin buckling coordinates contractility and severing in a biomimetic actomyosin cortex" *Proc. Natl. Acad. Sci.*, 2012, **109**, 20820–20825.

[97] S. Stam, S. L. Freedman, S. Banerjee, K. L. Weirich, A. R. Dinner and M. L. Gardel, "Filament rigidity and connectivity tune the deformation modes of active biopolymer networks" *Proc. Natl. Acad. Sci.*, 2017, **114**, E10037–E10045.

[98] A.-C. Reymann, R. Boujemaa-Paterski, J.-L. Martiel, C. Guérin, W. Cao, H. F. Chin, E. M. De La Cruz, M. Théry and L. Blanchoin, "Actin network architecture can determine myosin motor activity." *Science*, 2012, **336**, 1310–4.

[99] L. Farhadi, S. N. Ricketts, M. J. Rust, M. Das, R. M. Robertson-Anderson and J. L. Ross, "Actin and microtubule crosslinkers tune mobility and control co-localization in a composite cytoskeletal network" *Soft Matter*, 2020, **16**, 7191–7201.

[100] L. Gressin, A. Guillotin, C. Guérin, L. Blanchoin and A. Michelot, "Architecture Dependence of Actin Filament Network Disassembly" *Curr. Biol.*, 2015, **25**, 1437–1447.

[101] D. Breitsprecher, S. A. Koestler, I. Chizhov, M. Nemethova, J. Mueller, B. L. Goode, J. V. Small, K. Rottner and J. Faix, "Cofilin cooperates with fascin to disassemble filopodial actin filaments" *J. Cell Sci.*, 2011, **124**, 3305–3318.

[102] M. Guha, M. Zhou and Y. L. Wang, "Cortical actin turnover during cytokinesis requires myosin II" *Curr. Biol.*, 2005, **15**, 732–736.

[103] K. Murthy and P. Wadsworth, "Myosin-II-dependent localization and dynamics of F-actin during cytokinesis" *Curr. Biol.*, 2005, **15**, 724–731.

[104] N. A. Medeiros, D. T. Burnette and P. Forscher, "Myosin II functions in actin-bundle turnover in neuronal growth cones" *Nat. Cell Biol.*, 2006, **8**, 215–226.

[105] L. Haviv, D. Gillo, F. Backouche and A. Bernheim-Groswasser, "A Cytoskeletal Demolition Worker: Myosin II Acts as an Actin Depolymerization Agent" *J. Mol. Biol.*, 2008, **375**, 325–330.

[106] S. K. Vogel, Z. Petrasek, F. Heinemann and P. Schwille, "Myosin motors fragment and compact membrane-bound actin filaments" *Elife*, 2013, **2**, e00116.

[107] Sonal, K. A. Ganzinger, S. K. Vogel, J. Mücksch, P. Blumhardt and P. Schwille, "Myosin-II activity generates a dynamic steady state with continuous actin turnover in a minimal actin cortex" *J. Cell Sci.*, 2019, **132**, jcs219899.

[108] S. Arzash, P. M. McCall, J. Feng, M. L. Gardel and F. C. MacKintosh, "Stress relaxation in F-actin solutions by severing" *Soft Matter*, 2019, **15**, 6300–6307.

[109] M. Mak, M. H. Zaman, R. D. Kamm and T. Kim, "Interplay of active processes modulates tension and drives phase transition in self-renewing, motor-driven cytoskeletal networks" *Nat. Commun.*, 2016, **7**, 1–12.

[110] Q. Yu, J. Li, M. P. Murrell and T. Kim, "Balance between Force Generation and Relaxation Leads to Pulsed Contraction of Actomyosin Networks." *Biophys. J.*, 2018, **115**, 2003–2013.

[111] W. M. McFadden, P. M. McCall, M. L. Gardel and E. M. Munro, "Filament turnover tunes both force generation and dissipation to control long-range flows in a model actomyosin cortex." *PLoS Comput. Biol.*, 2017, **13**, e1005811.

[112] J. Roostalu, J. Rickman, C. Thomas, F. Nédélec and T. Surrey, "Determinants of Polar versus Nematic Organization in Networks of Dynamic Microtubules and Mitotic Motors" *Cell*, 2018, **175**, 796-808.e14.

[113] A. Patel, H. O. Lee, L. Jawerth, S. Maharana, M. Jahnel, M. Y. Hein, S. Stoynov, J. Mahamid, S. Saha, T. M. Franzmann, A. Pozniakovski, I. Poser, N. Maghelli, L. A. Royer, M. Weigert, E. W. Myers, S. Grill, D. Drechsel, A. A. Hyman and S. Alberti, "A Liquid-to-Solid Phase Transition of the ALS Protein FUS Accelerated by Disease Mutation" *Cell*, 2015, **162**, 1066–1077.

[114] D. R. Scheff, K. L. Weirich, K. Dasbiswas, A. Patel, S. Vaikuntanathan and M. L. Gardel, "Tuning shape and internal structure of protein droplets via biopolymer filaments" *Soft Matter*, 2020, **16**, 5659–5668.

[115] A. B. Marciel, E. J. Chung, B. K. Brettmann and L. Leon, "Bulk and nanoscale polypeptide based polyelectrolyte complexes" *Adv. Colloid Interface Sci.*, 2017, 239, 187–198.

[116] C. P. Brangwynne, P. Tompa and R. V. Pappu, "Polymer physics of intracellular phase transitions" *Nat. Phys.*, 2015, **11**, 899–904.

[117] T. K. Lytle, L. W. Chang, N. Markiewicz, S. L. Perry and C. E. Sing, "Designing Electrostatic Interactions via Polyelectrolyte Monomer Sequence" *ACS Cent. Sci.*, 2019, **5**, 709–718.

[118] S. F. Banani, A. M. Rice, W. B. Peeples, Y. Lin, S. Jain, R. Parker and M. K. Rosen, "Compositional Control of Phase-Separated Cellular Bodies" *Cell*, 2016, **166**, 651–663.

[119] L. Li, S. Srivastava, M. Andreev, A. B. Marciel, J. J. de Pablo and M. V. Tirrell, "Phase Behavior and Salt Partitioning in Polyelectrolyte Complex Coacervates" *Macromolecules*, 2018, **51**, 2988–2995.

[120] X. Wang, J. Lee, Y. W. Wang and Q. Huang, "Composition and rheological properties of β-lactoglobulin/pectin coacervates: Effects of salt concentration and initial protein/polysaccharide ratio" *Biomacromolecules*, 2007, **8**, 992–997.

[121] D. V. Krogstad, N. A. Lynd, S. H. Choi, J. M. Spruell, C. J. Hawker, E. J. Kramer and M. V. Tirrell, "Effects of polymer and salt concentration on the structure and properties of triblock copolymer coacervate hydrogels" *Macromolecules*, 2013, **46**, 1512–1518.

[122] M. Antonov, M. Mazzawi and P. L. Dubin, "Entering and exiting the protein-polyelectrolyte coacervate phase via nonmonotonic salt dependence of critical conditions" *Biomacromolecules*, 2010, **11**, 51–59.

[123] L. Onsager, "THE EFFECTS OF SHAPE ON THE INTERACTION OF COLLOIDAL PARTICLES" *Ann. N. Y. Acad. Sci.*, 1949, **51**, 627–659.

[124] R. M. W. Van Bijnen, R. H. J. Otten and P. Van Der Schoot, "Texture and shape of two-dimensional domains of nematic liquid crystals" *Phys. Rev. E*, 2012, **86**, 1–12.

[125] G. Nyström, M. Arcari and R. Mezzenga, "Confinement-induced liquid crystalline transitions in amyloid fibril cholesteric tactoids" *Nat. Nanotechnol.*, 2018, **13**, 330–336.

[126] P. X. Wang and M. J. MacLachlan, "Liquid crystalline tactoids: Ordered structure, defective coalescence and evolution in confined geometries" *Philos. Trans. R. Soc. A Math. Phys. Eng. Sci.*, 2018, 376.

[127] J. Brugués and D. Needleman, "Physical basis of spindle self-organization" *Proc. Natl. Acad. Sci.*, 2014, **111**, 18496–18500.

[128] W. Heller, W. Wojtowicz and J. H. L. Watson, "Isothermal and non-isothermal transformations of tactoid-forming particles of tungstic acid" *J. Chem. Phys.*, 1948, 16, 998–999.

[129] S. Palmgren, P. J. Ojala, M. A. Wear, J. A. Cooper and P. Lappalainen, "Interactions with PIP2, ADP-actin monomers, and capping protein regulate the activity and localization of yeast twinfilin." *J. Cell Biol.*, 2001, **155**, 251–60.

[130] R. Oldenbourg, "A new view on polarization microscopy." *Nature*, 1996, **381**, 811–812.

[131] C. A. Schneider, W. S. Rasband and K. W. Eliceiri, "NIH Image to ImageJ: 25 years of image analysis" *Nat. Methods*, 2012, **9**, 671–675.

[132] J. Schindelin, I. Arganda-Carreras, E. Frise, V. Kaynig, M. Longair, T. Pietzsch, S. Preibisch, C. Rueden, S. Saalfeld, B. Schmid, J.-Y. Tinevez, D. J. White, V. Hartenstein,

K. Eliceiri, P. Tomancak and A. Cardona, "Fiji: an open-source platform for biological-image analysis" *Nat. Methods*, 2012, **9**, 676–682.

[133] A. V. Kaznacheev, M. M. Bogdanov and S. A. Taraskin, "The nature of prolate shape of tactoids in lyotropic inorganic liquid crystals" *J. Exp. Theor. Phys.*, 2002, **95**, 57–63.

[134] P. Prinsen and P. Van Der Schoot, "Continuous director-field transformation of nematic tactoids" *Eur. Phys. J. E*, 2004, **13**, 35–41.

[135] R. D. Williams, "Nematic Liquid Crystal Droplets" *Rutherford Applet. Lab. Rep.*, 1985, RAL-85-028.

[136] P. M. McCall, S. Srivastava, S. L. Perry, D. R. Kovar, M. L. Gardel and M. V. Tirrell, "Partitioning and Enhanced Self-Assembly of Actin in Polypeptide Coacervates" *Biophys. J.*, 2018, **114**, 1636–1645.

[137] A. Weeds and S. Maciver, "F-actin capping proteins" *Curr. Opin. Cell Biol.*, 1993, **5**, 63–69.

[138] K. A. Black, D. Priftis, S. L. Perry, J. Yip, W. Y. Byun and M. Tirrell, "Protein encapsulation via polypeptide complex coacervation" *ACS Macro Lett.*, 2014, **3**, 1088–1091.

[139] A. C. Obermeyer, C. E. Mills, X. H. Dong, R. J. Flores and B. D. Olsen, "Complex coacervation of supercharged proteins with polyelectrolytes" *Soft Matter*, 2016, **12**, 3570–3581.

[140] C. W. Pak, M. Kosno, A. S. Holehouse, S. B. Padrick, A. Mittal, R. Ali, A. A. Yunus, D. R. Liu, R. V. Pappu and M. K. Rosen, "Sequence Determinants of Intracellular Phase Separation by Complex Coacervation of a Disordered Protein" *Mol. Cell*, 2016, **63**, 72–85.

[141] K. L. Weirich, K. Dasbiswas, T. A. Witten, S. Vaikuntanathan and M. L. Gardel, "Self-organizing motors divide active liquid droplets" *Proc. Natl. Acad. Sci.*, 2019, **116**, 201814854.

[142] P. Poulin, H. Stark, T. C. Lubensky and D. A. Weitz, "Novel colloidal interactions in anisotropic fluids" *Science*, 1997, **275**, 1770–1773.

[143] X. Wang, D. S. Miller, J. J. De Pablo and N. L. Abbott, "Organized assemblies of colloids formed at the poles of micrometer-sized droplets of liquid crystal" *Soft Matter*, 2014, **10**, 8821–8828.

[144] P. X. Wang, W. Y. Hamad and M. J. MacLachlan, "Size-Selective Exclusion Effects of Liquid Crystalline Tactoids on Nanoparticles: A Separation Method" *Angew. Chemie - Int. Ed.*, 2018, **57**, 3360–3365.

[145] A. A. Hyman, C. A. Weber and F. Jülicher, "Liquid-Liquid Phase Separation in Biology"

Annu. Rev. Cell Dev. Biol., 2014, **30**, 39–58.

[146] H. Jiang, S. Wang, Y. Huang, X. He, H. Cui, X. Zhu and Y. Zheng, "Phase Transition of Spindle-Associated Protein Regulate Spindle Apparatus Assembly" *Cell*, 2015, **163**, 108–122.

[147] N. J. Cairns, V. M.-Y. Lee and J. Q. Trojanowski, "The cytoskeleton in neurodegenerative diseases" *J. Pathol.*, 2004, **204**, 438–449.

[148] X. Su, J. A. Ditlev, E. Hui, W. Xing, S. Banjade, J. Okrut, D. S. King, J. Taunton, M. K. Rosen and R. D. Vale, "Phase separation of signaling molecules promotes T cell receptor signal transduction" *Science*, 2016, **352**, 595–599.

[149] D. R. Scheff, S. A. Redford, C. Lorpaiboon, S. Majumdar, A. R. Dinner and M. L. Gardel, "Actin filament alignment causes mechanical hysteresis in cross-linked networks" *Soft Matter*, 2021, **17**, 5499–5507.

[150] P. Bieling, T.-D. Li, J. Weichsel, R. McGorty, P. Jreij, B. Huang, D. A. Fletcher and R. D. Mullins, "Force Feedback Controls Motor Activity and Mechanical Properties of Self-Assembling Branched Actin Networks" *Cell*, 2016, **164**, 115–127.

[151] F. Rückerl, M. Lenz, T. Betz, J. Manzi, J. L. Martiel, M. Safouane, R. Paterski-Boujemaa, L. Blanchoin and C. Sykes, "Adaptive Response of Actin Bundles under Mechanical Stress" *Biophys. J.*, 2017, **113**, 1072–1079.

[152] S. M. Volkmer Ward, A. Weins, M. R. Pollak and D. A. Weitz, "Dynamic viscoelasticity of actin cross-linked with wild-type and disease-causing mutant α-actinin-4" *Biophys. J.*, 2008, **95**, 4915–4923.

[153] M. L. Gardel, F. Nakamura, J. H. Hartwig, J. C. Crocker, T. P. Stossel and D. A. Weitz, "Prestressed F-actin networks cross-linked by hinged filamins replicate mechanical properties of cells" *Proc. Natl. Acad. Sci.*, 2006, **103**, 1762–1767.

[154] O. Chaudhuri, S. H. Parekh and D. A. Fletcher, "Reversible stress softening of actin networks" *Nature*, 2007, **445**, 295–298.

[155] A. Sharma, M. Sheinman, K. M. Heidemann and F. C. Mackintosh, "Elastic response of filamentous networks with compliant crosslinks" *Phys. Rev. E - Stat. Nonlinear, Soft Matter Phys.*, 2013, **88**, 1–9.

[156] B. Wagner, R. Tharmann, I. Haase, M. Fischer and A. R. Bausch, "Cytoskeletal polymer networks: the molecular structure of cross-linkers determines macroscopic properties." *Proc. Natl. Acad. Sci.*, 2006, **103**, 13974–8.

[157] S. L. Freedman, S. Banerjee, G. M. Hocky and A. R. Dinner, "A Versatile Framework for Simulating the Dynamic Mechanical Structure of Cytoskeletal Networks" *Biophys. J.*, 2017, **113**, 448–460.

[158] A. W. Lees and S. F. Edwards, "The computer study of transport processes under extreme conditions" *J. Phys. C Solid State Phys.*, 1972, **5**, 1921–1928.

[159] H. J. C. Berendsen, J. P. M. Postma, W. F. Van Gunsteren, A. Dinola and J. R. Haak, "Molecular dynamics with coupling to an external bath" *J. Chem. Phys.*, 1984, **81**, 3684–3690.

[160] N. Y. Yao, C. P. Broedersz, M. Depken, D. J. Becker, M. R. Pollak, F. C. MacKintosh and D. A. Weitz, "Stress-Enhanced Gelation: A Dynamic Nonlinearity of Elasticity" *Phys. Rev. Lett.*, 2013, **110**, 1–5.

[161] S. S. Margossian and S. Lowey, "Preparation of Myosin and Its Subfragments from Rabbit Skeletal Muscle" *Methods Enzymol.*, 1982, **85**, 55–71.

[162] A. B. Verkhovsky and G. G. Borisy, "Non-sarcomeric mode of myosin II organization in the fibroblast lamellum" *J. Cell Biol.*, 1993, **123**, 637–652.

[163] P. Thévenaz, U. E. Ruttimann and M. Unser, "A pyramid approach to subpixel registration based on intensity" *IEEE Trans. Image Process.*, 1998, **7**, 27–41.

[164] I. Linsmeier, S. Banerjee, P. W. Oakes, W. Jung, T. Kim and M. P. Murrell, "Disordered actomyosin networks are sufficient to produce cooperative and telescopic contractility" *Nat. Commun.*, 2016, **7**, 1–9.

[165] M. B. Smith, H. Li, T. Shen, X. Huang, E. Yusuf and D. Vavylonis, "Segmentation and tracking of cytoskeletal filaments using open active contours" *Cytoskeleton*, 2010, **67**, 693–705.

[166] D. Zimmermann, A. N. Morganthaler, D. R. Kovar and C. Suarez, "In vitro biochemical characterization of cytokinesis actin-binding proteins" in *Yeast Cytokinesis: Methods and Protcols*, eds. A. Sanchez-Diaz and P. Perez, Humana Press Inc., 2016, vol. 1369, pp. 151–179.

[167] I. J. Lee, V. C. Coffman and J. Q. Wu, "Contractile-ring assembly in fission yeast cytokinesis: Recent advances and new perspectives" *Cytoskeleton*, 2012, 69, 751–763.

[168] F. A. Barr and U. Gruneberg, "Cytokinesis: Placing and Making the Final Cut" *Cell*, 2007, 131, 847–860.

[169] S. Mukhina, Y. li Wang and M. Murata-Hori, "α-Actinin Is Required for Tightly Regulated Remodeling of the Actin Cortical Network during Cytokinesis" *Dev. Cell*, 2007, **13**, 554–565.

[170] J. Gladrow, N. Fakhri, F. C. Mackintosh, C. F. Schmidt and C. P. Broedersz, "Broken Detailed Balance of Filament Dynamics in Active Networks" *Phys. Rev. Lett.*, 2016, **116**, 1–6.

[171] D. S. Seara, V. Yadav, I. Linsmeier, A. P. Tabatabai, P. W. Oakes, S. M. A. Tabei, S. Banerjee and M. P. Murrell, "Entropy production rate is maximized in non-contractile actomyosin" *Nat. Commun.*, 2018, **9**, 4948.

[172] C. Battle, C. P. Broedersz, N. Fakhri, V. F. Geyer, J. Howard, C. F. Schmidt and F. C. Mackintosh, "Broken detailed balance at mesoscopic scales in active biological systems" *Science*, 2016, **352**, 604–607.

[173] G. Lee, G. Leech, P. Lwin, J. Michel, C. Currie, M. J. Rust, J. L. Ross, R. J. McGorty, M. Das and R. M. Robertson-Anderson, "Active Cytoskeletal Composites Display Emergent Tunable Contractility and Restructuring" *arXiv*, 2021, 2021.04.08.439072.

[174] S. J. Anderson, J. Garamella, S. Adalbert, R. J. McGorty and R. M. Robertson-Anderson, "Subtle changes in crosslinking drive diverse anomalous transport characteristics in actin-microtubule networks" *Soft Matter*, 2021, **17**, 4375–4385.

[175] T. H. Tan, M. Malik-Garbi, E. Abu-Shah, J. Li, A. Sharma, F. C. MacKintosh, K. Keren, C. F. Schmidt and N. Fakhri, "Self-organized stress patterns drive state transitions in actin cortices" *Sci. Adv.*, 2018, **4**, eaar2847.

[176] A. Hernández-Vega, M. Braun, L. Scharrel, M. Jahnel, S. Wegmann, B. T. Hyman, S. Alberti, S. Diez and A. A. Hyman, "Local Nucleation of Microtubule Bundles through Tubulin Concentration into a Condensed Tau Phase." *Cell Rep.*, 2017, **20**, 2304–2312.

[177] J. A. Spudich and S. Watt, "The Regulation of Rabbit Skeletal Muscle Contraction" *J. Biol. Chem.*, 1971, **246**, 4866–4871.

[178] J. D. Winkelman, C. Suarez, G. M. Hocky, A. J. Harker, A. N. Morganthaler, J. R. Christensen, G. A. Voth, J. R. Bartles and D. R. Kovar, "Fascin- and α-Actinin-Bundled Networks Contain Intrinsic Structural Features that Drive Protein Sorting" *Curr. Biol.*, 2016, **26**, 2697–2706.